Nonlinear Phenomena in Photonic Nanostructures
Modulational Instabilities And Solitons

Zhao, Xuesong

Award date:
2014

Awarding institution:
University of Bath

NONLINEAR PHENOMENA IN PHOTONIC NANOSTRUCTURES: MODULATIONAL INSTABILITIES AND SOLITONS

Xuesong Zhao

A thesis submitted for the degree of Doctor of Philosophy

University of Bath
Department of Physics

November 2013

Abstract

This thesis discusses nonlinear effects, such as modulation instability and solitons in nano-structured waveguides. The nanoscale optical waveguides have extremely small transverse dimensions, which can provide tight confinement of light. Therefore, by changing the waveguide geometry, the waveguide dispersion can be strongly altered. On the other hand, the confinement also enhances the nonlinear dispersion, allowing for nonlinear optical phenomena supported by dispersion of nonlinearity.

The new models governing evolution of the amplitudes of components of the optical waves interacting in the waveguides are derived for continuous wave and pulse wave using perturbation expansion method. The new modulation instability condition is found, as we take into account the dispersion of nonlinearity which is enhanced through a strong variation of the modal profile with the wavelength of light in sub-wavelength waveguides.

We demonstrate that this dispersion of nonlinearity can lead to the modulation instability in the regime of normal group velocity dispersion through the mechanism independent from higher order dispersions of linear waves for continuous wave. We address that the new mechanism highly associated with dispersion of nonlinearity in sub-wavelength semiconductor waveguide induces the modulation instability in picsecond regime together with the cascaded generation of higher-order sidebands. The impact of the dispersion of nonlinearity on spectral broadening of short pulses in a silicon waveguide also is considered.

We study the temporal evolutions of fundamental and one-ring solitary waves with phase dislocation in dielectric-metal-dielectric waveguides with PT-symmetry and numerically analyze the properties of these nonlinear localized modes and, In particular, reveal different scenarios of their instability.

Acknowledgements

I would like to thank my supervisor Dmitry Skryabin for his patient answering my questions and considerable support during these three years. And also thanks must go to Andrey Gorbach for teaching me a lot and helping me with my research.

Contents

Chapter 1

introduction

As an indispensable branch of modern physics, nonlinear optics has been investigated theoretically and experimentally for many years. In particular, the fruitful theoretical studies[1, 2, 3, 4, 5] shed light on that many nonlinear phenomena in optical fiber or waveguide can be captured by a simple cubic nonlinear Schrödinger (NLS) equation and its generalizations, which we will discuss in chapter 2. Based on these firmly established theory, this thesis is intended to provide a basic model governing evolution of intense light with propagation distance and time in sub-wavelength waveguides with high nonlinearity, while it is applied to describing several nonlinear effects, such as modulation instability (MI) and solitons.

In the presence of optical nonlinearity, the interaction between light and nonlinear medium brings about a rich varities of nonlinear phenomena. Generally, nonlinear effects exist due to anharmonic motion of bound electrons under the influence of an intensity field, which means, typically, only electromagnetic field is intense enough to modify the optical properties of a material system[1]. In nonlinear optics, there are many nonlinear processes classified as second or third-order parametric processes, depending on whether the second-order susceptibility or third-order susceptibility is responsible for them. These effects attract lots of interests of researchers, for instance, self-phase modulation (SPM), which results from dipole excitations induced by three photons (Figure 1.1.1 (a) shows this process) and leads to spectral broadening of pulses while mantaining the profile of the pulses, cross-phase modulation (XPM), in which two signals interact with each other without any energy transfer between

them, third-harmonic generation (THG), which allows a new signal oscillating at $\omega_{THG} = 3\omega$ (ω is pump frequency) , four wave mixing (FWM), in which three photons interact inside the optical waveguide to generate the fourth photon, second-harmonic generation through second-order susceptibility, in which photons interacting with a nonlinear material are combined to form new photons with twice the energy, and twice the frequency of the initial photons.

Nonlinearity is a universal phenomenon in nature. In particular, nonlinear optics offers a fertile and accessible ground in which concepts from another branch of physics can be realized and investigated experimentally, which explains partly why nonlinear optics has become an active subject recently.

In this work, the main nonlinear effects, which are investigated in details in the following chapters, are FWM (or modulation instability) and soliton.

1.1 General principles of four wave mixing

One of the most important nonlinear effects in optical waveguides is the FWM arising from the interaction of four photons through the third-order nonlinear susceptibility. One can distinguish several of such processes, see Figure 1.1.1(c,d). Specifically, in this work, we are concerned with so-called degenerate FWM, in which two identical pump photons generate signal and idler ones. Only when the phase mismatch between the interacting waves nearly vanishes, does significant FWM occur. Physically, from the classical point of view, the way of understanding these conditions is that since the energy transfer is a coherent process, all optical fields inside the waveguides must maintain a special relationship between the correlation phases to provide constructive interference. Thus basically, FWM requires matching of the frequencies as well as of the wave vectors. From quantum mechanical point of view, the energy conservation in the FWM can be expressed as:

$$\hbar\omega_{p1} + \hbar\omega_{p2} = \hbar\omega_s + \hbar\omega_i, \tag{1.1.1}$$

where ω_{p1}, ω_{p2} are the frequencies of the pumps, ω_s and ω_i are frequencies of signal and idler waves, respectively, and $\hbar$ is reduced Planck Constant. During this process, two photons at frequencies ω_{p1}, ω_{p2} are annihilated with simul-

taneous creation of two photons at frequencies ω_s, ω_i. Figure 1.1 shows these processes for several cases. Fortunately, the energy conservation is automatically satisfied, which indicates that matching of the frequencies can always be obtained. At the same time, the phase matching can be expressed as the momentum conservation:

$$\hbar\kappa_{p1} + \hbar\kappa_{p2} = \hbar\kappa_s + \hbar\kappa_i, \tag{1.1.2}$$

where $\kappa_{p1}, \kappa_{p2}, \kappa_s, \kappa_i$ are propagation constants corresponding to two pumps, signal and idler waves. By using the expression:

$$\kappa = \frac{n_{eff}(\omega)\omega}{c},$$

where n_{eff} is the effective index of refraction (see below for details) in optical waveguides. Substituting it into 1.1.2, we obtain:

$$n_{eff}(\omega_{p1})\omega_{p1} + n_{eff}(\omega_{p2})\omega_{p2} - n_{eff}(\omega_s)\omega_s + n_{eff}(\omega_i)\omega_i = 0. \tag{1.1.3}$$

From 1.1.3, it is obvious that the momentum in FWM is not always conserved unless a specific choice of frequencies and the refractive indices has been chosen carefully.

In order to explain how FWM occurs in a concise way, we define that total propagation constant consists of two parts: one is from material dispersion and geometrical dispersion, another one is from nonlinear effects in optical waveguides. Material dispersion refers to the dependence of materials refractive index on the frequency of the light. Geometrical dispersion strongly depends on the shape of waveguide, especially for semiconductor waveguide with high-index contrast. As for nonlinear part, the self-phase modulation (SPM) and cross-phase modulation (XPM) contributions have to be included. Figure 1.1(a,b) shows two processes. For these two parts, we will investigate how they affect the achievement of FWM in chapter 2. Here, for instance, for degenerate FWM, if we choose the reference frequency to be the pump frequency, the net phase mismatch is given by:

$$\delta\kappa = 2\kappa_p - \kappa_s - \kappa_i, \tag{1.1.4}$$

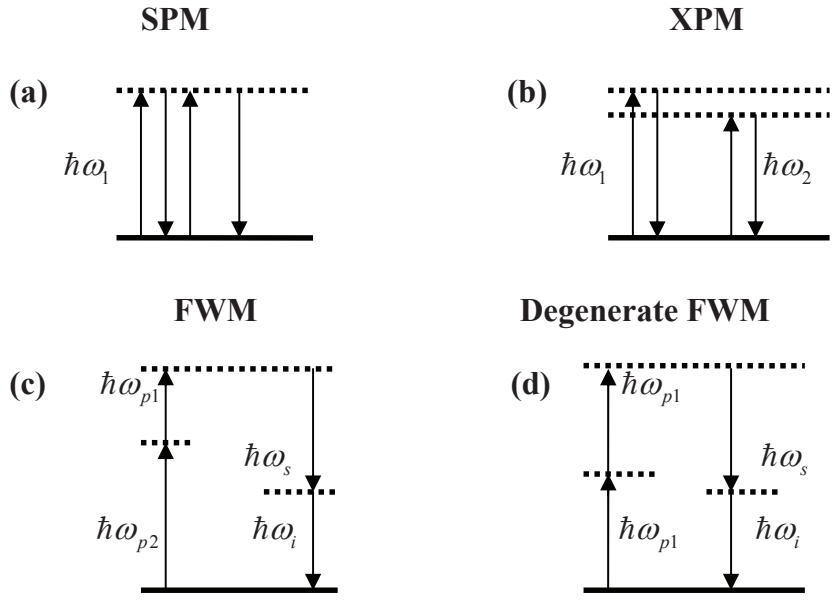

Figure 1.1.1: Schematic diagrams of possible energy level. Self-phase modulation (SPM), cross-phase modulation (XPM), degenerate and non-degenerate four-wave mixing (FWM).

here,

$$\kappa_p = \gamma p, \tag{1.1.5}$$

$$\kappa_s = \beta(\omega_s) - \beta(\omega_p) + 2\gamma p, \tag{1.1.6}$$

$$\kappa_i = \beta(\omega_i) - \beta(\omega_p) + 2\gamma p, \tag{1.1.7}$$

where $\kappa_p, \kappa_s, \kappa_i$ are total propagation constants corresponding to the pump, signal and idler waves, γ is nonlinear parameter measured in $1/W \cdot m$, and p is the initial power. Substituting 1.1.5 1.1.6 1.1.7 into 1.1.4, we obtain:

$$\delta\kappa = \delta\beta - 2\gamma p, \tag{1.1.8}$$

where $\delta\beta$ is linear phase mismatch which is from the linear dispersion, and the second term of 1.1.8 is from SPM and XPM. From 1.1.8, in order to achieve phase matching, the linear phase mismatch $\delta\beta$ must be positive. The above qualitative consideration is often found in text books[1]. However, it ignores the impact of dispersion of nonlinearity on FWM, which is one of the main topics of this thesis.

It is worth mentioning that modulation instability (MI), which is discussed in this thesis, actually is the description of FWM. By perturbing a steady state of continuous wave (CW) light inside an optical fibre, it was found that, in the time domain, such a small perturbation can cause the CW light break up into a short pulse train. The physics behind this is that the perturbation with a frequency Ω grows exponetially with the propagation distance if the pump frequency ω_0 is in the anomalous dispersion regime[1]. On the other hand, in the frequency domain, two sidebands at $\omega_0 \pm \Omega$, which are symmetrically located in both sides, are generated. This is exactly what the FWM describes.

1.2 Solitons

Solitons have been found in many branches of physics, such as Bose–Einstein condensate[6], fluid dynamics[7, 8] and plasma physics[8, 9]. In nonlinear optics, soliton is a very important nonlinear effect, which results from the balance

between linear dispersion or diffraction and nonlinearity.

A soliton is a wavepacket localised either spatially or temporally. In 1844, James Scott Russell observed that a heap of water in a canal can continuously propagate over several Kilometers without any distortion[10]. Such wave later was termed solitary wave. In the optics literature, it is common to refer to solitary waves as solitons. An appropriate mathmatical model was introduced and the inverse scattering method was used to find soliton solution for Korteweg-deVries (KdV) equation in the 1960s[11]. Since then, inverse scattering method has been employed to solve many kinds of nonlinear equations, including NLS[1]. It should be mentioned that most of properties of optical solitons can be understood within the frame of NLS[1].

1.2.1 Optical temporal solitons

In optics, the pulses propagating inside the fiber can mantain their shape intact because the nonlinear effect (nonlinear change of refractive index depending on the light intensity-known as optical Kerr effect) is able to compensate the dispersion exactly, see Figure 1.2.1. Temporal optical solitons were first predicted by Akira Hasegawa in 1973 [12], and first observed experimentally by Linn Mollenauer and Roger Stolen in 1980 in conventional fibre [13]. Since then, solitons have become an active subject and have been studied extensively. The applications have been found in fiber-optic communications[14, 15, 16]. Transmitting solitons over thousands of km has been realized[17].

More recently, with the dramatic development of photonic crystal fibre (PCF)[18, 19], solitons[20] have been found in PCF with an intricate transverse structure of glass and air-gaps which run through their entire length. One of the advantages of PCF is that dispersion tailoring can be achieved by changing the geometry of this structure, and thus the group velocity dispersion (GVD) can be greatly altered, allowing for changing normal bulk GVD into anomalous GVD in PCF.

Also, solitons have been discovered in Silicon on insulator (SOI) waveguides with strong ultrafast nonlinearity[21, 22, 23, 24, 25], and the capability for dispersion engineering[26, 27, 28].

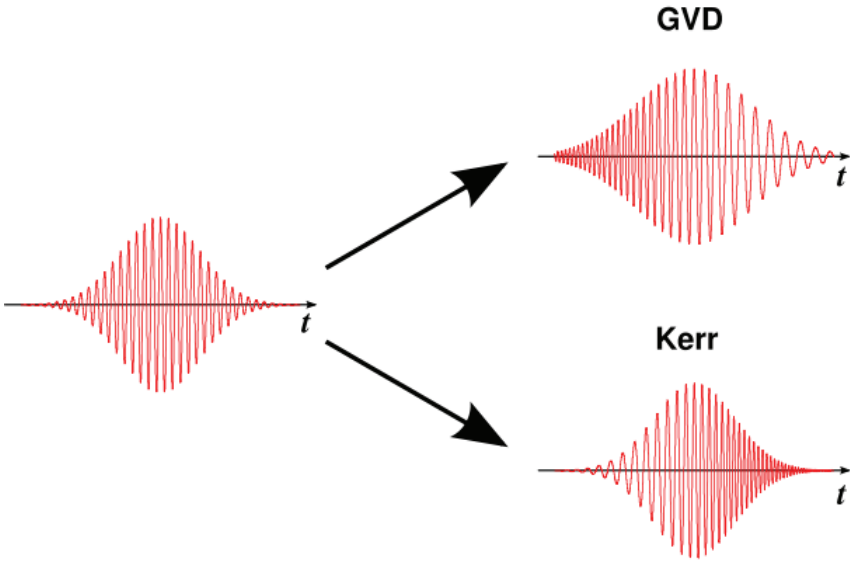

Figure 1.2.1: For Gaussian pulse in time domain, in the left, the front and trailing of the pulse contain equal amount of the frequencies, which are negatively and positively detuned from center frequency ω_0. On the top right, the initially existing frequencies are redistributed across the pulse in time domain due to GVD (no new frequencies are generated during this process). In anomalous GVD range, high frequencies are fast. On the bottom right, self-phase modulation (SPM) in Kerr medium leads to spectral broadening of pulse (new frequencies are generated), while maintaining the pulse profile unaffected. Exact balance between GVD and SPM leads to soliton.

1.2.2 Optical spatial solitons

Spatial solitons can be formed if the confiment of light occurs in space during the light propagation through balancing between nonlinear effect and diffraction, as Figure 1.2.2 shown. As discussed above, the electromagnetic field can change the refractive index of the medium while propagating, thus creating an optical lens with higher refractive index in the beam's center. This induced lens is able to focus the beam (a phenomenon called self-focusing, see Figure 1.2.2), which could cancel out the natural dffraction, and therefore leads to a spatial soliton.

The earliest example of a spatial soliton dates back to 1964. Self-focussing of CW beams has been discovered in a bulk nonlinear medium[30], although it is not stable. Until 1980s, one dimensional spatial soliton has been observed using nonlinear media[31]. In 2001, it was found in a semiconductor waveguide[32]. Also, discrete spatial solitons were first introduced by Christodoulides in 1988 theoretically and were observed experimentally in 1998 using arrays of single-mode nonlinear AlGaAs waveguides[33, 34, 35]. Another kind of spatial soliton called dark soliton has been found and studied extensively in self-defocusing medium[36, 23].

As one of family of spatial solions, votex soliton causes much attention because of its unique properties. Votex soliton is also called topological soliton associated with the self-trapping of a phase singularity embedded in a optical beam. The vortex with a hole in the center is characterized by a number called the topological charge m, according to how many twists the light does, and carries orbital angular momentum, which can be applied to trapping particles[38, 39, 40, 41, 42]. Specifically, in self-focusing material, self-trapped optical beams with a ring shape was discoverd in 1985[43]. They have a spiral phase structure with a singularity in the center and these ring-like vortex beams are also called vortex solitons. Such solitons carrying a topological charge are considered in chapter 5.

1.3 Introduction of nanostructure waveguides

Because of appropriate optical properties of silicon and the mature complementary metal-oxide-semiconductor (CMOS) fabrication processing technol-

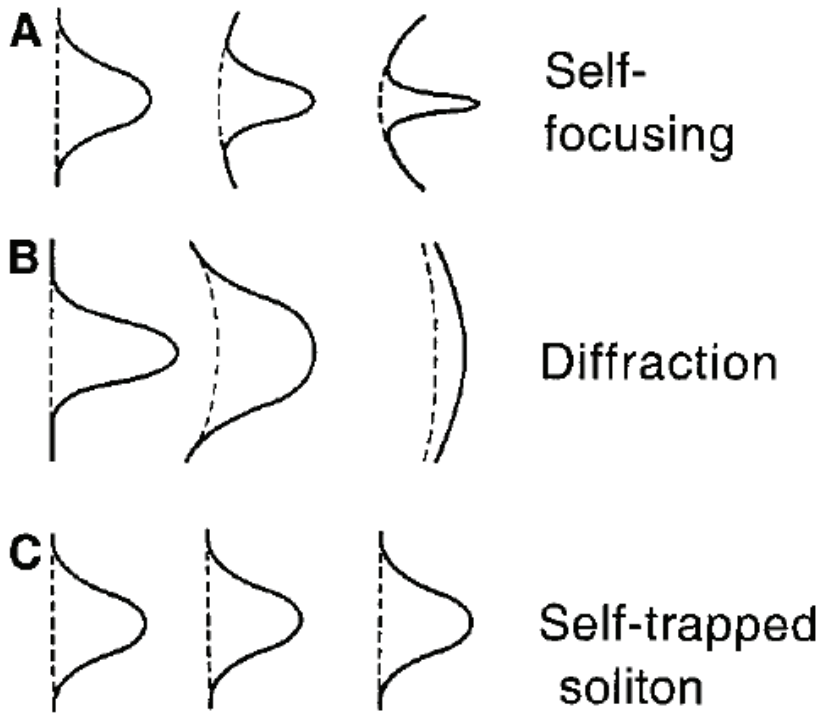

Figure 1.2.2: Schematic illustration of the spatial beam profiles (solid line) and phase fronts (dashed line) for (A) beam self-focusing, (B) normal beam diffraction, and (C) soliton propagation. A soliton forms when self-focusing exactly balances beam divergence [29].

ogy compatible with silicon, silicon photonics attracts considerable attention. [44, 46, 45]. Because of the potential application of silicon waveguides in all-optical switches, optical amplifiers, and so on, silicon waveguides become a very favorble platform to implement many kinds of functionalities by using its high Kerr nonlinearity and capability of dispersion tailoring.

For AlGaAs, nonlinear coefficient γ is 500 times larger than that of silica, and 3 times larger than that of silicon at telecommunication wavelengths[47]. Its negligible two-photon absorption (TPA) for wavelength $\lambda > 1.55\mu m$ makes it more attractive[48] despite its relatively high material cost. The tight confinement of the optical waves in such AlGaAs nanowires can cause a strong variation of dispersion by altering the geometry of waveguides[50].

1.3.1 Semiconductor waveguide

In this section, we introduce several geometries of silicon waveguides. The typical SOI devices and the guided modes considered in this thesis are given in Figure 1.3.1, 1.3.2.

SOI devices consist of nanoscale silicon waveguides deposited on top of an insulator silica base (Figure 1.3.1). It gradually becomes an attractive platform for integrated photonics due to CMOS-process compatibility as mentioned before. Also, the linear and nonlinear optical properties of silicon waveguide make it an ideal medium for nanoscale integrated photonic devices. First, large refractive index ($n = 3.5$), in conjunction with a low-index cladding ($n_{cladding} = 1.45$ for silica), leads to very tight light confinement, which makes it possible to scale silicon photonic devices down to ultrasmall cross sections. This reduction of cross section leads to the capability for dispersion engineering and a high optical field density. Silicon also has an extremely large intrinsic third-order nonlinear optical susceptibility. Together these factors result in a low optical power requirement, and short distance required to achieve nonlinear functionality.

Considerable efforts have been dedicated to SOI devices in recent years. For instance, self-phase modulation[52, 53, 54, 22], cross-phase modulation[55, 56], stimulated Raman scattering[57, 65, 59]and FWM[60, 61, 62, 63, 64, 65, 66, 67, 68, 69, 70, 71] have been explored. In this work, we will mainly investigate FWM in silicon nanowire waveguides.

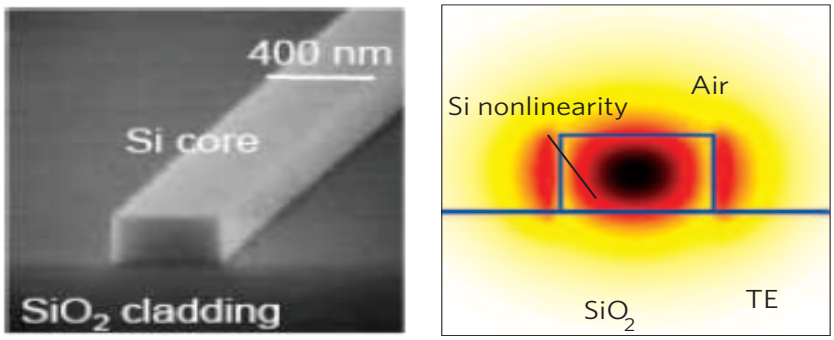

Figure 1.3.1: Cross-sectional structure of a si wire waveguide (Scanning electron micrograph (SEM) of a cross-sectional view of a typical silicon wire waveguide) and the TE guided mode corresponding to this structure (simulation using comsol).[51]

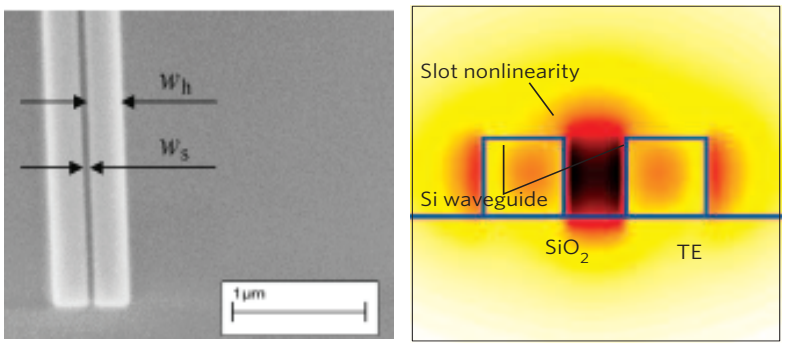

Figure 1.3.2: SEM of a silicon slot waveguide in which high nonlinear material is filled. The guided slot mode is shown on the right for the slot waveguides.[51]

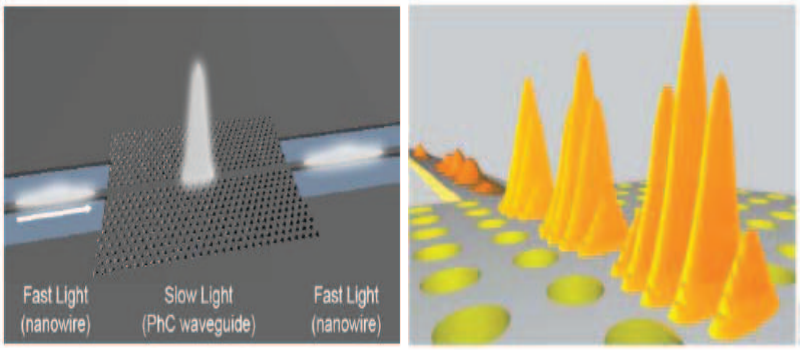

Figure 1.3.3: SEM if two dimensional photonic crystal waveguide on the left and illustration of the slow light intensity enhancement.[51]

Due to large loss induced by two photon absorption (TPA) and free carriers in silicon waveguide, realizing the optical amplifier functionalities based on silicon waveguide experimentally isn't an easy task. In order to reduce the loss and continue to enhance field intensity inside the waveguide, people began to investigate different waveguide geometry. Figure 1.3.2 shows plot of a slot waveguide. Theoretical analysis and experimental demonstration of the first slot waveguide implemented in the Si/SiO_2 material system at wavelength $\lambda = 1.55\mu m$ were reported by Cornell researchers in 2004[72, 73]. The principle of operation of a slot-waveguide is based on the discontinuity of the normal component of the electric field at high-refractive-index-contrast interfaces. Maxwell's equations manifest that, to satisfy the continuity of the normal component of the electric displacement D at an interface, the corresponding electric field must undergo a discontinuity with higher amplitude in the low-refractive-index side. In practice, the slot is uniformly filled with nonlinear material, which has large band gap and can reduce TPA. In our work, we will study FWM in slot waveguide in chapter 3.

Recently, photonic crystal (PhC) waveguides have been used for enhancing third harmonic generation and FWM[74, 75, 76]. In this kind of structure, group velocity of pulse has been reduced, which means the slowdown of the field can promote stronger light-matter interaction because the pulse is compressed

and its energy density is increased per unit length. Figure 1.3.3 shows an example of a slow light PhC waveguide on a suspended membrane fabricated from a SOI wafer[77]. On the both sides, it is connected to two tapered ridge nanowires. Here, the PhC waveguide is actually two-dimensional photonic crystal with a line defect, in which light can propagate with a frequency within the band gap of crystal.

1.3.2 Dielectric-metal waveguide

Here, we briefly introduce the dielectric-metal-dielectric waveguide, see Figure 1.3.4. On the nanoscale, there is a unique way to manipulate light through the combination of light and electrons using metallic waveguide[78, 79]. The incident light couples with the surface plasmons, which are coherent electron oscillation, to create self-sustaining, propagating along the interface electromagnetic waves known as surface plasmon polaritons (SPPs). They are localized in the direction perpendicular to the interface. Normally, light can only be focused down to microscale regions due to the diffraction limit. These unique interface waves (surface plasmon) have a much smaller wavelength at the same frequency compared to free-space wavelength (incident light wavelength). Therefore, application of SPPs enables subwavelength optics in microscopy and lithography beyond the diffraction limit[78, 79]. On the other hand, coupling light efficiently into nanometer scale volumes leads to field enhancements, which can be used to boost nonlinear phenomena[80, 81, 82]. A combination of graphene or silicon with noble-metal nanostructures indicates a varity of promising applications by making use of the properties of SPPs[83, 84]. In chapter 5, we will study the light evolution with time instead of propagation distance in dielectric-metal-dielectric waveguides with the same amount of gain in the upper layer and loss in the lower layer (see Figure 1.3.4).

1.4 Scope of the thesis

This thesis aims to study MI, the cascaded generation of higher-order sidebands and the spectral broadening of short pulses supported by new mechanism arising from dispersion of nonlinearity in nano-structured semi-conductor

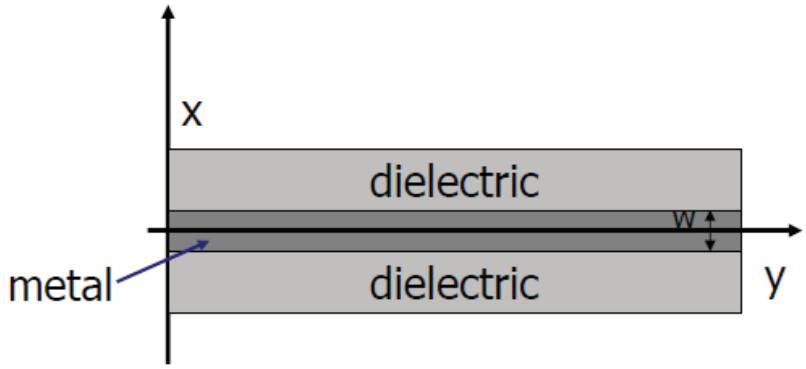

Figure 1.3.4: Geometry of a three-layer system consisting of a thin metal layer ($100nm$) sandwiched between two infinite half dielectric layers.

waveguides based on new models fully taking nonlinear dispersion into account which are derived in chapter 2 for continuous wave (CW) and pulse wave, and the dynamics of fundamental solitons and beams with a topological charge in dielectric-metal-dielectric waveguides with PT symmetry.

Tight confinement of light in sub-wavelength waveguide enhances the Kerr nonlinearity and, especially, leads to strong waveguide dispersion. At the same time, a strong variation of the modal profile with the wavelength of light causes the strong geommetric dispersion of nonlinearity. In chapter 2, by considering the nonlinear dispersion, the new models governing evolution of the amplitudes of components of the optical waves interacting in the waveguides are derived for CW and pulse wave using perturbation expansion method.

In chapter 3, by using our model derived in chapter 2, the new modulation instability condition is found, as we take into account the dispersion of nonlinearity which is enhanced through a strong variation of the modal profile with the wavelength of light in sub-wavelength waveguides. We demonstrate that this dispersion of nonlinearity can lead to the MI in the range of normal group velocity dispersion through the mechanism independent from higher order dispersions of linear waves for CW. A simple generalization of the NLS equation accounting for the MI resulting from the dispersion of nonlinearity is presented.

Furthermore, under the assumption of factorization of the four-frequency dependence of nonlinear coefficient, the model derived in chapter 2 can be

reduced to the generalized nonlinear Schrödinger-type equation. Based on this model, in chapter 4, we address that the dispersion of nonlinearity in sub-wavelength semiconductor waveguide induces the MI in picsecond regime together with the cascaded generation of higher-order sidebands. The impact of the dispersion of nonlinearity on spectral broadening of short pulses in a silicon waveguide also is considered.

In chapter 5, we study the temporal evolutions of fundamental and one-ring solitary waves with phase dislocation in dielectric-metal-dielectric waveguides with PT-symmetry and numerically analyze the properties of these nonlinear localized modes and, In particular, reveal different scenarios of their instability.

In chapter 6, the research work described in this thesis is summarized and directions for future work are discussed.

Chapter 2

Theoretical model

The propagation of light can be described directly by Maxwell's equations in the presence of linear and nonlinear polarization in optical waveguide and the equations can be integrated[85]. However, very large computational resources are needed for this.

On the other hand, to avoid the heavy numerical calculations[85], it is possible to substantially reduce the complexity of Maxwell's equations by using the envelopes of the electromagnetic fields, which are still capable of describing the dynamics of pulse accurately. Consequently, the Nonlinear Schrödinger equation (NLS), which is obtained by making several assumptions[1], has been applied to many branchs of nonlinear optics[5]. A specific extended version of the NLS equation (or the generalized NLSE), including the Raman effect term , self-steepening term and the higher order dispersion terms[1] has been introduced to characterize pulse evolution inside the fiber.

It should be emphasized that the slowly-varying envelope approximation (SVEA) is valid only if the envelope profile contains many oscillations. SVEA also allows for reducing the second-order equation into a first-order equation, which makes numerical simulations drastically reduced as the fast oscillation of the carrier wave has been removed.

Another assumption is that the z-component of the electric field is very small with respect to its transverse components. This assumption is justified for conventional fibers with a low index contrast between the core and the cladding. However, for the sub-wavelength waveguides with high index contrast, longitudinal component of the electric field is non-negligible. Thus, a

complete vector theory need to be considered[90, 86, 87].

In this chapter, based on the well-known NLS equation, a standard theory of modulation instability in optical waveguide is reviewed. For sub-wavelength waveguides, based on SVEA, the generalized NLS equations are derived by taking into account vector nature of the pulses interacting inside the waveguide.

2.1 Engineering dispersion

This thesis aims to present the third-order nonlinear optical properties of sub-wavelength silicon waveguides. As we know, most of third-order nonlinear effects stem from third-order susceptibility induced by strong external fields. In this subsection, we first discuss the origin of these nonlinear effects, together with the origin of material dispersion resulting from linear susceptibility in optical waveguides.

2.1.1 Third-order susceptibility

The optical response can often be described by expressing the polarization P as a power series when electric field E is far from medium resonance[3]. Therefore, as we know, to describe linear and nonlinear optical phenomena, the most common procedure is based on expanding the polarization P in terms of the applied electric field strength$E$:

$$P = \varepsilon_0(\chi^{(1)} \cdot E + \chi^{(2)} : EE + \chi^{(3)} \vdots EEE + \cdots), \tag{2.1.1}$$

where ε_0 is the vacuum permittivity and $\chi^{(i)}$ are the ith-order optical susceptibilities and these terms are tensors of rank $(i+1)$. In practice, the polarization can be categorized into linear and nonlinear parts: $P = P_L + P_{NL}$. The linear polarization will be discussed in next section.

Because of symmetry of si-crystal lattice, the lowest-order nonlinear effects arise from the third-order susceptibility. In this work, the second-order susceptibility is neglected for silicon and AlGaAs. Therefore, the nonlinear part can be written as:$P_{NL}^{(3)} = \varepsilon_0 \chi^{(3)} \vdots EEE$, where $\chi^{(3)}$ is third-order susceptibility. The real part of the third-order susceptibility is directly related to the nonlinear refractive index n_2. Accordingly, the imaginary part governs the TPA

coefficient β_T. One can have the expressions[1, 88]:

$$n_2 = \frac{3}{4cn_0^2\varepsilon_0} Re(\chi^{(3)}) \tag{2.1.2}$$

$$\beta_T = \frac{-3\omega}{2c^2 n_0^2 \varepsilon_0} Im(\chi^{(3)}). \tag{2.1.3}$$

In the process of two-photon absorption, an electron makes a transition from the valence band to the conduction band by the simultaneous absorption of two photons, which produces an electron-hole pair. For instance, for silicon, an electron transits from the valence band to the conduction band when energy of photons exceeds the half band gap $E_g/2$, corresponding to a wavelength of $1.1\mu m$ [88]. In addition, the TPA process also generates a considerable number of free electrons and holes depending on the peak power and duration of a pulse. These excessive carriers not only absorb light but also affect the wave propagation by changing the refractive index[88]. Thus, TPA and free carrier limit the FWM efficiency and operating power. To fully understand free charge carrier effects, we introduce equation:

$$\frac{\partial N}{\partial t} = \frac{\xi_e \beta_T |A(z,t)|^4}{2\hbar\omega_p} - \frac{N}{\tau_0} \tag{2.1.4}$$

where N is the density of electron-hole pairs, β_T is the coefficient of two-photon absorption, ξ_e is polarization factor, and τ_0 is the carrier lifetime. τ_0 depends on the waveguide design and duration of a pulse. It can be reduced to be smaller than $1ns$ by changing the waveguide dimension to improve the carrier recombination or simply by using an external electric field to sweep out the carriers. In a word, existence of TPA and free carrier in silicon waveguide can severely degrade the performance of ultrafast all-optical devices based on the optical Kerr effect.

2.1.2 Linear susceptibility and material dispersion

In the case of linear optics, the polarization varies linearly with the electric field strength, which can be expressed simply: $P_L = \varepsilon_0 \chi^{(1)} \cdot E$, where $\chi^{(1)}$ is the linear susceptibility. Its effects are included through the refractive index

n and the attenuation coefficient α. In other words, the real part of $\chi^{(1)}$ is related to the dispersive effects, whereas the imaginary part of $\chi^{(1)}$ accounts for loss or gain. In practice, for bulk silicon, we have a very useful Sellmeier equation[89, 90], which has form:

$$n_{si}^2(\lambda) = \varepsilon + \frac{A}{\lambda^2} + \frac{B\lambda_1^2}{\lambda^2 - \lambda_g^2} \tag{2.1.5}$$

with $\varepsilon = 11.686, A = 0.9398\mu m^2, B = 0.00081046, \lambda_g = 1.1071\mu m$. For bulk silica[1], Sellmeier equation is given by:

$$n_{silica}^2(\lambda) = 1 + \sum_{j=1}^{m} \frac{B_j \omega_j^2}{\omega_j^2 - \omega^2}$$

where $\omega_j$is the frequency and $B_j$is the strength of jth resonance. When $m = 3$, the values of these parameters are found to be $B_1 = 0.6961663, B_2 = 0.4079426, B_3 = 0.8974794$, $\lambda_1 = 0.0684043\mu m, \lambda_2 = 0.1162414\mu m$, $\lambda_3 = 9.896161\mu m$. Note that the material frequency dependence of bulk silicon and silica is included in equation 2.1.5. It should be mentioned that the material dispersion in standard fibers dominates the linear dispersion properties. On the contrary, in silicon waveguides, the waveguide dispersion is dominant, which means that one is able to change the total dispersion strongly by altering the geometry in the wavelength range that we are concerned.

For bulk $Al_xGa_{1-x}As$, we have a similar equation describing the refractive index $n(\omega)$. The real part of the dielectric constant ϵ_1 can be expressed as[91]:

$$\epsilon_1(\omega) = A_0\{f(\chi) + \frac{1}{2}[E_0/(E_0 + \Delta_0)]^{3/2} f(\chi_{so})\} + B_0, \tag{2.1.6}$$

where $f(\chi) = \chi^{-2}[2 - (1+\chi)^{1/2} - (1-\chi)^{1/2}], \chi = \hbar\omega/E_0, \chi_{so} = \hbar\omega/(E_0 + \Delta_0)$. A_0 and B_0 are constants and can be obtained by fitting 2.1.6 with the experimental data. The constants A_0 and B_0 as function of composition x are found to be written as:$A_0(x) = 6.3 + 19x, B_0(x) = 9.4 - 10.2x$. $\hbar\omega$ is the photon energy. Also, the numerical values of E_0 and $E_0 + \Delta_0$ can be found through:

$$E_0 = 1.425 + 1.155x + 0.37x^2$$

$$E_0 + \Delta_0 = 1.765 + 1.115x + 0.37x^2$$

Based on these equations, one can calculate the frequency dependence of $\epsilon_1$for different value of composition x. In chapter 3, particularly, we choose $x = 0.25$ to compute material dispersion for AlGaAs waveguide.

In chapter 3, we also use chalcogenide glass As_2S_3 in slot waveguide. The refractive index $n(\lambda)$ gives[92]:

$$n(\lambda) = \sqrt{\frac{1.8983678\lambda^2}{\lambda_1} + \frac{1.9222979\lambda^2}{\lambda_2} + \frac{0.8765134\lambda^2}{\lambda_3} + + \frac{0.1188704\lambda^2}{\lambda_4} + \frac{0.9569903\lambda^2}{\lambda_5} + 1} \tag{2.1.7}$$

where $\lambda_1 = \lambda^2 - 0.0225 \times 10^{-12}, \lambda_2 = \lambda^2 - 0.0625 \times 10^{-12}, \lambda_3 = \lambda^2 - 0.1225 \times 10^{-12}$, $\lambda_4 = \lambda^2 - 0.2025 \times 10^{-12}$, $\lambda_5 = \lambda^2 - 750 \times 10^{-12}$.

2.1.3 Geometric dispersion

In this section, we review the characteristics of group-velocity dispersion (GVD) inside SOI waveguides due to its impact on the phase matching in FWM process.

As we know, in small core optical fibers, the waveguide geometry contributes to dispersion. Utilizing this feature in silica fibers, one can tailor their dispersion by changing the size of the fiber core[94, 95], or by using a photonic-crystal cladding[93]. In SOI waveguides, because of the extremely small cross sections and high index contrast which cause strong optical confinement, waveguide dispersion dominates the dispersive properties of silicon waveguides[28, 90]. It should be pointed out that, in our calculations, the material dispersion is included by using the equations 2.1.5,2.1.6,2.1.7.

One of the main goals of tailoring dispersion is that we need to reduce the broadening of pulse propagating inside the waveguide by careful designing the waveguide to minimize GVD for a given wavelength. Figure 2.1.1 shows that there are two zero-GVD wavelengths for small waveguide dimension. From this figure, one can find that dispersion can be engineered simply by changing

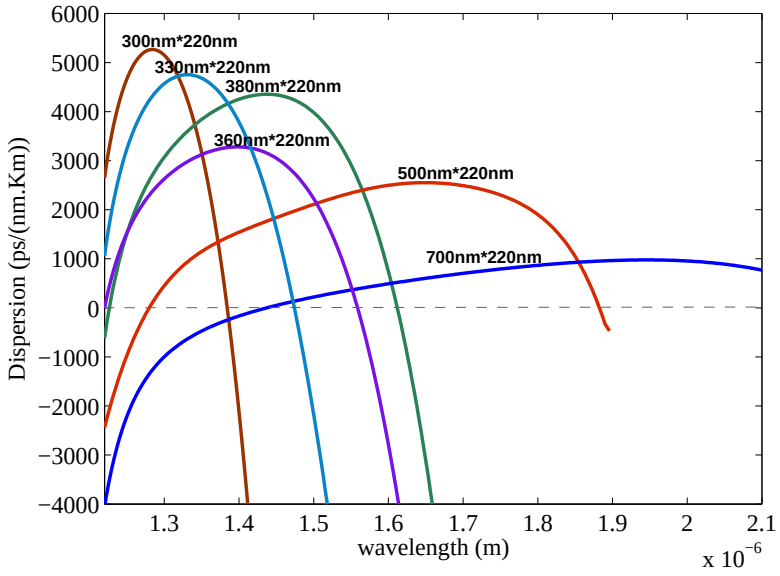

Figure 2.1.1: Dispersion curves as function of wavelength for several silicon waveguides with different cross-section. Positive values correspond to anomalous GVD and negative values correspond to normal GVD . We use commercial software comsol to compute propagation constant corresponding to guided quasi-TE modes.

the waveguide dimensions or the width of the silicon waveguide core. The zero-GVD point shifts towards the large wavelength with the increase of width of waveguides. On the other hand, the maximal value of GVD becomes smaller. It is worth mentioning that large GVD can minimize the overall bandwidth of FWM. Therefore, working near the zero-GVD wavelength is very essential for gaining broader bandwidth.

We should note that the higher-order dispersion is important in FWM processes. Especially, operating near the Z-GVD point makes higher-order dispersion critical. By varying the core-cladding index difference, higher-order dispersion can be engineered simultaneously[96].

Finally, for different modes existing in waveguides, one should use different method to acquire the ideal curve of dispersion. In principle, the boundaries decide an optical mode. On the boundaries, the electric field is discontinuous. Therefore, the qusi-TE mode is more sensitive to the two sidewalls and the waveguide width. On the contrary, the quasi-TM mode is affected mainly by the top and bottom interfaces and the waveguide height[88].

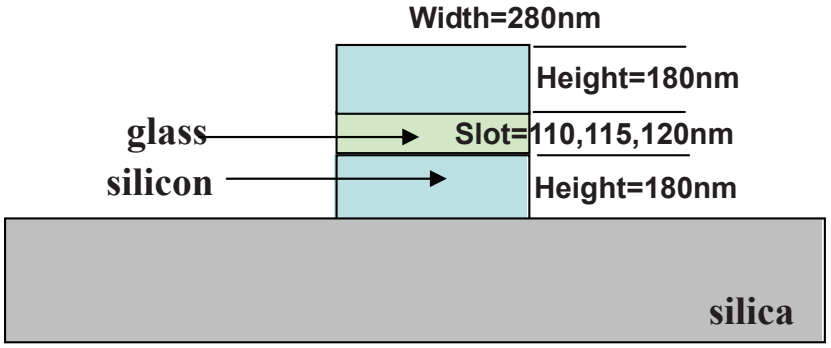

Figure 2.1.2: Slot waveguide with silicon layers surrounding a highly nonlinear chalcogenide slot layer.

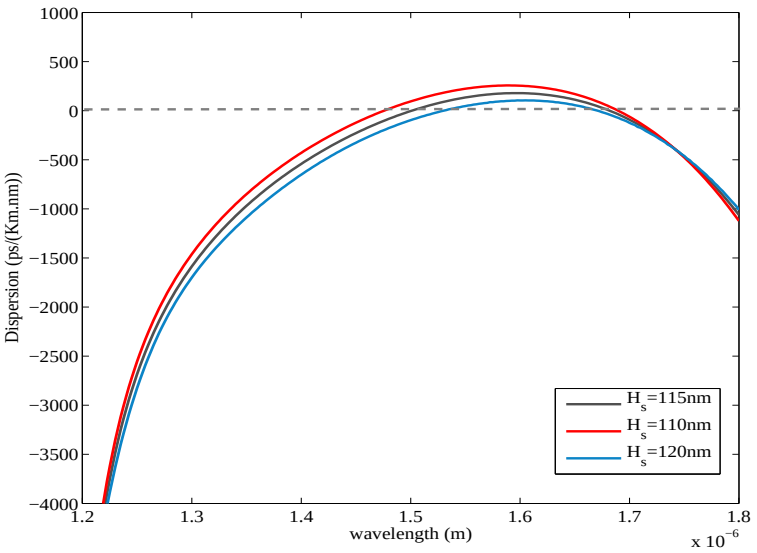

Figure 2.1.3: Dispersion curves in 10-cm-long chalcogenide slot waveguides with different slot heights. The geometry is same as Figure 2.1.2.

In the preceding section, we discussed how to engineer the dispersion for single silicon waveguide. It should be mentioned that one can tailor dispersion for slot waveguide by a careful control of the geometrical waveguide parameters including the cross sectional area, the slot fill factor, and the slot asymmetry degree[97, 98, 99]. For instance, in a vertical slot waveguide (see Figure 2.1.2), one can obtain different dispersion curves by changing the slot waveguide height for quasi-TM mode (The confined TM mode is shown in chapter 3). The Figure 2.1.3 shows these results clearly.

As we mentioned before, the efficient FWM requires minimal phase-mismatch of the four interacting waves. From equation 1.1.8 and the equations 2.2.9, 2.2.11 we will derive below, one can see that the phase matching can be satisfied by locating the pump in the anomalous dispersion regime because the nonlinear part of the phase mismatch is always positive. By changing the geometry of waveguide, one is always able to obtain the anomalous dispersion in the wavelength range that we are interested.

2.2 Basic theory of modulation instability in optical waveguides

In many nonlinear systems[7, 100, 101, 102, 103], especially, in optical nonlinear systems, the combination of dispersive and nonlinear effects can lead to modulation of the steady state when a pulse or CW beam propagates inside optical waveguides, which is referred to as the modulation instability or FWM. E.g., when only one strong pump wave is incident on a waveguide, and the phase-matching condition is satisfied, the spectral sidebands can be generated from noise and the input wave is broken into a train of ultrashort pulses. If sidebands are seeded by a weak input signal, the signal is amplified and, the idler wave is generated simultaneously. In latter case, usually, we call this nonlinear process as degenerate FWM. In this section, the previously known theory about FWM will be reviewed in details.

Generally, when an electromagnetic wave interacts with bound electrons of a dielectric, the medium response depends on the optical frequency. This property is referred to as material dispersion. On the other hand, for the sub-wavelength waveguide, due to the effects at the material boundaries, a

waveguide introduces dispersion of its own. Waveguide dispersion plays an important role in propagation of short optical pulses because different spectral components within the pulse travel at different speed. Therefore, to realize matching of wave vector in FWM, controlling characteristic of dispersion of optical waveguide becomes important (see above for more details). We first introduce the propagation constant β, which is associated with frequency and accounts for effect of dispersion. However, it is not easy to obtain the exact functional form of β. By expanding β in a series around the carrier frequency , we found:

$$\beta(\omega) = n_{eff}\frac{\omega}{c} = \beta_0 + (\omega-\omega_0)\beta_1 + \frac{1}{2}(\omega-\omega_0)^2\beta_2 + \frac{1}{6}(\omega-\omega_0)^3\beta_3 + \cdots, \quad (2.2.1)$$

and β_n are the dispersion coefficients. n_{eff} is effective index, which includes effects of the material dispersion and geometrical dispersion. $\beta_1 = {}^1\!/_{v_g}$ is group velocity, and β_2 represents dispersion of the group velocity (GVD). Note that we can alter the zero GVD point by changing the width and height of waveguide (see below for more details). Dispersion parameter D is related to β_2 by the relation:

$$D = \frac{d\beta_1}{d\lambda} = -\frac{2\pi c}{\lambda^2}\beta_2.$$

When $D < 0$, the optical waveguide is said to exhibit normal dispersion. By contrast, the positive value of D gives anomalous GVD. The coefficient and above constitute of what is known as high order dispersion (HOD).

We start with the Nonlinear Schrodinger equation, which can be derived from Maxwell equations[1]. If losses are ignored, and width of optical pulses is large than $1ps$, NLS equation takes the form:

$$i\partial_z E = -(\frac{i}{1!}\beta_1\partial_t + \frac{i^2}{2!}\beta_2\partial_t^2 + \frac{i^3}{3!}\beta_3\partial_t^2 + \cdots)E - \gamma|E|^2E, \quad (2.2.2)$$

where E represents the complex amplitude of the field envelope. The two terms in the right hand side are the dispersive and nonlinear shifts of β_0, respectively. γ is nonlinear parameter. The pump frequency has been taken as the reference frequency ω_0. To study FWM, we look for the overall field in the form:

$$E = A_p(z)e^{i\kappa_p z} + A_s(z)e^{i\kappa_s z - i\Omega t} + A_i(z)e^{i\kappa_i z + i\Omega t}, \quad (2.2.3)$$

where $\omega_{s,i} = \omega_0 \pm \Omega$, and $A_p(z), A_s(z)A_i(z)$ are the amplitudes corresponding to the pump, signal and idler waves, $\kappa_p, \kappa_s, \kappa_i$ represent the propagation constants including linear and nonlinear contributions, and Ω is the frequency detuning. Here, we define the total phase mismatch as:

$$\delta\kappa = 2\kappa_p - \kappa_s - \kappa_i. \tag{2.2.4}$$

Substituting the expression 2.2.3 into equation 2.2.2, we arrive at:

$$i\partial_z A_p - \kappa_p A_p = -\gamma|A_p|A_p, \tag{2.2.5}$$

$$i\partial_z A_s - \kappa_s A_s = (\beta_p - \beta_s(\omega_p + \Omega))A_s - 2\gamma|A_p|^2 A_s - \gamma A_p^2 A_i^* e^{i\delta\kappa z}, \tag{2.2.6}$$

$$i\partial_z A_i - \kappa_i A_i = (\beta_p - \beta_i(\omega_p + \Omega))A_i - 2\gamma|A_p|^2 A_i - \gamma A_p^2 A_s^* e^{i\delta\kappa z}, \tag{2.2.7}$$

where $\beta_p, \beta_s, \beta_i$ are the linear propagation constants. In the equation 2.2.5-2.2.7, we have assumed that signal and idler wave are weak, so the nonlinear terms in the signal and idler can be neglected. In equation 2.2.5, the term in the right side represents the SPM. From Figure 1.1.1(a), one can see that three identical photons cause dipole transitions to excited states. When these excited states do not correspond to a real level, an electron goes back to the original level and the photon is released instantaneously. It is this instantaneous response that has attracted the interest of the researchers over the years. SPM results in an intensity-dependent refractive index change n_2, which is the nonlinear index coefficient inducing the spectral changes of pulse. In equation 2.2.6, the second term in the right hand side represents XPM, in which one field at frequency ω_1 influences another field at frequency ω_2 . Note that, In this nonlinear process, there is no energy transfer between two optical fields. As we can see from the equation 2.2.5-2.2.7, the refractive index change caused by XPM is twice as strong as the refractive index change caused by SPM. If we select $\kappa_{p,s,i}$ as:

$$\kappa_p = \gamma|A_p|^2,$$

$$\kappa_s = \beta_s(\omega_p + \Omega) - \beta_p + 2\gamma|A_p|^2,$$

$$\kappa_i = \beta_i(\omega_p - \Omega) - \beta_p + 2\gamma|A_p|^2.$$

and assume that the pump amplitude is constant. Then we get the following equations governing the evolution of the signal and idler waves inside a waveguide:

$$i\partial_z A_s = -\gamma A_p^2 A_i^* e^{i\delta\kappa z},$$

$$i\partial_z A_i = -\gamma A_p^2 A_s^* e^{i\delta\kappa z}. \tag{2.2.8}$$

The equation for A_s is:

$$i\partial_z^2 A_s = i\gamma|A_p|^2 A_s - \delta\kappa\partial_z A_s.$$

Assuming $A_s = e^{\lambda z}$, we find:$\lambda = \frac{i}{2}\delta\kappa \pm \sqrt{\gamma^2 p^2 - \frac{1}{4}(\delta\kappa)^2}$. From this, we define that the growth rate of modulation instability is:

$$g = Re\sqrt{\gamma^2 p^2 - \frac{1}{4}(\delta\kappa)^2},$$

where $p = |A_p|^2$ is the pump power. Also, we take $\delta\beta = 2\beta_p - \beta_s - \beta_i$, which represents the linear phase mismatch. Total phase mismatch can be written as:

$$\delta\kappa = \delta\beta - 2\gamma p. \tag{2.2.9}$$

Consequently, the gain can also be expressed by:

$$g = Re\sqrt{\frac{1}{4}\delta\beta(4\gamma p - \delta\beta)}. \tag{2.2.10}$$

From equation 2.2.10, one can see that the gain exists within $0 < \delta\beta < 4\gamma p$. By using expression 2.2.1, the linear phase mismatching $\delta\beta$ can be rewritten as[1]:

$$\delta\beta = -2\sum_{m=2,4,\cdots}^{\infty} \frac{\beta_m(\omega_p)}{m!}\Omega^m. \tag{2.2.11}$$

In standard theory, $\delta\beta$ must be positive and $\delta\beta < 4\gamma p$ in order to amplify the signal and realize frequency conversion. If β_2 dominates the linear phase mismatch, in this case, gain can exist only when GVD is anomalous. One can find that only the even-order dispersion terms influence the phase-matching condition. When GVD parameter β_2 is very small, higher order dispersion terms have to be taken into account. Therefore, adding the higher-order dispersion terms becomes critical when we operate the pump wavelength near the zero-GVD point. In this case, the higher-order dispersion plays very important role in the phase matching. Apart from the gain interval near the pump, which is due to the GVD, a second narrow gain region is located further from the pump and appears due to higher order dispersion[1, 104] . As an example, we choose the waveguide with cross-section $330nm \times 220nm$ and operate within the anomalous GVD range. By using the equation 2.2.2, the numerical result shows that the two peaks located quite close to the pump are because of GVD. The higher order dispersion can account for the two peaks, which are far from the pump wavelength (see Figure 2.2.1). Even when one operates the wavelength within the normal-GVD regime, the high-order dispersion can induce the modulation instability which occurs in the large frequency offset[1, 104].

It should be noted that, in common FWM theory as presented above, the small differences in nonlinear resonance of four light pulses are neglected, γ has the form of[1]:

$$\gamma = \frac{n_2 \omega_p}{c A_{eff}}, \tag{2.2.12}$$

where

$$A_{eff} = \frac{[\iint_{-\infty}^{+\infty} |F(x,y)|^2 dxdy]^2}{\iint_{-\infty}^{+\infty} |F(x,y)|^4 dxdy} \tag{2.2.13}$$

where c is velocity of light in vacuum, and $F(x,y)$ is the transverse distribution of the fiber mode, and n_2 is the nonlinear refractive index . Here it is reasonable to assume n_2 doesn't depend on frequency. A_{eff} is the effective mode area of an optical waveguide. Generally, the effective area should be a function of the pump, idler, and signal wavelengths due to dependence of modes distribution on frequency. However, from expression 2.2.13, the variation of the effective core area is negligible in conventional single-mode fibers. Therefore, we should note that γ is only decided by pump frequency although there are

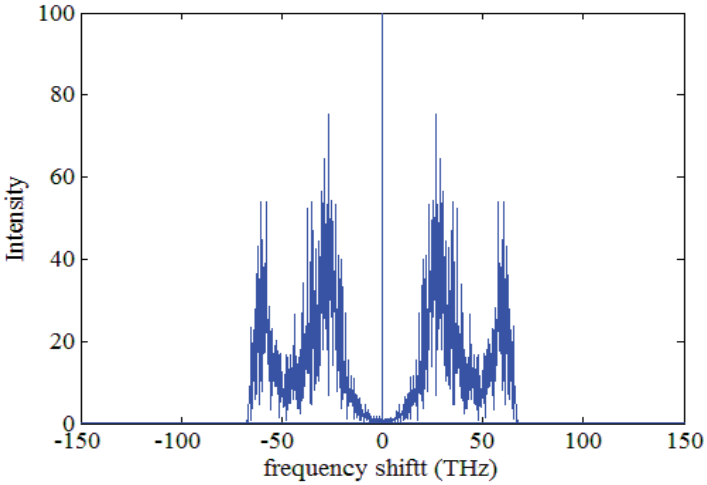

Figure 2.2.1: Spectral output of a $220nm \times 330nm$ silicon waveguide with initial power $1W$ and $\lambda_p = 1.47\mu m$. Spectral sidebands are due to modulation instability. (Note: this model doesn't include the TPA and free carrier effects.)

three interacting waves inside the waveguide. For a conventional fiber, in practice, this assumption is reasonable because the mode profile does not change much with frequency. Therefore, the effective core area A_{eff} doesn't change too much also. However, for subwavelength optical waveguide with high-index contrast, we should be careful about this assumption because the waveguide modes strongly depend on the wavelength for the given waveguide geometry. γ is not simply function of a single frequency, but it should depend on $\omega_p, \omega_s, \omega_i$, which is explored in details in the following section. More than this, in silicon waveguides, the modes inside the waveguide should include the longitudinal component of the mode fields, which has been ignored in conventional fiber, when one calculates the effective core area. Also, because the tight optical-field confinement achieved in this waveguide results in a strong dependence of the waveguide modes on waveguide geometry, for different waveguide geometry, the value of γ should be quite different. Based on these considerations, we will address a new model to calculate the value of γ and discuss the impacts of dispersion of nonlinearity on FWM in details.

2.3 Derivation of propagation equation including dispersion of nonlinearity

We noticed that many prior works[72, 75, 28]on optical waveguides have assumed that $\gamma(\omega_{pump})$ depends only on frequency of the pump field. Therefore, only the frequency dependence of the modal distribution of pump wavelength has been considered. Furthermore, the longitudinal component of the pump field hasn't been included when one calculates the nonlinear parameter γ. It is safe to make these assumptions, specifically, in the weakly guiding geometries. However, distributions of modes propagating inside the waveguides with high index contrast are strongly dependent on the frequency, which can not be simply neglected.

In order to completely understand the nonlinear optical properties of subwavelength waveguide, in particular, when conditions of phase matching are satisfied, a new model, which accounts for dispersion of nonlinearity inside the subwavelength semiconductor waveguides, is needed.

Below, a new model, which more accurately describes the dynamics of optical pulses propagating in optical waveguides is derived. First of all, we obtain the new expression of nonlinear coefficient γ, which depends on all interacting waves and all of components of the optical wave interacting in waveguide such as pump, idler and signal waves. Note that, according to our new equations, the contribution of the longitudinal component of the modes is included by considering the vectorial solutions of Maxwell's equations.

The propagation of electromagnetic fields in fibers is described by Maxwell's equations:

$$\nabla \times E = -\frac{\partial B}{\partial t} \tag{2.3.1}$$

$$\nabla \times E = J + \frac{\partial D}{\partial t} \tag{2.3.2}$$

$$\nabla \cdot D = \rho_f \tag{2.3.3}$$

$$\nabla \cdot B = 0 \tag{2.3.4}$$

where E and H are electric and magnetic field vectors, respectively, and D and B are corresponding to the electric displacement and magnetic induction, respectively, ρ_f and J are the external electric charge and current densities, respectively. These Maxwell equations are the fundamental equations of the theory of electrodynamics and determine the electromagnetic field completely. In particular, in waveguides, external charges are absent, which means $J = 0$ and $\rho_f = 0$. In the following section, based on these equations, a set of equations describing the light propagation in optical waveguides with high index contrast are derived.

We start with Maxwell's equations for electric and magnetic fields:

$$\Xi(\overrightarrow{r},t) = \frac{1}{2}\sum_n E_n(\overrightarrow{r})e^{-i\omega_n t} + c.c$$

$$\mathcal{H}(\overrightarrow{r},t) = \frac{1}{2}\sum_n H_n(\overrightarrow{r})e^{-i\omega_n t} + c.c.$$

Each harmonic field satisfies Maxwell equations:

$$\nabla \times E_n = i\omega_n \mu_0 H_n \tag{2.3.5}$$

$$\nabla \times H_n = -i\omega_n D_n \tag{2.3.6}$$

$$D_n = \varepsilon_0 E_n + P_n$$

where D_n is the electric displacement field and P_n is the electric polarization of the medium induced by electric field and has the form:

$$P_n = \varepsilon_0[\varepsilon_L(\overrightarrow{r}) - 1]E_n + \delta P_n. \tag{2.3.7}$$

The first term in the right hand side is linear polarisation and the second term δP_n consists of nonlinear polarization, free carrier, and linear loss, respectively and is given by:

$$\delta P_n = \delta P_n^{(NL)} + \delta P_n^{(FC)} + \delta P_n^{(L)}.$$

For convenience, we use Lorentz reciprocity theorem by constructing two sets

of fields:[2, 90, 105]:

$$\frac{\partial}{\partial z}\int_A F_c \hat{} _z dA = \hat{\int_A} \nabla \cdot F_c d\hat{A} \tag{2.3.8}$$

$$F_c = E_1 \times H_2^* + E_2^* \times H_1,$$

where $\hat{e_z}$ is the unit vector along the longitudinal axis of the waveguide, and the field F_c consists of two arbitrary guided fields (E_1, H_1) and (E_2, H_2). It is important that A should be large enough that the modes decay to zero at the boundaries. Now we consider that $(E_n, H_n) = (E_2, H_2)$ are the fields created by the nonlinear polarization and free carriers, and so on, and $(E_1, H_1) = (e_n e^{i\beta_n z}, h_n e^{i\beta_n z})$ is the electromagnetic field in an ideal linear waveguide. Here, e_n, h_n denote the mode at the corresponding frequency ω_n. Based on Maxwell equations, through various numerical methods including Finite Element methods, the vectorial modes consisting of three components can be obtained. We neglect the time dependence of the field by assuming quasi-CW condition. For the perturbed fields, we choose the following:

$$E_n = u_n(z) e_n e^{i\beta_n z}$$

$$H_n = u_n(z) h_n e^{i\beta_n z},$$

where $u_n(z)$ is the complex mode amplitude, β_n is the propagation constant. Using Maxwell equations and Lorentz reciprocity theorem, we obtain:

$$I_n \frac{du_n}{dz} = i\omega_n e^{-i\beta_n z} \int_A (e^n)^* \delta P_n dA \tag{2.3.9}$$

where $I_n = \int_A (e_n \times h_n^* + h_n \times e_n^*)$. Note that, to derive equation 2.3.9, we assumed that the modes of perturbed and unperturbed waveguides are same since the variation of the index of refraction is small. In addition, the following formula has been used:

$$\nabla \cdot (f \times g) = (\nabla \times f) \cdot g - f \cdot (\nabla \times g)$$

where f and g are both vectors.

Below, we only consider the nonlinear polarization, and temporarily, neglect the other of terms. In this work, especially because the Si-crystal lattice is invariant with respect to the inversion symmetry, the second-order susceptibility disappears, i.e.$\chi^{(2)} = 0$. Thus, in silicon, the lowest-order optical nonlinearity is the third-order nonlinear response. We have:

$$\{\delta\mathcal{P}^{\mathrm{NL}}\}_\omega = \varepsilon_0\{\chi^{(3)}\vdots\Xi^3\}_\omega.$$

Here $\chi^{(3)}$ is the fourth-rank tensor. Obviously,$\chi^{(3)}\vdots\Xi^3$ is a vector. Its ith component is given by:

$$\{\chi^{(3)}\vdots\Xi^3\}_i = \sum_{p,r,s=1}^{3} \chi^{(3)}_{iprs}\Xi_p\Xi_r\Xi_s.$$

In general, $\chi^{(3)}$ has 81 components. Fortunately, because silicon belongs to the crystallographic point group $m3m$, $\chi^{(3)}$ only has 21 nonzero elements[57], of which only four are independent, namely, $\chi^{(3)}_{1111}$,$\chi^{(3)}_{1122}$,$\chi^{(3)}_{1212}$,and$\chi^{(3)}_{1221}$[3]. Because of intrinsic permutation symmetry, $\chi^{(3)}_{1122} = \chi^{(3)}_{1221}$. In addition, the frequency dispersion of the nonlinear susceptibility can be neglected, so the Kleinman symmetry relations[90] imply that $\chi^{(3)}_{1122} = \chi^{(3)}_{1212}$. In this report, only the terms of frequency combinations $\omega_k - \omega_l + \omega_m = \omega_n$ are considered here. In other words, we assume that third-harmonic frequency and another sum-frequency generation processes are not phase matched. Thus, we drop all of them. By assuming the similar expression for the polarization:

$$\overrightarrow{\mathcal{P}} = \frac{1}{2}\sum_n P_n(\overrightarrow{r})e^{-i\omega_n t} + c.c.,$$

eventually, we obtain:

$$\delta P_n^{NL} = \frac{3\varepsilon_0}{4}\sum_{\omega_k-\omega_l+\omega_m=\omega_n} \chi^{(3)}\vdots E_k E_l^* E_m. \tag{2.3.10}$$

Substituting 2.3.10 into equation 2.3.9, finally, we arrive at the following differential equation:

$$I_n \frac{du_n}{dz} = \sum_{k,l,m} i\Gamma_{nklm} e^{i(\beta_k+\beta_m-\beta_l-\beta_n)z} u_k u_l^* u_m \tag{2.3.11}$$

$$\Gamma_{nklm} = \omega_n \frac{3\varepsilon_0}{4I_n} \int_A (e^n)^* \chi^{(3)} \vdots e_k e_l^* e_m dA.$$

It should be noted that the total time-averaged power is given by:

$$P = \int_A (\Xi \times \mathcal{H}) \hat{e_z} dA = \sum_n |u_n|^2 I_n/4.$$

It is convenient to introduce rescaled amplitudes $a_n = \sqrt{I_n} u_n/2$, so the total time-averaged power is given by:

$$P = \sum_n |a_n|^2.$$

By using this transformation, our new equation reads as:

$$\frac{da_n}{dz} = \sum_{k,l,m} i\gamma_{nklm} e^{i(\beta_k+\beta_m-\beta_l-\beta_n)z} a_k a_l^* a_{m,} \tag{2.3.12}$$

where

$$\gamma_{nklm} = 4\sqrt{\frac{I_n}{I_k I_l I_m}} \Gamma_{nklm}.$$

As we discussed before, for silicon, its nonlinear response has only four independent components and can be written as:

$$\chi^{(3)}_{iprs} = \chi^{(3)}_{1122}\delta_{ip}\delta_{rs} + \chi^{(3)}_{1212}\delta_{ir}\delta_{ps} + \chi^{(3)}_{1221}\delta_{is}\delta_{pr} + \chi^{(3)}_{d}\delta_{iprs},$$

where δ_{ij} denote the Kronecker's delta and $\chi^{(3)}_d = \chi^{(3)}_{11111} - \chi^{(3)}_{1122} - \chi^{(3)}_{1212} - \chi^{(3)}_{1221}$, which denotes anisotropy of nonlinearity. By using $\chi^{(3)}_{1122} = \chi^{(3)}_{1221} = \chi^{(3)}_{1212}$, We rewrite $\chi^{(3)}_{iprs}$ tensor as:

$$\chi^{(3)}_{iprs} = \chi^3 [\frac{\rho}{3}(\delta_{ip}\delta_{rs} + \delta_{ir}\delta_{ps} + \delta_{is}\delta_{pr}) + (1-\rho)\delta_{iprs}]$$

where $\rho = 3\chi^{(3)}_{1122}/\chi^3$. We should note that the magnitude of nonlinear anisotropy is associated with the band structure of material. It has been measured through several methods[106, 107, 108]. For silicon, the value of ρ is close to 1.27 in

the telecom band. In this work, we take $\rho = 1$ for $AlGaAs$ waveguides. Thus, the nonlinear coefficient can be expressed as

$$\gamma_{nklm} = \omega_n \frac{3\varepsilon_0 \chi^3}{\sqrt{I_n I_k I_l I_m}} \times \int_A dA\{\frac{\rho}{3}[(e_n^* \cdot e_m)(e_l^* \cdot e_k) + (e_n^* \cdot e_k)(e_l^* \cdot e_m) + (e_n^* \cdot e_l^*)(e_k \cdot e_m)] + (1-\rho) \sum_{i=x,y,z} e_{ni}^* e_{ki} e_{li}^* e_{mi}\}. \quad (2.3.13)$$

As mentioned before, although the electronic nonlinear susceptibility shows frequency dispersion in special frequency range, however, if the corresponding photon energies are smaller than the band-gap energy of Si, we can say that this frequency dispersion of nonlinear susceptibility χ^3 is small enough to neglect it. As we know, the real and imaginary parts of χ^3 are related to the Kerr coefficient n_2 and the TPA coefficient β_T as:

$$\chi^3 = \frac{4 n_2 \varepsilon \varepsilon_0 c}{3}(1 + i\frac{c\beta_T}{2\omega n_2}) \quad (2.3.14)$$

Substituting 2.3.14 into 2.3.13, we find:

$$\gamma_{nklm} = \omega_n \frac{4\varepsilon_0^2 c}{3\sqrt{I_n I_k I_l I_m}} \times \int_A \varepsilon(\hat{r}) n_2(\hat{r})(1 + i\alpha_T(\hat{r}))\varsigma_{nklm}(\hat{r}) dA, \quad (2.3.15)$$

$$\varsigma_{nklm} = \rho(\hat{r})[(e_n^* \cdot e_m)(e_l^* \cdot e_k) + (e_n^* \cdot e_k)(e_l^* \cdot e_m) + (e_n^* \cdot e_l^*)(e_k \cdot e_m)] + 3(1-\rho(\hat{r})) \sum_{i=x,y,z} e_{ni}^* e_{ki} e_{li}^* e_{mi} \quad (2.3.16)$$

where $\alpha_T = c\beta_T / 2\omega n_2$. All function ς_{nklm} are real and have certain symmetry due to intrinsic permutation symmetry. For instance,$\varsigma_{nklm} = \varsigma_{nmlk} = \varsigma_{lknm} = \varsigma_{knml} = \varsigma_{mlkn} = \varsigma_{mnkl}$. In chapter four, considering this symmetry of ς_{nklm}, a significant reduction is made to simplify the computation of γ_{nklm}.

Based on the above theory, we consider the case of four interacting harmonics, i.e. two pumps and two generated signals. For each harmonic, there exist SPM terms and XPM terms, as well as FWM terms. The resulting coupled

equations are:

$$\frac{da_0}{dz} = i\gamma_{0000}|a_0|^2a_0 + 2i\sum_{i=1,2,3}\gamma_{0ii0}|a_i|^2a_0 + i\gamma_{0121}e^{i(2\beta_1-\beta_2-\beta_0)z}a_1^2a_2^* + 2i\gamma_{0132}e^{i(\beta_1+\beta_2-\beta_3-\beta_0)z}a_1a_3^*a_2,$$

$$\frac{da_1}{dz} = i\gamma_{1111}|a_1|^2a_1 + 2i\sum_{i=0,2,3}\gamma_{1ii1}|a_i|^2a_1 + i\gamma_{1232}e^{i(2\beta_2-\beta_3-\beta_1)z}a_2^2a_3^* + 2i\gamma_{1012}e^{i(\beta_0+\beta_2-2\beta_1)z}a_0a_2a_1^* + 2i\gamma_{1023}e^{i(\beta_0+\beta_3-\beta_1-\beta_2)z}a_0a_2^*a_3,$$

$$\frac{da_2}{dz} = i\gamma_{2222}|a_2|^2a_2 + 2i\sum_{i=0,1,3}\gamma_{2ii2}|a_i|^2a_2 + i\gamma_{2101}e^{i(2\beta_1-\beta_0-\beta_2)z}a_1^2a_0^* + 2i\gamma_{2123}e^{i(\beta_1+\beta_3-2\beta_2)z}a_1a_3a_2^* + 2i\gamma_{2013}e^{i(\beta_0+\beta_3-\beta_1-\beta_2)z}a_0a_1^*a_3,$$

$$\frac{da_3}{dz} = i\gamma_{3333}|a_3|^2a_{03} + 2i\sum_{i=0,1,2}\gamma_{3ii3}|a_i|^2a_3 + i\gamma_{3212}e^{i(2\beta_2-\beta_1-\beta_3)z}a_2^2a_1^* + 2i\gamma_{3102}e^{i(\beta_1+\beta_2-\beta_3-\beta_0)z}a_1a_0^*a_2, \quad (2.3.17)$$

where a_1, a_2 denote the pump amplitudes and a_0, a_3 correspond to signal and idler waves. Note that all of the γs strongly vary with the wavelength. In chapter 3, to address this, we compute these γs for different geometries. Because of the big difference between these γs, the modulation instability happens within normal dispersion region even when $\delta\beta < 0$.

As discussed in section 2.2 and reference[1], theoretical description of CW and pulse propagation in conventional fibers or waveguides is mainly based on the well-known generalized Nonlinear Schrodinger equation, which only includes self-steepening term (the first-order term of nonlinear dispersion). To explain how the dispersion of nonlinearity could affect modulation instability in subwavelength waveguides, in this section, a new model has been derived for CW. In equation 2.3.12, we neglect the time dependence of the amplitudes

of the field components due to quasi-CW conditions. However, if we need to describe modulation instability of optical pulses, then the effect of GVD has to be included into our model. We should note that the group velocity of pulses participating in the four-wave mixing process can be quite different. Thus, efficient FWM needs not only phase matching but also matching of the group velocities.

Following the same procedure as demonstrated above and in references[90], by using Fourier expansion for the electric field:

$$\Xi(\overrightarrow{r},t) = \frac{1}{\sqrt{2\pi}} \int E(\overrightarrow{r},\omega) e^{-i\omega t} d\omega + c.c,$$

where each harmonic is described in terms of slowly varying amplitude $A_\omega(z)$ of the corresponding linear mode $e_\omega(x,y)$:

$$E(\overrightarrow{r},\omega) = I_\omega^{-1/2} A_\omega(z) e_\omega(x,y),$$

where $I_\omega = \int\int_{-\infty}^{+\infty} (e_\omega \times h_\omega^* + e_\omega^* \times h_\omega)\hat{e_z} dxdy$, we derive equations for the harmonic amplitudes:

$$i\partial_z A_\omega = -\beta_\omega A_\omega - \frac{\omega}{2\pi} \int\int \Gamma_{\omega\omega_1\omega_2\omega_3} A_{\omega_1} A_{\omega_2}^* A_{\omega_3} d\omega_1 d\omega_2, \qquad (2.3.18)$$
$$\omega_3 = \omega - \omega_1 + \omega_2$$

where β_ω is the propagation constant at the corresponding frequency for the linear guided mode, and the nonlinear coefficients are given by:

$$\Gamma_{nklm} = \frac{\varepsilon_0}{\sqrt{I_n I_k I_l I_m}} \times \int_A \chi_{nklm} \varsigma(\hat{r}) dA, \qquad (2.3.19)$$

where $\varsigma(\hat{r})$ is defined above. Note that the actual nonlinear coefficients are given by:$\gamma_{nklm} = \omega_n \Gamma_{nklm}$. As discussed before, It is reasonable to assume that $\chi_{nklm} = (3/4)\varepsilon_0 \varepsilon c n_2$ as the nonlinear material dispersion is usually weak. Therefore, the Kerr coefficient n_2 and dielectric permittivity ε are evaluated at a reference frequency $\omega_0 = 2\pi c/\lambda_0$. On the contrary, we expect that the geometrical dispersion of nonlinearity is strong and could make big impact on nonlinear effects, such as modulation instability, soliton, in sub-wavelength

waveguides.

Below, in chapter 3 and chapter 4, the role of dispersion of nonlinearity resulting from geometrical dispersion of nonlinearity is investigated based on our new model 2.3.12 in sub-wavelength semiconductor waveguides for CW and pulse wave.

2.4 Summary

Linear dispersion causing linear chirp can compensate the nonlinear chirp induced by nonlinearity, thus leading to soliton, which is very important nonlinear phenomenon in optical fibers or waveguides. Furthermore, linear phase mismatch resulting from linear dispersion plays a critical role during the process of FWM. Thanks to these, in this chapter, we discussed how to engineer the dispersion in sub-wavelength waveguides with high index together with the origin of linear dispersion and nonlinearity.

We derived the new model governing evolution of the amplitudes of components of the optical waves interacting in the waveguides for CW and pulse wave using perturbation expansion method. The new MI condition is found, as we take into account the dispersion of nonlinearity which is enhanced through a strong variation of the modal profile with the wavelength of light in sub-wavelength waveguides in chapter 3.

In our model, we don't consider the effects of TPA and free carrier. This is because there are two approaches which could reduce the influence of TPA and free carrier. One is that, by applying external electric field, the free carrier can be removed. In addition, by changing the waveguide geometry (slot waveguide) or material and varying the operating wavelength, we can reduce effect of TPA or completely eliminate it. For instance, TPA can be ignored at wavelength $\lambda > 1.5\mu m$ for AlGaAs waveguide[48] and at wavelength $\lambda > 2\mu m$ for Silicon waveguide[49].

Chapter 3

Modulation instability induced by nonlinear dispersion for continuous wave

The models describing nonlinear light propagation in sub-wavelength waveguides have been investigated extensively[109, 110, 86, 87, 111, 112]. As one of important nonlinear phenomena, FWM[113, 114, 115, 93] has been first explored in conventional fiber. The main characteristics of FWM can be understood from the equations (2.2.10),(2.2.11). As we mentioned before, formally, the effective core area A_{eff} is a function of the wavelength as the modal profiles can change significantly. However, the variation of the effective core area is negligible in conventional single-mode fibers since the transverse scales involved are relatively large compared to the wavelength. Dispersion of nonlinearity hasn't gained much attention in many works, in particular, when one studies the FWM in silica fiber.

In the process of FWM, to achieve efficient FWM, Phase matching is very important. From equations 2.2.9 and 2.2.10, in order to cancel the mismatch resulting from nonlinear effects, $\delta\beta$ should be positive, where $\delta\beta$ represents the mismatch caused by material dispersion and waveguide dispersion. Based on these considerations, during the past few years, FWM has been studied extensively[93, 118, 119, 94, 120][60, 61, 62, 63, 64, 65, 66, 67, 68, 69, 70, 71, 88, 121].

Recently, due to advances in the fabrication of photonic-crystal fibers (PCFs)[18,

19, 116], the fibers with the wavelength scale core areas have been produced. Compared with conventional fibers, the dispersion characteristics were strongly modified. As a consequence, the FWM phase matching conditions are quite different from those seen in conventional fibers. For small core PCFs, Strong nonlinear interactions occur at relatively low peak powers and over short propagation distances. The other kind of fiber is tapered fibers[117] (TFs), which are made by heating and stretching conventional fibers. The dispersion characteristics of TFs are very similar to those in small-core PCFs, which means the GVD profiles of PCFs and TFs are similar, because, in a typical index-guiding PCF, most of the light is guided in a tiny core surrounded by a periodic structure of large air-filled holes separated by thin membranes. In a word, the photonic crystal fibers[18, 19, 116], tapered[117] fibers and even doped fibers[118] have high nonlinearity, as well as offer opportunities for engineering of dispersion. Soon after their successful fabrication and development, these highly nonlinear fibers have been used for efficient FWM[93, 118, 119, 94, 120]. Most of the results in these papers can be understood within the framework of the idealized nonlinear Schrodinger equation, which we have already reviewed in previous section. On the other hand, FWM theory has been developed based on the full wave equation[93].

Due to favorable optical, electronic, and physical properties of silicon and CMOS fabrication processing technology compatible with silicon, significant research effort has been put into silicon-based nanophotonic devices[44, 46, 45]. During the past few years, from fiber[113, 114, 115, 93] to Silicon-on-insulator (SOI) photonic nanowires[60, 61, 62, 63, 64, 65, 66, 67, 68, 69, 70, 71, 88, 121], FWM attracted significant attention because of its potential applications in all-optical switches, optical signal regenerators, high-speed optical networks, and optical sources for quantum information technology. Developing an optical amplifier and frequency conversion based on silicon waveguide are important for the success of SOI photonic integrated circuits. Through the process of phase-matched FWM in suitably designed SOI waveguide, optical amplifier[121] can be acquired. Compared with Raman gain bandwidth[122], more broad conversion bandwidth has been obtained[121], which allows for the implementation of dense wavelength division multiplexing and demultiplexing in silicon waveguides. In fiber-optic communication, wavelength-division multiplexing (WDM)

is a technology which combines a number of optical carrier signals onto a single optical waveguide by using different wavelengths of laser light. A WDM system uses a multiplexer at the transmitter to join the signals together, and a demultiplexer at the receiver to split them apart. The demultiplexer tends to be wideband devices. It must provide the wavelength selectivity of the receiver in the WDM system. Exploiting FWM, error-free 640 Gbit/s demultiplexing has been demonstrated[123].

As discussed in preceding section, efficiency of FWM is limited by TPA and free carrier. Therefore, it is not easy to realize the net gain in silicon waveguides. However, the recent work[121] shows that the parametric gain can be obtained if the SOI waveguides can be designed properly [121, 67]. In addition, using a single silicon waveguide with $700nm \times 425nm$ cross section and mid-infrared pump, due to reducing the impact of two photon absorption, high gain and broad bandwidth can be achieved[124].

Also, FWM has been observed in SOI waveguides with normal GVD due to higher-order dispersion[63, 66, 68]. However, the bandwidth is very narrow and the conversion efficiencies are lower[63, 66, 68]. By tailoring waveguide dispersion, broad gain bandwidths and efficient wavelength conversion have been achieved via phase-matched FWM[71, 88, 125] by using a CW pump. It is worth mentioning that, in the theoretical part of these papers, γ is only decided by the pump frequency although there are three interacting waves inside the waveguide. In another word, so far, for the most of investigations of FWM in silicon waveguide, the dispersion of nonlinearity hasn't caused much attention because of the reasons presented above. In this work, through the new model 2.3.12 derived in chapter 2, significant difference is made to the modulation instability condition for the sub-wavelength waveguide. Thus the new mechanism supporting FWM is addressed below.

The main results in this chapter can be found in our paper[126].

3.1 Parametric gain and dispersion of nonlinearity

We consider only a single pump a_1, while, a_0, a_2 correspond to signal and idler wave, respectively. Equations 2.3.17 are quite general because they include

the SPM, XPM, and pump depletion due to the FWM. If we assume that the pump field is strong enough to remain undepleted during the process of FWM, and signal and idler are weak, then we get the following coupled equations:

$$\frac{da_1}{dz} = i\gamma_{1111}|a_1|^2 a_1 \tag{3.1.1}$$

$$\frac{da_0}{dz} = 2i\gamma_{0110}|a_1|^2 a_0 + i\gamma_{0121}e^{i(2\beta_1-\beta_2-\beta_0)z}a_1^2 a_2^* \tag{3.1.2}$$

$$\frac{da_2}{dz} = 2i\gamma_{2112}|a_1|^2 a_2 + i\gamma_{2101}e^{i(2\beta_1-\beta_0-\beta_2)z}a_1^2 a_0^*. \tag{3.1.3}$$

By assuming that $\delta\beta = 2\beta_1 - \beta_2 - \beta_0$, and initial power $p = |a(0)|^2$, through several basic calculations, one can easily obtain two coupled equations for signal and idler fields:

$$\frac{da_0}{dz} = 2i\gamma_{0110}pa_0 + i\gamma_{0121}e^{i\delta\beta z}e^{2i\gamma_{1111}pz}pa_2^* \tag{3.1.4}$$

$$\frac{da_2}{dz} = 2i\gamma_{2112}pa_2 + i\gamma_{2101}e^{i\delta\beta z}e^{2i\gamma_{1111}pz}pa_0^*. \tag{3.1.5}$$

To solve these equations, we introduce:

$$a_0 = A_0(z)e^{2i\gamma_{0110}pz} \tag{3.1.6}$$

$$a_2 = A_2(z)e^{2i\gamma_{2112}pz}, \tag{3.1.7}$$

where $A_{0,2} \sim e^{gz}$. By using equation 3.1.4 through 3.1.7, we then obtain the parametric gain depending coefficient in the form:

$$g = \frac{1}{2}Re(\sqrt{(4\Gamma_+ p - \delta\beta)(\delta\beta - 4\Gamma_- p)}) \tag{3.1.8}$$

where

$$\Gamma_+ = \frac{\gamma_{0110} + \gamma_{2112} + \sqrt{\gamma_{0121}\gamma_{2101}} - \gamma_{1111}}{2} \tag{3.1.9}$$

$$\Gamma_- = \frac{\gamma_{0110} + \gamma_{2112} - \sqrt{\gamma_{0121}\gamma_{2101}} - \gamma_{1111}}{2}. \tag{3.1.10}$$

From equations 3.1.8-3.1.10, after performing simple calculations, the modulation instability condition $g > 0$ can be expressed as follows:

$$4\Gamma_{-}p < \delta\beta < 4\Gamma_{+}p \tag{3.1.11}$$

We write the threshold power in terms of $\Gamma_{\pm}$:

$$p_{critical1} = \frac{\delta\beta}{4\Gamma_{-}}$$

$$p_{critical2} = \frac{\delta\beta}{4\Gamma_{+}}$$

By taking $\gamma_{0110} = \gamma_{2112} = \gamma_{0121} = \gamma_{2101} = \gamma$, we find $\Gamma_{+} = \gamma, \Gamma_{-} = 0$. Thus, the conventional condition $\delta\beta > 0$ is recovered.

Before we discuss how Γ_{-} makes impact upon modulation instability in details by numerical calculation, we first look through the new conditions 3.1.11. Γ_{-} is a very essential parameter for gain spectrum since the gain range strongly depends on the Γ_{-}. $\Gamma_{-} \neq 0$ because of the dependence of nonlinear coefficients on frequencies, i.e., ω_p,ω_s,ω_i. However, the value of γ_{nklm} is determined by the complex overlap integrals, which we will calculate below. Importantly, Γ_{-} can be negative. Therefore, even if $\delta\beta$ is negative, the growth rate of modulation instability still can happen providing $p > p_{critical1}$. From the equation 3.1.11, one can see that, if Γ_{-} is a small negative number, then $\delta\beta$ should be very small negative number as well in order to realize the FWM under the low power condition. Consequently, minimizing the value of $\delta\beta$ becomes very crucial by engineering the dispersion of waveguides in subwavelength waveguide. Notably, when $\Gamma_{-} < 0$, our task is that we need larger absolute value of Γ_{-} , and on the other hand, smaller absolute value of $\delta\beta$ in order to satisfy the MI condition for practical power.

It is important to emphasize that tight optical-field confinement achieved in sub-wavelength silicon waveguide results in a strong dependence of the waveguide mode profiles and their propagation constant of these structures on both waveguide geometry and the corresponding material parameters. Similar to the linear optical properties of silicon waveguides, we expect that the nonlinear properties of silicon waveguide also show large frequency dispersion, which

means the nonlinear dispersion is too large to ignore it. To achieve these, we need to calculate the waveguide modes and the corresponding propagation constant at frequency ω_p,ω_s ,ω_i, and then use Equations 2.3.15 and 3.1.8 to calculate the nonlinear coefficient γ and gain, respectively.

3.2 Nonlinear coefficient γ

In chapter 2 and section 3.1, by considering the dispersion of nonlinearity in semiconductor waveguides, the new MI condition has been found through calculating the overlap integrals. In our theory, the dispersion of γ_{nklm} is defined by the three distinct contributions. First, it is from the material dispersion of the $\chi^{(3)}$ tensor; second, is from the geometrical dispersion induced by the dependencies of the modal profiles and of the overlap integrals on the value of $\omega_{p,s,i}$; third, is that each γ_{nklm} is trivially proportional to ω_n. The latter factor on its own makes $\Gamma_- \sim \omega_p - \sqrt{\omega_p^2 - (\omega_p - \omega_s)^2} > 0$ and hence can not create MI gain with negative $\delta\beta$. Thus to achieve $\Gamma_- < 0$, one has to rely on the material and geometrical contributions to the dispersion of nonlinearity. The material dispersion is usually weak and also poorly characterized in terms of its variations with multiple frequencies. On the contrary, geometrical dispersion is expected to be strong and also controllable with the waveguide geometry and choice of the operating wavelength. Below we calculate γ_{nklm} in some ordinary waveguide geometries. Hereafter we take $\chi^{(3)} = \chi = (4/3)\varepsilon_0\varepsilon c n_2$, where n_2 is the constant Kerr coefficient and $\varepsilon = \varepsilon(\omega_p)$. The geometrical dispersion is accounted for by computing guided modes (Figure. 3.2.1) at the required frequencies with the help of the Comsol's Maxwell solver.

Value of γ_{nklm} and dispersion are strongly correlated with waveguide geometry for silicon nanowires. Here, we take $\gamma_p = \gamma_{1111}, \gamma_{sp} = \gamma_{0110}, \gamma_{ip} = \gamma_{2112}, \gamma_{4s} = \gamma_{0121}, \gamma_{4i} = \gamma_{2101}$.

We first compute the γ_p as a function of pump wavelength. As is shown in Figure 3.2.2, the value of γ_p changes with wavelength notably. Through comparison of $\gamma_p^{'}$s for three geometries, we found that the γ_p rapidly drops with the decrease of the width of the waveguides from shorter to longer wavelength, which implies that, for waveguide with small cross-section, the nonlinear dispersion term $\partial_\omega^2\gamma_p$, which is second derivative of γ_p, can make big influence on

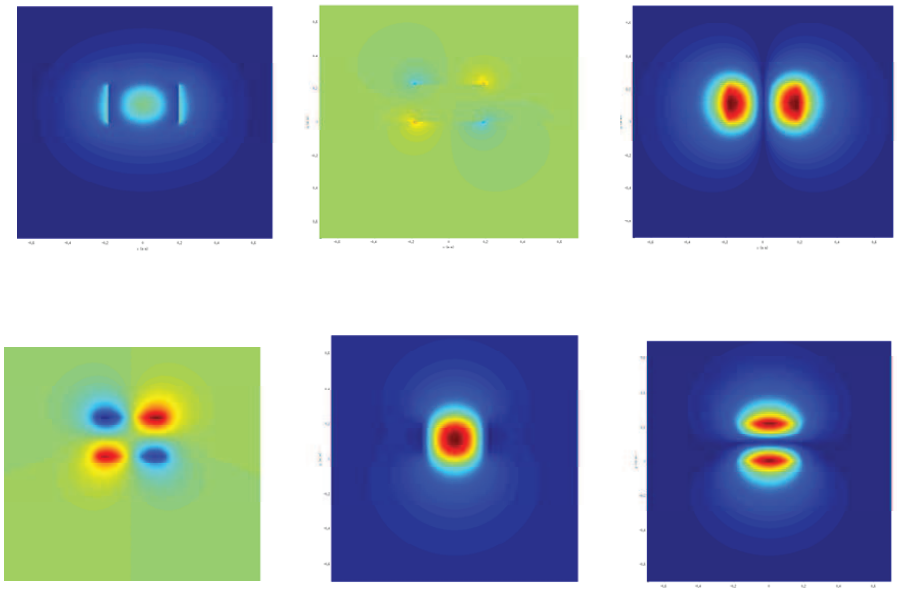

Figure 3.2.1: The profile of guided mode for $380nm \times 220nm$ SOI waveguide at pump wavelength λ_p=1.55μm. from left to right , in the first row, E_x, E_y, E_z. In the second row, H_x, H_y, H_z.

MI. We will return to this issure in the section 3.4.

Below, we calculate all of the γ_{nklm} for a given pump wavelength and waveguide geometry. As an example, we first consider a single $700nm \times 220nm$ SOI waveguide. As we kow, bulk silicon exhibits normal dispersion over its transparent spectral region. However, the dispersion can change dramatically if the GVD resulting from a strong optical mode confinement is used to compensate for the material GVD. In the following, we calculate the dispersion by using Comsol. Figure 2.1.1 in chapter 2 shows dispersion curve of the $700nm \times 220nm$ waveguide. It is clear to see that the first zero-GVD point is about $1.435\mu m$ and the second zero-GVD is $2.24\mu m$. The dispersion is expressed in units of $ps/nm \cdot km$.

From Equation 2.3.16, to calculate γ_{nklm}, one can find that we need to know the modes corresponding to pump, signal and idler wave. Here, we choose pump wavelength to be $1.55\mu m$, which is located in the anomalous GVD range. Figure 3.2.1 shows the fundamental mode propagating inside silicon waveguide. In our calculations, we take $n_2 = 4 \times 10^{-18} m^2/W$ [90]. The result is demonstrated in figure 3.2.3. As we expect, the difference between

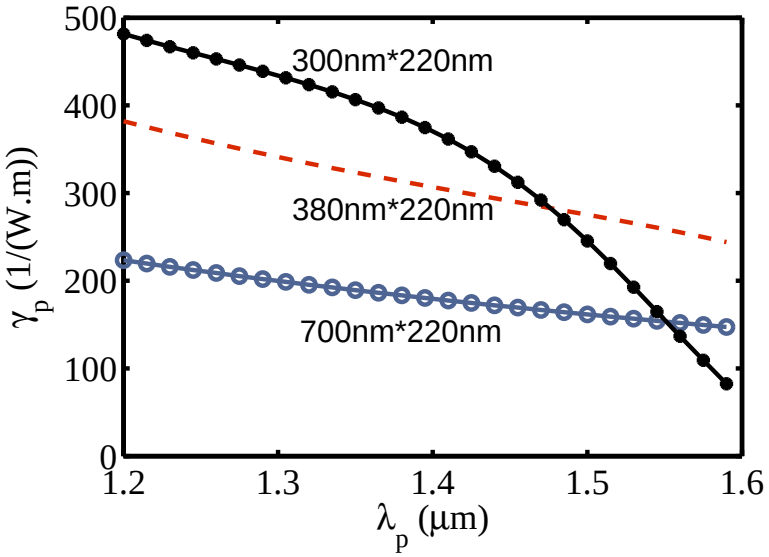

Figure 3.2.2: γ_p as function of pump wavelength λ_p. the black curve with dot, the dashed line and the blue curve with circle correspond to single $300nm \times 220nm, 380nm \times 220nm, 700nm \times 220nm$ SOI waveguide, respectively.

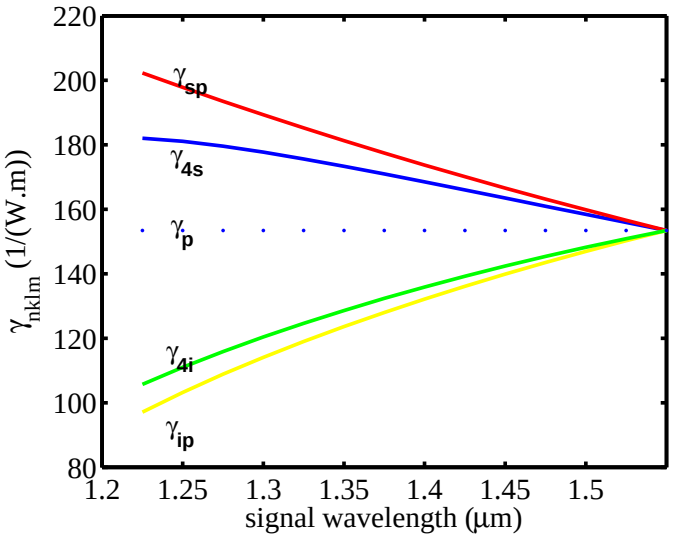

Figure 3.2.3: The plot of value of γ_{nklm} as function of signal wavelength for $700nm \times 220nm$ SOI waveguide. The pump wavelength is $1.55\mu m$, which is within anomalous GVD range.

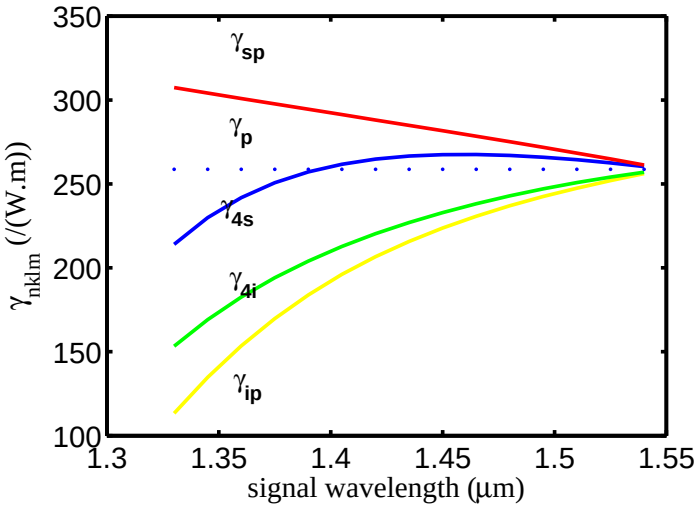

Figure 3.2.4: The plot of value of γ_{nklm} as function of signal wavelength for $380nm \times 220nm$ SOI waveguide. The pump wavelength is $1.55\mu m$, which is within anomalous GVD range.

γ_{nklm} is very pronounced. With decrease of signal wavelength, γ_{ip} and γ_{4i} go down to about $89/mW$ and $98/mW$, respectively. Obviously, γ_{sp} and γ_{4s} go up to $202/mW$ and $178/mW$, respectively.

Next, to further see the variations of γ_{nklm} with wavelength and waveguide geometry, by decreasing the width of waveguide, and fixing the height of waveguide, again, we calculate the γ_{nklm} for $380nm \times 220nm$ SOI waveguide. Pump wavelength is $1.55\mu m$ located in the anomalous GVD regime. Compared with values of γ_{nklm} in Figure 3.2.3, Figure 3.2.4 shows that γ_{ip}, γ_{4i},γ_{4s} decrease quickly with increase of signal frequency. From equation 2.3.16, we find that, to compute these three $\gamma_{nklm}s$, the modes corresponding to idler wavelengths needs to be calculated (for $\gamma_{p}$and γ_{sp} , only the modes of pump and signal waves are needed.). In particular, for a subwavelength silicon waveguide, the modes become less confined for the larger wavelength (idler wave). Especially, as idler wavelength is close to the cutoff wavelength, only a smaller amount of optical power is guided within the region with optical nonlinearity, which leads to decrease of γ_{nklm} related to the mode of idler wave.

Figure 3.2.5 shows the same trend as in Figure 3.2.4. However, a major concern is given to the linear mismatch $\delta\beta$ for $300nm \times 220nm$ waveguide. we choose that pump wavelength is $1.4\mu m$ in the normal GVD range. (The

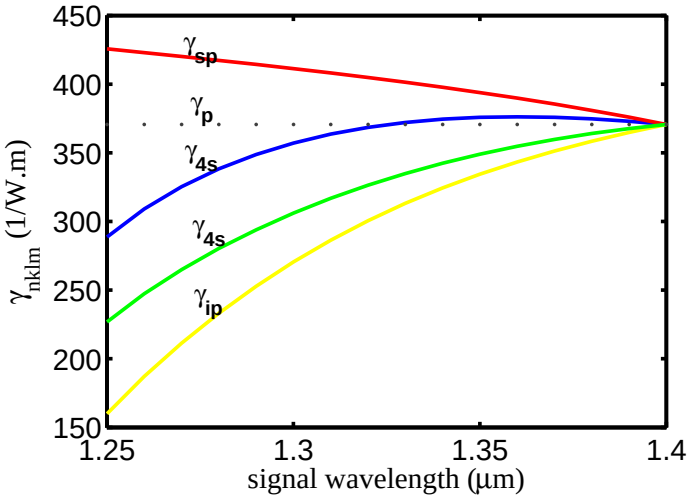

Figure 3.2.5: The plot of value of γ_{nklm} as function of signal wavelength for $300nm \times 220nm$ SOI waveguide. The pump wavelength is $1.4\mu m$, which is within normal GVD range.

dispersion curve has been shown in Figure 2.1.1, we will be back to this case in the following section). It is necessary to emphasize that $\delta\beta < 0$ from our calculation. According to standard theory, MI gain doesn't exist if $\delta\beta < 0$. However, as will be discussed below, due to these significant differences between these γ_{nklm}, which account for nonlinear dispersion, the MI happens in this case.

As a final consideration in this subsection, based on our values of γ_{nklm}, which have been obtained above, we calculate Γ_- for $700nm \times 220nm$ and $380nm \times 220nm$ SOI waveguides, specifically. By employing expression 3.1.10, which we derived in section 3.1,Γ_- responsible for the occurrence of MI when $\delta\beta < 0$ is evaluated. Figure 3.2.6 shows same interesting results. For a fixed pump wavelength $1.55\mu m$, the values of Γ_- are always positive for $700nm$ by $220nm$ waveguide, which means MI gain can not happen if $\delta\beta < 0$ in this case. The same conclusion has been made by using the standard theory. In addition, we calculated Γ_- at pump wavelength $1.55\mu m$ for a SOI waveguide with cross-section of $500nm$ by $220nm$ and we found the same result (The dispersion curve also has been shown in Figure 2.1.1). However, for $380nm \times 220nm$ SOI waveguides, Figure 3.2.6 shows totally different behavior. Within the whole wavelength range, Γ_- is always negative, which means the gain can exist even

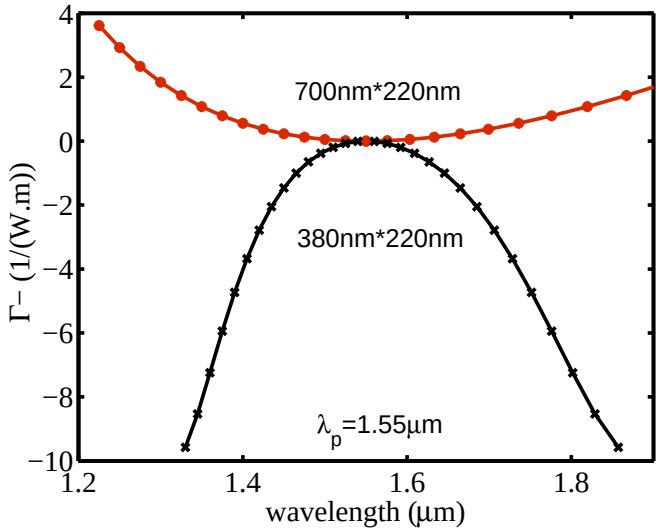

Figure 3.2.6: The plot of value of Γ_{-}as function of wavelength for $700nm \times 220nm$ (red curve with dot)and $380nm \times 220nm$ (black curve with cross) SOI waveguides. (Pump wavelength is $1.55\mu m$ for two cases.)

if $\delta\beta < 0$ as long as we choose an appropriate power.

The results predicted by our model shed light on the occurrence of MI supported by the new mechanism. In the following section, with the help of the Comsol's solver, numerically, we compute Γ_{-} and corresponding gain spectrum for several sub-wavelength waveguides.

3.3 Modulation instability due to dispersion of nonlinearity

As discussed in preceding chapter, if we operate specific wavelength near to the Zero-GVD point, where $\beta_2 \sim 0$, the effect of fourth-order dispersion will become essential for a large frequency offsets. In the standard theory, only when the instability condition $0 < \delta\beta < 4\gamma p$ is satisfied, MI could occur in this system. Especially, In normal GVD regime, $\beta_2 > 0$, the instability condition may be satisfied if $\beta_4 < 0$, and furthermore, in this case, the generated signal and idler frequencies through process of MI can not be close to the pump frequency as only large frequency offset can cancel out β_2 and make $\delta\beta > 0$.

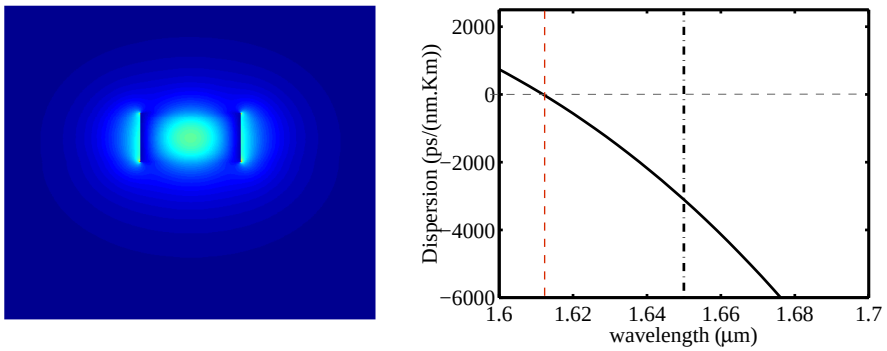

Figure 3.3.1: Guided mode of $380nm \times 220nm$ SOI waveguide : in the left, profile of the dominant electric field component (e_x) at $\lambda_p = 1.65\mu m$. In the right, calculated GVD, $D = -2\pi c\beta_2/\lambda^2$, Black dash-dot line indicates the pump wavelength and red dashed line represents Z-GVD point.

On the contrary, based on new instability condition 3.1.11, in this section, we will investigate the MI gain when $\delta\beta < 0$. Note again that $\delta\beta$ refers to the linear phase mismatch.

3.3.1 Modulation instability for $380nm \times 220nm$ SOI waveguide

To demonstrate how our unique MI condition 3.1.11 works, in particular, we choose the pump wavelength located in the normal GVD range, which can ensure $\delta\beta < 0$. On the other hand, we also found that, in anomalous dispersion regime, broader gain bandwidth can be acquired if we take dispersion of nonlinearity into account (make sure that $\Gamma_- < 0$) when $\delta\beta < 0$ at a specific signal wavelength where the parametric gain becomes zero using the standard theory.

As our first example, we consider a SOI waveguide with cross-section of $380nm \times 220nm$. The geometry and the mode profile (dominant electric field component is oriented horizontally) are shown in Figure 3.1.1. The GVD of this mode is normal for $\lambda > 1.612\mu m$. In order to apply our new theory, we choose that the pump wavelength is $1.65\mu m$, which is sufficiently far from the Z-GVD point. Thus, the second-order dispersion $\beta_2 > 0$ and $D = -3200ps/nm/Km$.

The black full curve in Figure 3.3.2(a) shows the plot of $\delta\beta$ as function of

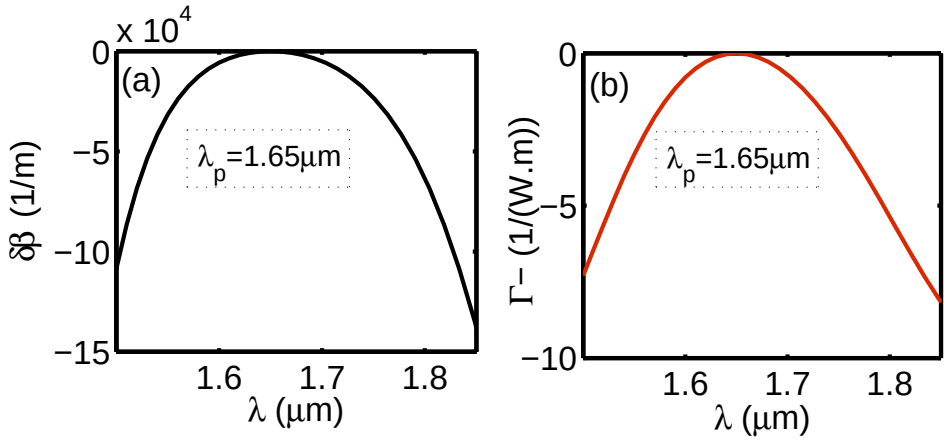

Figure 3.3.2: The plot of values of $\delta\beta$ and Γ_- as functions of signal and idler wavelengths at $\lambda_p = 1.65\mu m$ for $380nm \times 220nm$ SOI waveguide. $n_2 = 4 \times 10^{-18} m^2/W$,$D = -3200 ps/nm/Km$.

the signal and idler wavelengths for $\lambda_p = 1.65\mu m$. One can see that, across the whole wavelength range, $\delta\beta$ always negative, thus MI can be supported only through the mechanism related to the nonlinear dispersion and can happen only if $\Gamma_- < 0$. Fortunately, $\Gamma_-$is negative everywhere within the broad range of the signal and idler wavelengths from our calculation shown in Figure 3.3.2(b). Thus, by increasing the pump power p, the MI condition 3.1.11 always can be satisfied.

Figure 3.3.3 shows parametric gain together with threshold pump power $p_{th}(\lambda_p)$ (red dashed curve). However, unfortunately, to acquire this kind of parametric gain, a sufficiently high threshold pump power, which is about $1600W$, is required. Also, one should remember that TPA and free carriers in silicon can degrade the gain resulting from dispersion of nonlinearity.

Note that, to qualitatively estimate the impact of material dispersion of $\chi^{(3)}$ on MI, we also calculated $p_{th}(\lambda_p)$ by using $\chi_{nklm} = (4/3)\varepsilon_0 \varepsilon \bar{\omega}_{nklm} c n_2$, where $\bar{\omega} = (\omega_n + \omega_k + \omega_l + \omega_m)/4$. This gave only negligible deviations from the results shown in Figure 3.3.3, thus confirming the dominant role of the geometrical dispersion of nonlinearity. Therefore, in the following section, we ignore material dispersion of $\chi^{(3)}$.

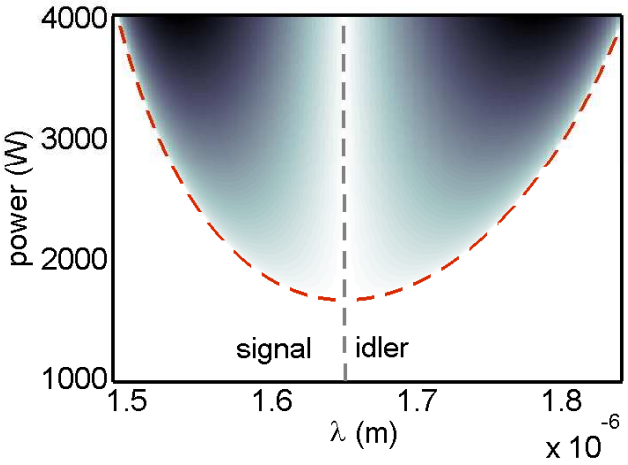

Figure 3.3.3: Plot of gain as function of pump power and signal/idler wavelengths. Dashed lines show the threshold power $p_{th} = \delta\beta/(4\Gamma_{-})$; Geometry is same as Figure 3.3.1. In the shaded area, darker colours indicate the larger values of gain.

3.3.2 Modulation instability for $300nm \times 220nm$ SOI waveguide

In this section, we continue to seek the optimal geometry to implement our theory under low pump power in order to reduce the impacts of TPA and free carriers in silicon waveguide. $300nm \times 220nm$ SOI waveguide is employed. The profile of confined mode is similar to the mode in Figure 3.3.1. From Figure 3.3.4, for $\lambda_p > 1.38\mu m$, the waveguide exhibits normal dispersion since $D < 0$. To obtain negative $\delta\beta$, we still choose pump wavelength $\lambda_p = 1.4\mu m$ located in normal GVD regime. One can see that $\delta\beta$ is negative everywhere from Figure 3.3.5(a). In the case of negative $\delta\beta$, MI can be induced only by dispersion of nonlinearity in terms of our new findings.

Consequently, the sign of Γ_{-}becomes essential for MI to exist. Figure 3.3.5(b) shows that Γ_{-} is negative within the range of the signal and idler frequencies which we are concerned. Compared with the values of Γ_{-} in Figure 3.3.2, the absolute values of Γ_{-} becomes larger in this case, which means we can use lower pump power to generate parametric gain based on MI condition 3.1.11. The Figure 3.3.6 further proves this prediction. The generated gain and the threshold power $p_{th}(\lambda_p)$ (red dashed curve) are shown in Figure 3.3.6.

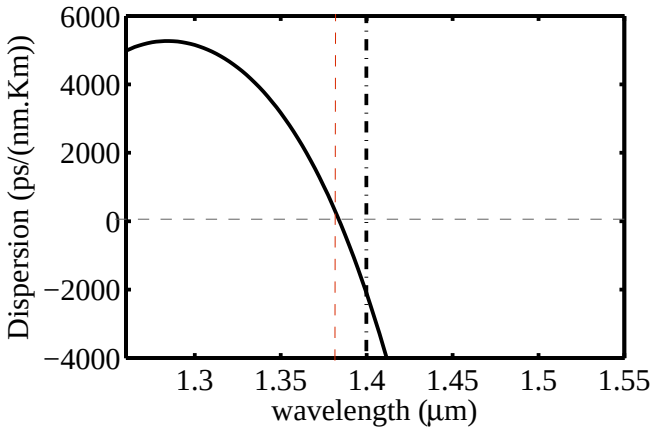

Figure 3.3.4: The plot of GVD, $D = -2\pi c\beta_2/\lambda^2$, Black dash-dot line indicates the pump wavelength $\lambda_p = 1.4\mu m$. Red dashed line represents Z-GVD wavelength.

The lower threshold power $500W$ has been found by using $p_{th} = \delta\beta/(4\Gamma_-)$.

We also consider a $380nm \times 220nm$ silicon waveguide with polymer cladding. In this case, the value of the dispersion parameter D is always negative within the whole range of wavelength and $\delta\beta < 0$. At pump wavelength $\lambda_p = 1.375\mu m$, We found that $\Gamma_-$is always positive within the whole wavelength regime. Thus, no MI happens in this waveguide.

3.3.3 Modulation instability for $300nm \times 500nm$ AlGaAs waveguide

As mentioned above, TPA and free carrier induced by external field can bring significant impact on MI in SOI waveguide. Thus, observing the MI gain becomes difficult in practice. As we know, for AlGaAs waveguide, TPA[48] is negligible when the operation wavelength is larger than $1.5\mu m$.

As another example, we consider a suspended $Al_{0.25}Ga_{0.75}As$ waveguide. Again, the geometry and profile of the guided modes at $\lambda_p = 1.7\mu m$ (dominant electric field component is oriented horizontally) are shown in Fig. 3.3.7(a). The GVD of this mode is normal for $\lambda > 1.66\mu m$, see Figure 3.3.7(b).

The full black curve in Figure 3.3.8(a) shows the plot of $\delta\beta$ as function of the signal and idler wavelengths for $\lambda_p = 1.7\mu m$. One can see that $\delta\beta$ is negative everywhere. Hence MI can be provided only through the mechanism

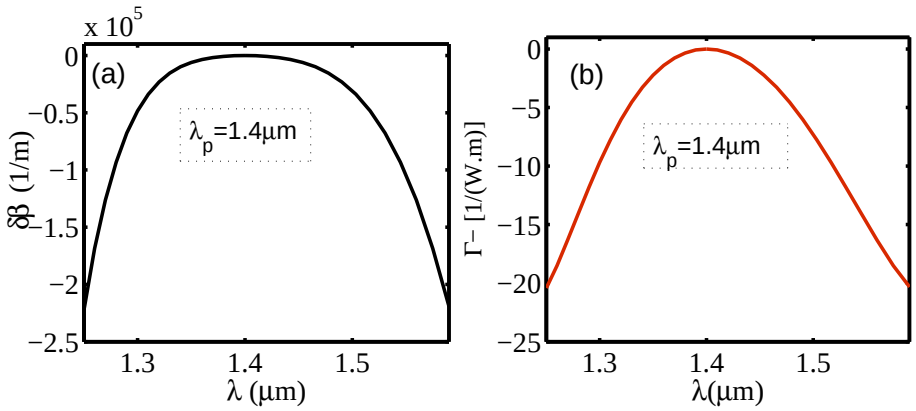

Figure 3.3.5: Plot of $\delta\beta$and Γ_- as function of signal and idler wavelengths at $\lambda_p = 1.4\mu m$ for $300nm \times 220nm$ SOI waveguide. $n_2 = 4 \times 10^{-18} m^2/W$,$D = -2200 ps/nm/Km$.

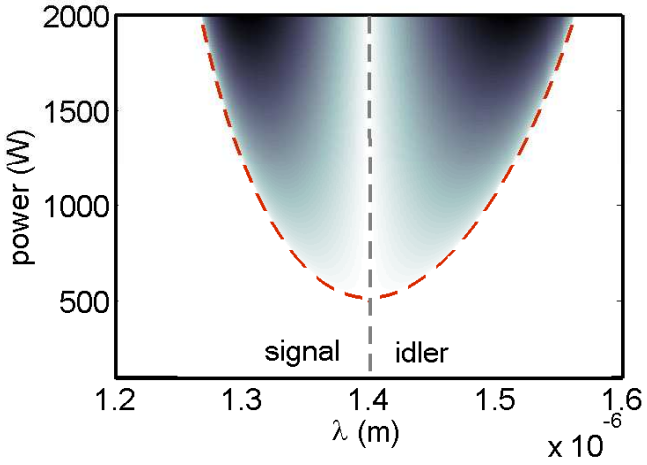

Figure 3.3.6: Plot of gain as function of pump power and signal/idler wavelengths. Dashed lines show the threshold power $p_{th} = \delta\beta/(4\Gamma_-)$; Geometry is same as Figure 3.3.5. In the shaded area, darker colors indicate the larger values of gain.

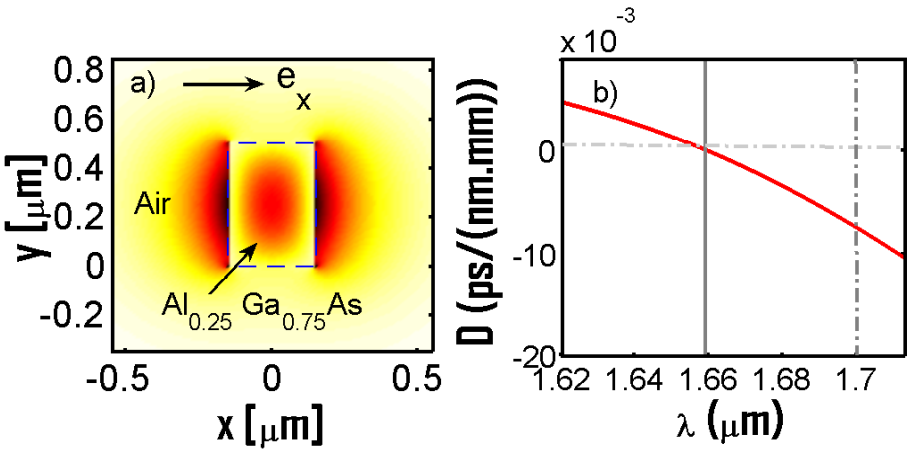

Figure 3.3.7: Guided mode of $Al_{0.25}Ga_{0.75}As$ waveguide suspended in air: (a) profile of the dominant electric field component (e_x) at $\lambda_p = 1.7\mu m$ for $500nm \times 300nm$. Waveguide is indicated by dashed lines; (b) The plot of GVD, $D = -2\pi c\beta_2/\lambda^2$. Grey dash-dot line indicates the pump wavelength $\lambda_p = 1.7\mu m$. Grey line represents Z-GVD wavelength.

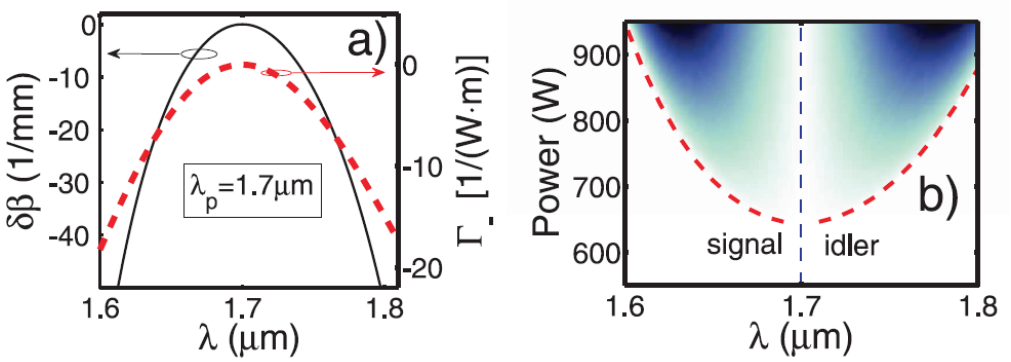

Figure 3.3.8: MI in $Al_{0.25}Ga_{0.75}As$ waveguide: (a) $\delta\beta$ and Γ_- at $\lambda_p = 2\pi c/\omega_p = 1.7\mu m$ as functions of the signal/idler wavelengths. $n_2 = 1.5 \times 10^{-17} m^2/W$, $D = -0.07 ps/nm/mm$; (b) gain as function of pump power and signal/idler wavelengths, g > 0 within shaded areas with darker colors corresponding to larger values of g. Red dashed lines show the threshold power $p_{th} = \delta\beta/(4\Gamma_-)$;

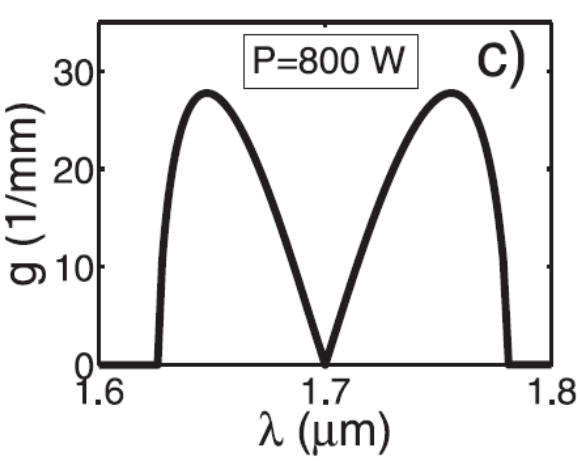

Figure 3.3.9: The plot of gain as function of signal/idler wavelength for $P = 800W$ at pump wavelength $\lambda_p = 1.7\mu m$.

related to the dispersion of nonlinearity and is possible only if $\Gamma_- < 0$. Γ_- and Γ_+ have been calculated by using 3.1.10 and 3.1.10. As we expected, Γ_+ is always positive. We have found that Γ_- is negative in the broad range of the signal and idler frequencies, see the dashed line in Figure 3.3.8(a). Thus, by increasing the pump power P, one can always satisfy the MI condition 3.1.11. The calculated gain together with the threshold pump power $p_{th}(\lambda_p)$ (red dashed curve) are shown in Figs. 3.3.8(b). The darker colors indicate the larger value of gain.

In addition, To demonstrate the MI development, we investigate the propagation of pump and signal waves. For $P = 800W$, the maximum gain is achieved for $\lambda_s = 1.65\mu m$ ($\lambda_i = 1.75\mu m$), see Figure 3.3.9, and the characteristic MI length is $L_{MI} = 1/g \sim 0.03mm$. By assuming the excitation with picosecond pulses, $T_0 = 1ps$, we estimate the dispersion length, $L_D = T_0^2/|\beta_2| \sim 100mm$, and the walkoff length between the signal and idler, $L_w = T0/|1/v_{gs} - 1/v_{gi}| \sim 1mm$, $v_{gs,gi} = 1/\partial_\omega \beta(\omega_{s,i})$ to be much longer than the MI length. This justifies our CW based approach to analyze MI, Equations. 3.1.1–3.1.3. Also, we simulate the MI development along the waveguide length for the cases of $\delta\beta > 0 (\lambda_p = 1.6\mu m)$ and $\delta\beta < 0 (\lambda_p = 1.7\mu m)$. The results were obtained by numerically simulating Equation 2.3.12 for the case of three waves. During evolution, the energy from the pump is almost entirely transferred to the signal and idler, and then back to the pump again.

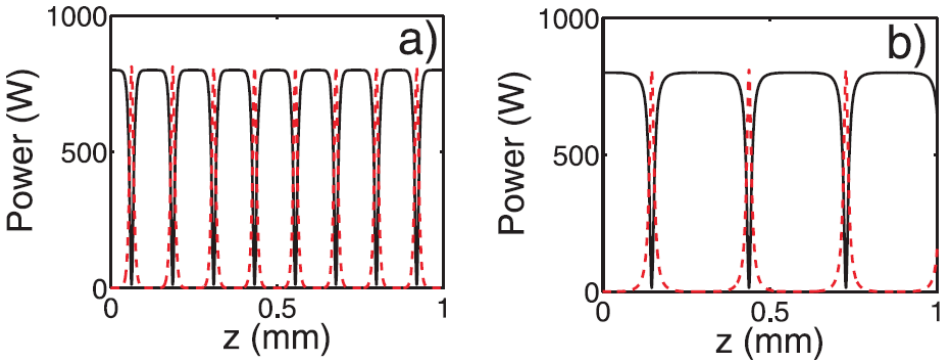

Figure 3.3.10: Dynamics of the pump and signal waves for $\delta\beta > 0$ (a) and $\delta\beta < 0$ (b). Initial power: $p_p = 800W, p_s = 0.8mW, p_i = 0, \lambda_p = 1.6\mu m, \lambda_s = 1.55\mu m$ (a), $\lambda_p = 1.7\mu m, \lambda_s = 1.65\mu m$ (b). Solid and dashed curve correspond to pump and signal, respectively.

The whole process repeats periodically with propagation distance. The pump, signal and idler periodically exchange power (see Figure 3.3.10).

Such recurrence is typical for MI processes in optical fibres[1]. It is known that the pump energy is transferred to the sidebands and even their higher order harmonics[127], surprisingly, after some distance, the energy is back to pump. Studies of possible modifications of the recurrence process due to the dispersion of nonlinearity in subwavelength structures is an interesting topic of future work.

.

3.3.4 Modulation instability for silicon-on-insulator slot waveguide with polymer cladding

To reduce the impacts of TPA and free carrier in silicon waveguide, another approach to implement our theory is that we could use slot waveguide, in which higher amplitude is concentrated on the low-refractive-index region. The slot is filled with nonlinear material, for which the TPA is negligible. In this section, we consider a SOI dielectric slot waveguide with the nonlinear polymer cladding[128]. The guided slot mode is shown in Figure 3.3.11(a). As we investigated in single SOI waveguide before, localization of the fundamental slot mode is also sensitive to wavelength, and therefore the geometrical dispersion of nonlinearity is expected to be significant. The plot of GVD is shown in Fig.

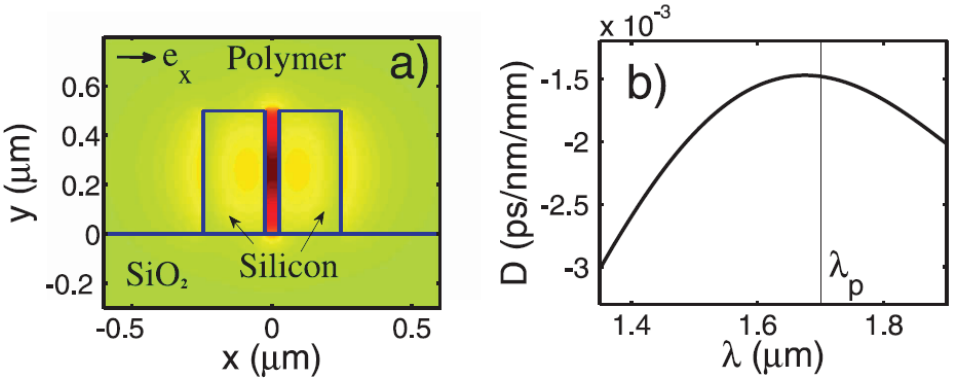

Figure 3.3.11: Fundamental mode of the silicon-polymer slot waveguide: (a) profile of the dominant electric field component (e_x) at $\lambda_p = 1.7\mu m$ for $500nm \times 220nm$ silicon waveguides, wall-to-wall separation $50nm$, silica glass substrate and nonlinear polymer cladding. Geometry is indicated by solid lines; (b) calculated GVD.

3.3.11(b) and it is normal for any wavelength. Hence, Figure 3.3.12(a) shows that $\delta\beta < 0$ within the range of signal and idler wavelengths. It is clear to see that, without the dispersion of nonlinearity, no MI is expected for any pump wavelength.

However, Γ_- has been found negative, see Figure 3.3.12(a). Therefore, the MI condition 3.1.11 is satisfied for $P > P_{th}$, see Figure 3.3.12(b). The ratio of the characteristic lengths (see AlGaAs discussion) has also been found favorable for MI observation over typical sub-millimeter propagation distances, where walk-off due to GVD is negligible for picosecond pulses. Thus, while the frequency conversion in the optical processing experiment with a similar slot waveguide[68] has relied on the two frequency pumping (classical four wave mixing setup), our MI mechanism allows to obtain the necessary gain only with the single pump wave. Note also that TPA and free carrier generation in AlGaAs are negligible for $\lambda \geq 1.5\mu m$. However, they are significant in silicon, but reduced in the slot geometry with the polymer cladding as the most energy of light is focused on the slot[128].

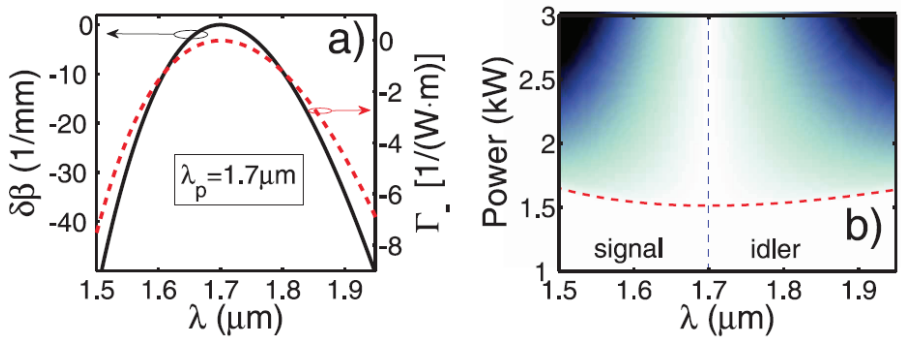

Figure 3.3.12: (a):The plot of $\delta\beta$ and Γ_{-}at $\lambda_p = 2\pi c/\omega_p = 1.7\mu m$ as functions of the signal/idler wavelengths for the slot waveguide shown in Figure 3.3.11(a); (b): gain as function of pump power and signal and idler wavelengths. Again, darker colours correspond to larger values of gain. $n_{2,polymer} = 16.9 \times 10^{-18} m^2/W, n_{2,silicon} = 4 \times 10^{-18} m^2/W$, $D = -0.0015 ps/nm/mm$;

3.3.5 Modulation instability for slot waveguide with silicon layers surrounding a chalcogenide glass layer

As our next example, chalcogenide glass slot waveguide is considered. Our major consideration for using chalcogenide glass is that it has highly nonlinearity with reduced TPA coefficient β_{TPA} compared to silicon[88].

Due to the discontinuity of electric field of quasi-TM mode at the interfaces of the slot and the silicon layers, the guided mode is confined in the slot layer with lower refractive index. The geometry of slot waveguide and dispersion curve are demonstrated in Figure 3.3.13. The large variation of the area of the slot mode with wavelength is expected here. Therefore, the dispersion of nonlinearity is able to induce MI under required threshold power. The plot of GVD is shown in Figure 3.3.13. It is normal for $\lambda > 1.68\mu m$. Numerical calculation shows that the values of Γ_{-} are negative in the range of signal and idler wavelength, see Figure 3.3.14 (b), for $\lambda_p = 1.7\mu m$. Consequently, the MI gain is observed numerically for $p > p_{th}$. Note that, Figure 3.3.15 also shows that the threshold power ($800W$) is lower than the one ($1500W$) in Figure 3.3.12. In practice, lower threshold power is required in order to reduce nonlinear loss, such as TPA and free carrier .

The characteristic lengths, such as MI length $L_{MI} = 1/g$, has been calculated, which is much shorter than the dispersion length $L_D = T_0^2/|\beta_2|$. Also,

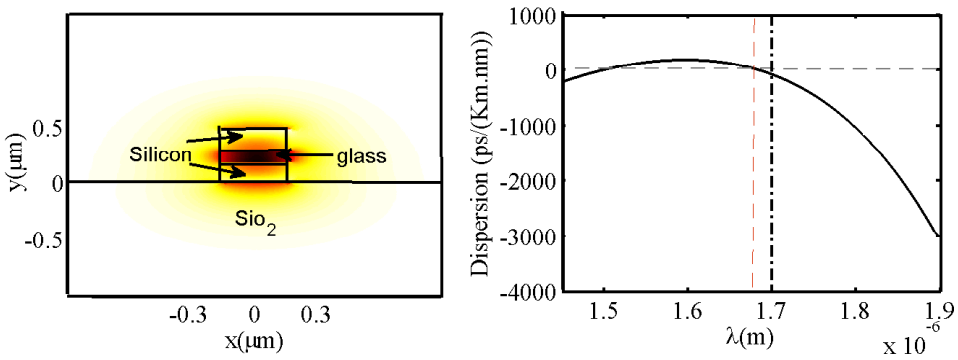

Figure 3.3.13: Slot waveguide with silicon layers surrounding a highly nonlinear slot layer (chalcogenide glass). Fundamental mode of slot waveguide: in the left, profile of the dominant electric field component at $\lambda_p = 1.7\mu m$ for $280nm \times 180nm$ silicon waveguides, wall-to-wall separation $115nm$, silica glass substrate and air cladding. Geometry is indicated by solid lines; in the right, calculated GVD. Black dash-dot line indicates the pump wavelength $\lambda_p = 1.7\mu m$. Red dashed line represents Z-GVD wavelength.

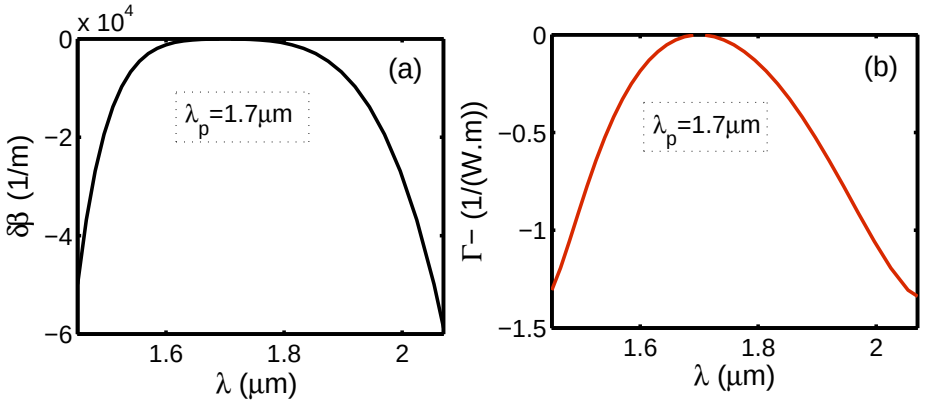

Figure 3.3.14: Plot of $\delta\beta$ and Γ_as function of signal and idler wavelengths for the slot waveguide . Geometry is same as Figure 3.3.13. $D = -0.0003ps/nm/mm$ $n_{2,glass} = 3 \times 10^{-18}m^2/W$, $n_{2,silicon} = 4 \times 10^{-18}m^2/W$

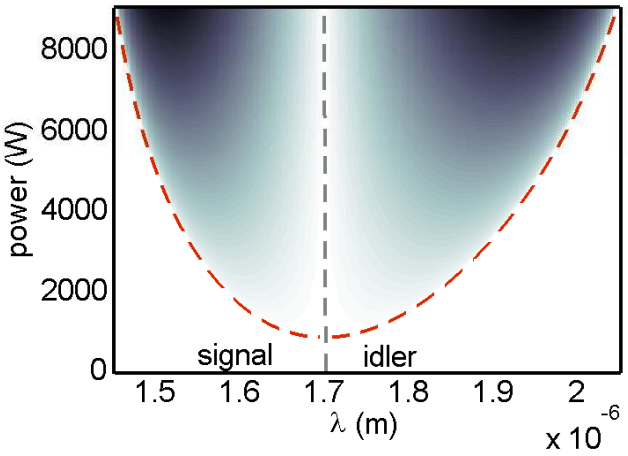

Figure 3.3.15: Plot of gain as function of pump power and signal/idler wavelengths. Dashed lines show the threshold power $p_{th} = \delta\beta/(4\Gamma_{-})$; Geometry is same as Figure 3.3.13. In the shaded area, darker colours indicate the larger values of gain.

the walk-off between signal and idler is negligible for picosecond pulse.

3.4 Minimal model describing modulation instability induced by dispersion of nonlinearity

Apart from continuing to seek more suitable geometry and material to reduce the threshold power and nonlinear loss, we also need to investigate the MI condition more deeply. All of these calculations of γ_{nklm} based on our theory are quite complicated because of the complex overlap integrals. Therefore, condition of existence of MI gain is not straightforward. Indeed, all the information needed to analyze MI condition in Equation 3.1.11 is hidden inside the overlap integrals. In order to find the better way to understand new MI condition induced by the dispersion of nonlinearity, we introduce a generalized NLS equation where all the dispersion coefficients include nonlinear contributions:

$$i\partial_z A = -\sum_{n=0}^{N}(\beta_n + \gamma_n|A|^2)\partial_t^n A. \tag{3.4.1}$$

where A is slowly varying amplitude. Monochromatic solution of this equa-

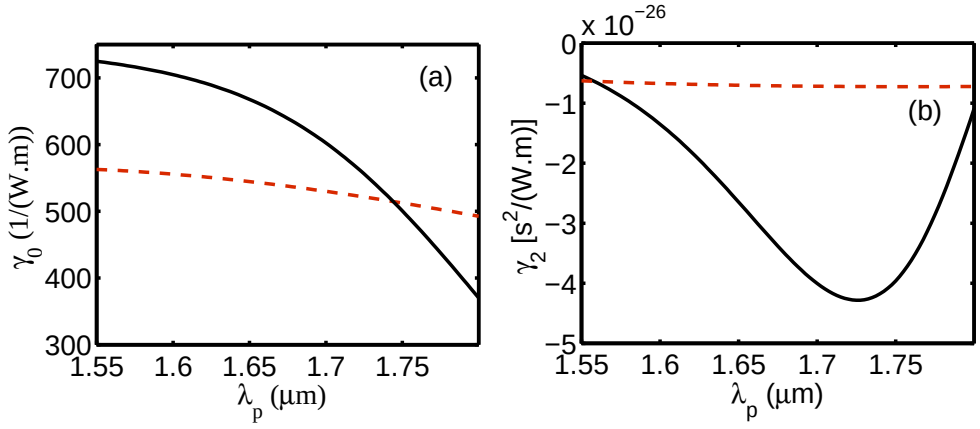

Figure 3.4.1: Plot of nonlinear parameters (a)$\gamma_0$and (b) γ_2 for different geometries as in Fig. 3.3.7 (solid line) and Fig.3.3.11 (dashed line).

tion is given by $A = ae^{i\kappa z - i\delta t}$, where $\kappa = \sum_n (\beta_n + \gamma_n |a|^2)\delta^n/n!$ and $\delta = \omega - \omega_p$. The linear propagation constant is

$$\beta = \sum_n \beta_n \delta^n / n!,$$

and, the frequency dependence of the nonlinear waveguide parameter γ is given by:

$$\gamma = \sum_n \gamma_n \delta^n / n!.$$

By the appropriate choice of the phase shift and of the reference frame velocity, we can fix $\beta_0 = \beta_1 = 0$. We simply take the minimal model including dispersion of nonlinearity resulting in MI when $\delta\beta < 0$:

$$i\partial_z A = -\gamma_1 |A|^2 \partial_t A + \frac{1}{2}(\beta_2 + \gamma_2 |A|^2)\partial_t^2 A - \gamma_0 |A|^2 A. \tag{3.4.2}$$

As we demonstrated in chapter two before, we expand A as the sum for the pump, signal and idler fields:

$$A = A_p(z)e^{i\kappa_p z} + A_s(z)e^{i\kappa_s z - i\Omega t} + A_i(z)e^{i\kappa_i z + i\Omega t} \tag{3.4.3}$$

where $A_p(z), A_s(z), A_i(z)$ are the slowly varying amplitudes with distance corresponding to the pump, signal and idler waves, $\kappa_p, \kappa_s, \kappa_i$ represent the total propagation constant (linear part and nonlinear part), and Ω is the frequency

detuning from pump wavelength. Substituting 3.4.3 into 3.4.2, we have following equations in the form of:

$$i\partial_z A_p - \kappa_p A_p = -\gamma_0 |A_p|^2 A_p,$$

$$i\partial_z A_s - \kappa_s A_s = -\frac{\beta_2}{2}\Omega^2 A_s - (2\gamma_0 + \gamma_1\Omega + \frac{1}{2}\gamma_2\Omega^2)|A_p|^2 A_s - \gamma_0 A_p^2 A_i^* e^{i\delta\kappa z},$$

$$i\partial_z A_i - \kappa_i A_i = -\frac{\beta_2}{2}\Omega^2 A_i - (2\gamma_0 - \gamma_1\Omega + \frac{1}{2}\gamma_2\Omega^2)|A_p|^2 A_i - \gamma_0 A_p^2 A_s^* e^{i\delta\kappa z}.$$

One can readily find that $\gamma_{4s} = \gamma_{4i} = \gamma_0 = \gamma_p$ (Note that in the modal expansion $\gamma_{4s} \neq \gamma_{4i} \neq \gamma_0$), $\gamma_{sp} = \gamma_0 + \frac{1}{2}\gamma_1\Omega + \frac{1}{4}\gamma_2\Omega^2$,$\gamma_{ip} = \gamma_0 - \frac{1}{2}\gamma\Omega + \frac{1}{4}\gamma_2\Omega^2$. Thus MI condition for $\delta\beta < 0$ transforms to : $\Gamma_- = \gamma_2\Omega^2 < 0$. For relatively small detuning Ω, we have $\gamma_n = \partial_\omega^n \gamma$.

Using equation 2.3.15, $\gamma_p(\omega_p)$ are evaluated as function of wavelength for AlGaAs waveguide (see Figure 3.3.7) and slot waveguide (see Figure 3.3.11), see Figure 3.4.1 (a). We also plot the second derivative as a function of wavelength for the waveguides considered above in Figure 3.4.1 (b). These plots show that $\partial_\omega^2 \gamma < 0$ and therefore comfirm our prediction about MI resulting from the calculation of the several overlap integrals. This simple differentiation of γ gives us straightforward approach to estimate where such behavior can be expected.

3.5 Summary

In this chapter, by using our model derived in chapter two, we proved that the growth rate of MI can exist even in the range of normal GVD due to dispersion of nonlinearity in subwavelength AlGaAs and silicon waveguides. We calculated the pump power thresholds required for this type of MI and we found that the gain exists under acceptable threshold powers. To reduce the threshold power to levels more favorable for applications, further understanding of the relevant physics and design work are necessary. We presented a simple generalization of the NLS equation accounting for the MI resulting from the dispersion of nonlinearity. By computing MI condition based on this equa-

tion, we presented that much simpler differentiation of γ can give us the same prediction about existence of MI induced by the dispersion of nonlinearity.

Chapter 4

Modulation instability and spectral variation induced by nonlinear dispersion in picsecond regime

As discussed in chapter 3, tight confinement of light (typical waveguide transverse dimensions of the order of hundreds of nanometers) and a strong variation of modes with wavelength for CW in such subwavelength waveguides with high refractive index contrast induce substantial dispersion of nonlinear response [126], which has a strong influence on FWM or soliton[130, 131].

Pulse propagation equations which are able to accurately describe evolution of ultra-short pulses in nonlinear media have been explored for many years. The well-known and generally accepted nonlinear Schrödinger model [1] in conventional waveguides and fibers can qualitatively and successfully describe evolution of the guided mode envelope with propagation distance although it has a very simple form consisting of the group velocity dispersion of the mode (responsible for pulse spreading in time) and nonlinear interaction (resulting from the intensity-dependent refractive index). It is the interplay between these linear and nonlinear effects that creates many interesting phenomena in optical waveguides and fibers [1].

One of the most important assumptions on which the NLS equation is based is that the z-component of the electric field is very small with respect

to its transverse components (weak guidance regime)[1, 5]. However, this is only true for waveguides with a relatively low refractive index contrast between the core and the cladding, and with core sizes being much larger than the wavelength of light. For subwavelength semiconductor waveguides, the longitudinal electric field component of the mode should be included into the model. Therefore, development of adequate models to describe light propagation in subwavelength waveguides has become the subject of active research in the recent years [90, 88, 110, 86, 87, 132, 133, 134].

Light confined within several handreds nanometers area strongly enhances the nonlinearity in subwavelength waveguides. On the other hand, one of the distinctive features of these waveguides is a strong variation of the modal profile with the wavelength of light. Since distribution of light intensity across the cross-section of waveguide defines the effectiveness of nonlinear (multiphoton) processes, this variation leads to a considerable dispersion of nonlinearity [133, 134]. By introducing a nonlinear waveguide parameter γ depending on frequency, some novel effects can be explored based on the generalized NLS equation[1]. As we all know, the first-order dispersion of nonlinearity ($\gamma_1 = d\gamma/d\omega$) gives intensity-dependent correction to the group velocity. It is responsible for the self-steepening of pulses. Self-steepening leads to an asymmetry in the SPM-broadened spectra of ultrashort pulses[1]. In subwavelength waveguides, the self-steepening effect can be significantly enhanced due to the geometrical contribution to the dispersion of nonlinearity [88, 87, 111]. More than this, dispersion of nonlinearity resulting from geometrical contribution causes much attention since many novel effects associated with nonlinear dispersion have been found. Recently we derived a set of coupled equations governing pulse propagation by using reciprocity theorem[2] and identified the novel mechanism of MI of a constant-amplitude wave, mediated by the dispersion of nonlinearity in subwavelength waveguides[126]. We also introduced a simple phenomenological model describing this effect, which is based on the generalized version of the NLS equation where the second-order dispersion of nonlinearity term is included ($\gamma_2 = d^2\gamma/d\omega^2$). Similar models have been considered recently in the context of ultrashort pulse dynamics in fibers [135, 131], beam propagation in nonlinear photonic crystals[130], pulse dynamics in nonlinear metamaterials [136], and dynamics of Bose–Einstein condensate of dipo-

lar atoms in a periodic potential [137].

It must be emphasized, that for the Kerr-type nonlinear response of a medium (the most common in optics), the nonlinear process involves four photons at different frequencies (four wave mixing process). Therefore, the nonlinear parameter γ should rely on four frequencies of all the interacting waves, rather than single frequency dependence $\gamma(\omega)$ as in the above NLS models.[90, 86, 87, 126]. Conveniently, to obtain the wave equation for the slowly varying amplitude, we can work in the frequency domain by treating p_{NL} as a small perturbation. However, as we presented in chapter 3, the resulting model that describes evolution of individual harmonics with the propagation distance, the harmonic propagation (HP) model, contains a network of nonlocal nonlinear interactions[87, 126]. Also, this approach gives us little intuition on why and where such behavior can be expected.

In this chapter, we demonstrate that the HP model ,which is derived from Maxwell equations following the standard perturbation expansion procedure[90, 88, 86], can be reduced to the generalized NLS equation with higher order dispersion terms and nonlinear dispersion terms[138] (more details see below). The only assumption which allows this reduction is the factorization of the four-frequency dependence of nonlinear coefficients in HP model. Having analyzed different semiconductor subwavelength waveguide geometries, we found that this factorization approximates well the actual four-frequency dependencies in a wide range of wavelengths.

4.1 Factorization approximation

Below, we introduce the factorization of nonlinear coefficients and compare with the actual full coefficients Γ. In chapter 2, we derived the equation 2.3.18 which can fully describe pulse propagation with the dispersion of nonlinearity in sub-wavelength waveguides. The full coefficient Γ has the form:

$$\Gamma_{nklm} = \frac{\varepsilon_0}{\sqrt{I_n I_k I_l I_m}} \times \int_A \chi_{nklm} \varsigma(\hat{r}) dA,$$

$$\varsigma_{nklm} = \rho(\hat{r})[(e_n^* \cdot e_m)(e_l^* \cdot e_k) + (e_n^* \cdot e_k)(e_l^* \cdot e_m) + (e_n^* \cdot e_l^*)(e_k \cdot e_m)] \quad (4.1.1)$$

$$+3(1-\rho(\hat{r})) \sum_{i=x,y,z} e_{ni}^* e_{ki} e_{li}^* e_{mi}. \quad (4.1.2)$$

The geometrical dispersion of nonlinearity is accounted for by the coefficients ς_{nklm} in equation 4.1.1. Notably, definition of these coefficients involves overlap integrals with modal profiles at different frequencies. We note that ς_{nklm} are invariant under all permutations of indices[3] that preserve the condition $n-k+l-m=0$: $\varsigma_{nklm} = \varsigma_{lknm} = \varsigma_{nmlk} = \varsigma_{mlkn} = \varsigma_{knml} = \varsigma_{mnkl}$. However, even with the account of the above symmetry, description of a broadband signal evolution within the HP model in equation 2.3.18 remains to be a challenging computational task due to the large number of nonlinear coefficients to be computed. Considering the above permutation symmetry resulting from the Si's symmetry, a significant reduction can be made by assuming factorization of nonlinear coefficients:

$$\Gamma_{nklm} = g_n g_k g_l g_m, g_n = \Gamma_{nnnn}^{1/4}. \quad (4.1.3)$$

To prove our approximation, we test it by the direct comparison with the original coefficients obtained from equation 4.1.1. The relative error is defined as:

$$\Delta = |\Gamma_{nklm} - g_n g_k g_l g_m| / \Gamma_n$$

For $300nm \times 500nm$ AlGaAs waveguide (the AlGaAs waveguide geometry shown in Figure 4.1.1), Figure 4.1.2 shows the relative error Δ plotted in the plane of parameters $\delta_{k,l} = (\omega_{k,l} - \omega_n)/\omega_n$ for the fixed $\omega_n \approx 1.13 \times 10^{15} rad/s$ ($\lambda_n = 2\pi c/\omega_n = 1.665\mu m$). It should be noted that the fourth frequency ω_m is determined by the resonance condition in equation 2.3.18. The discrepancy between the factorized coefficient Γ (equation 4.1.3) and the full coefficient Γ (equation 4.1.1), remains to be small,$\Delta < 10^{-1}$, within a large window of frequency detunings ($\delta_k = 0.25$ corresponds to $\delta\lambda \approx 0.5\mu m$). We have obtained similar results for other fixed values of ω_n. For the silicon waveguide (geometry shown in Figure 4.5.1), we repeated the above calculations and comparison and the same conclusion has been obtained. All of the tests that we did so far

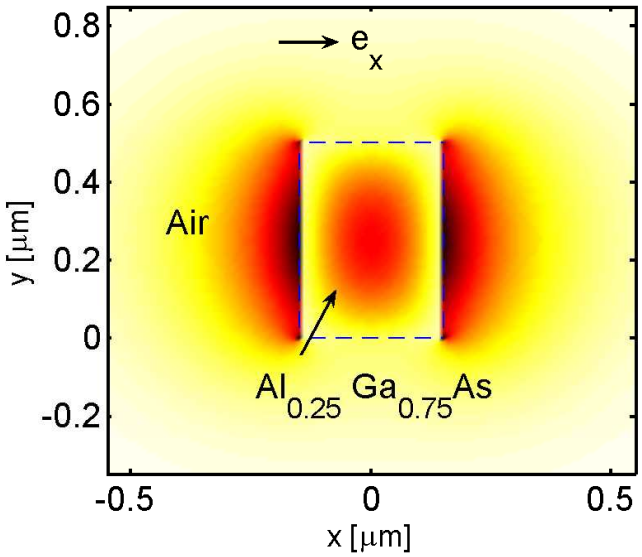

Figure 4.1.1: Geometry and profile of the quasi-TE guided mode in subwavelength AlGaAs waveguide with cross-section $300nm \times 500nm$ suspended in air for $\lambda_0 = 1.665\mu m$.

manifest that our approximation (factorization of nonlinear coefficients) is reasonable and can give us consistent results. Note that certain one-dimensional subsets of coefficients with $\delta_k = \delta_l, \delta_k = 0, \delta_l = 0$ enter the condition of MI of the constant amplitude pump at the frequency ω_n, as will be discussed in the next section. Further comparison between the corresponding factorized and full coefficients Γ is illustrated in Figure 4.1.4.

4.2 Pulse propagation equation

Based on our factorization of nonlinear coefficients, the equation 2.3.18 can be reduced to a single generalized NLS. Firstly, replacing coefficients Γ_{nklm} with their factorized analogs and changing to variables :

$$A_n = (g_0/g_n)\Psi_n, \tag{4.2.1}$$

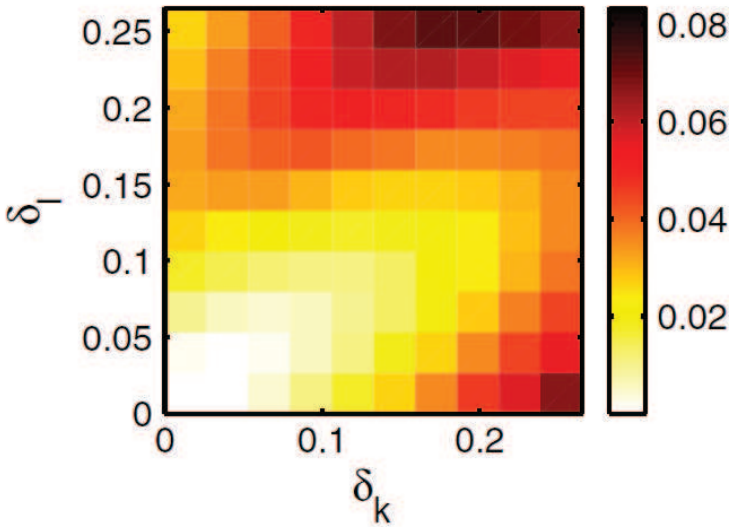

Figure 4.1.2: Relative error Δ for the AlGaAs waveguide with cross-section $300nm \times 500nm$ as in Figure 4.4.1 and the fixed frequency $\omega_n = 2\pi c/\lambda_n, \lambda_n = 1.665\mu m$, see text for details.

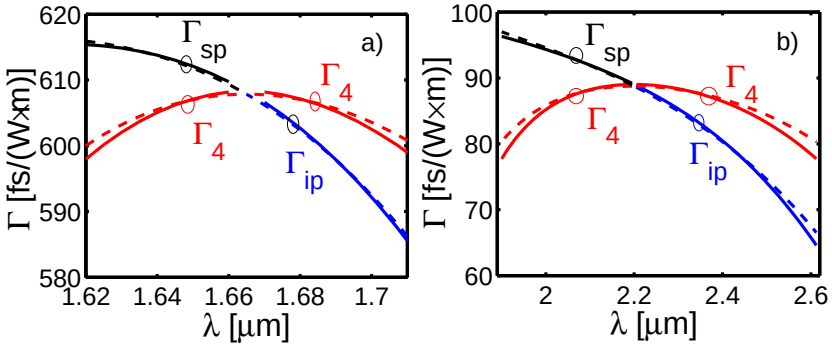

Figure 4.1.3: The plots of nonlinear coefficients Γ entering the necessary condition of MI [see equation 4.3.5] calculated for AlGaAs waveguide at $\lambda_p = 1.665\mu m$ (a) and SOI waveguide at $\lambda_p = 2.2\mu m$ (b). Dashed curves show their factorized approximations, see Equation 4.1.3.

where $g_0 = \Gamma_0^{1/4}$corresponds to a reference frequency ω_0, thus the equation 2.3.18 becomes:

$$i\partial_z \Psi_\omega = -\beta_\omega \Psi_\omega - \frac{\tilde{\gamma}_\omega}{2\pi} \int\int \Psi_{\omega_1} \Psi^*_{\omega_2} \Psi_{\omega_3} d\omega_1 d\omega_2, \tag{4.2.2}$$

where the modified nonlinear coefficient is given by:

$$\tilde{\gamma}_\omega = \omega \sqrt{\Gamma_0 \Gamma_\omega}. \tag{4.2.3}$$

It is instructive to note that the equation 4.2.2 possesses two integrals of motion[137]:

$$P = \int \frac{\omega |\Psi_\omega|^2}{\tilde{\gamma}_\omega} d\omega = const.,$$

$$N = \int \frac{|\Psi_\omega|^2}{\tilde{\gamma}_\omega} d\omega = const.$$

They are very useful for monitoring the accuracy of numerically integrating the equation 4.2.2. In particular, in terms of the original harmonic amplitudes A_n, these integrals correspond to the energy and the number of photons, respectively.

By assuming polynomial fits of the linear and nonlinear dispersion coefficients in the equation 4.2.2:

$$\beta(\omega = \omega_0 + \delta) = \sum_{n=0}^{N_D} (1/n!) \beta_n \delta^n$$

$$\tilde{\gamma}(\omega = \omega_0 + \delta) = \sum_{n=0}^{N_G} (1/n!) \tilde{\gamma}_n \delta^n,$$

using the inverse Fourier transform:

$$\psi(z,t) = \frac{1}{\sqrt{2\pi}} \int \Psi_\omega(z) e^{-i(\omega_0+\delta)t} d\delta$$

and transforming into the rotating and moving frame[1] by introducing

$$\psi(z,t) = a(\tau = t - \beta_1 z, z) e^{i\beta_0 z},$$

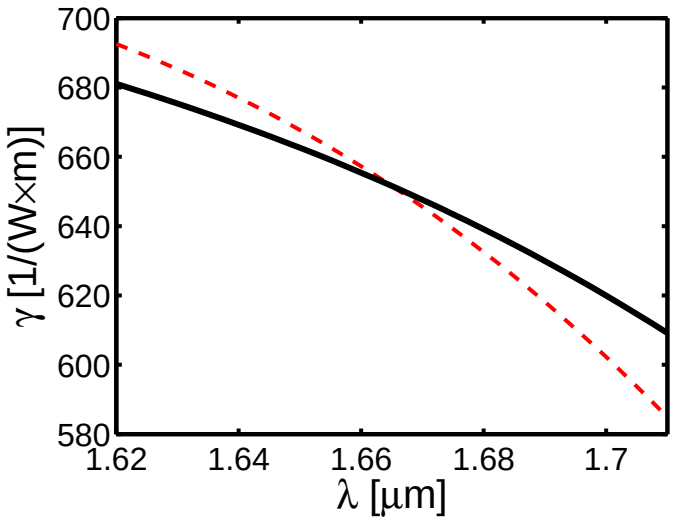

Figure 4.2.1: Modified nonlinear coefficient $\tilde{\gamma}$ for AlGaAs waveguide; see equation 4.2.3. Dashed curve shows the conventional nonlinear coefficient $\gamma = \omega\Gamma_\omega$for the same waveguide.

Eventually, we obtain the following pulse propagation equation:

$$i\partial_z a = -\hat{D}(i\partial_\tau)a - \hat{G}(i\partial_\tau)(|a|^2 a) \tag{4.2.4}$$

$$\hat{D}(i\partial_\tau) = \sum_{n=2}^{N_D} \frac{\beta_n}{n!}(i\partial_\tau)^n \tag{4.2.5}$$

$$\hat{G}(i\partial_\tau) = \sum_{n=0}^{N_G} \frac{\tilde{\gamma}_n}{n!}(i\partial_\tau)^n. \tag{4.2.6}$$

The equation 4.2.4 allows us to describe the pulse dynamics and parametric frequency conversion processes in subwavelength waveguides without computing the overlap integrals. Unlike the method proposed in[87], our approach does not require performing computationally heavy procedure of Taylor expansion of the modal profile frequency dependence, and is not limited by the narrow spectral width (quasi- CW) approximation.

It should be emphasized that the factorization of coefficients Γ_{nklm} in equation 4.1.3 is the only approximation made to derive the above generalized NLS equation 4.2.4. The dispersion of nonlinearity operator $\hat{G}$ in equation 4.2.4

and 4.2.6 is related to the modified nonlinear coefficient $\tilde{\gamma}(\omega)$, which is obviously different from the conventional nonlinear coefficient$\gamma = \omega\Gamma_\omega$[90, 1], see equation 4.2.3. Figure 4.2.1 shows the differences between γ (conventional nonlinear coefficient) and $\tilde{\gamma}$ using equation 4.2.3. If a narrowband signal is considered, the polynomial expansion coefficients $\tilde{\gamma}_n$can be replaced by the standard Taylor coefficients:

$$\tilde{\gamma}_{tn} = d^n\tilde{\gamma}/d\omega^n = d^n(\omega\sqrt{\Gamma_0\Gamma_\omega})/d\omega^n. \tag{4.2.7}$$

One can relate these coefficients to the corresponding Taylor expansion coefficients of the functionγ. γ_{tn} is given by:

$$\gamma_{tn} = d^n\gamma/d\omega^n = d^n(\omega\Gamma_\omega)/d\omega^n \tag{4.2.8}$$

For the first three coefficients we obtain:

$$\tilde{\gamma}_0 = \gamma_0 \tag{4.2.9}$$

$$\tilde{\gamma}_1 = \frac{1}{2}(\frac{\gamma_0}{\omega_0} + \gamma_1) \tag{4.2.10}$$

$$\tilde{\gamma}_2 = \frac{\gamma_2}{2} - \frac{(\gamma_1 - \gamma_0/\omega_0)^2}{4\gamma_0} \tag{4.2.11}$$

Figure 4.2.2 demonstrates that the values of $\tilde{\gamma}_1$ and $\tilde{\gamma}_2$ from our approach are smaller than values of $\gamma_1$and γ_2, respectively, while pump wavelength moves towards large wavelength, which implies that one should obtain higher gain (see equation 4.3.10) under the same initial power p if a gerneralized NLS equation[1] is employed.

We should note that, when geometrical dispersion of nonlinearity is absent, which means $\tilde{\gamma}_{i>1} = 0$, the first-order dispersion coefficient $\tilde{\gamma}_1$ is reduced to the standard self-steepening term [1]: $\tilde{\gamma}_1 = \gamma_0/\omega_0$.

To analyze the role of dispersion of nonlinearity in ultrashort pulse dynamics and parametric frequency conversion, the pulse propagation equation 4.2.4 is investigated below. In our modeling, by using equation 4.1.1, we computed coefficients Γ_ω (see Figure 4.1.3) from modal profiles which, together

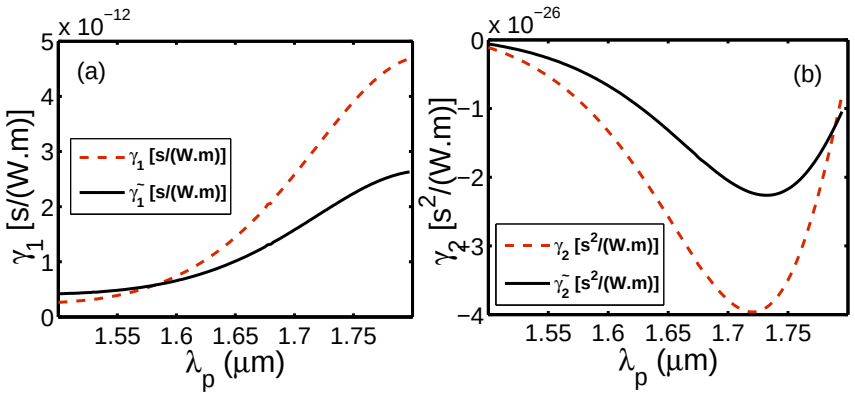

Figure 4.2.2: Modified Taylor expansion coefficients $\tilde{\gamma}_1$ and $\tilde{\gamma}_2$ as function of pump wavelength for AlGaAs waveguide; see equation 4.2.7. Dashed curve shows the Taylor expansion coefficients γ_1 and γ_2 for the same waveguide; see equation 4.2.8.

with the corresponding propagation constants $\beta(\omega)$, were obtained with the help of a commercially available Maxwell solver package. Equation 4.1.1 was then numerically integrated by the standard split-step procedure [1], where the nonlinear step was computed in frequency domain by the fourth-order Runge–Kutta method. Finally, the output field was converted to the modal amplitudes A by applying the scaling in frequency domain, see equation 4.2.1.

4.3 Modulation instability for pulse wave induced by dispersion of nonlinearity

MI is a well known and widely studied in fibers and waveguides because of its potential applications. As discussed in chapter 2, For focusing Kerr nonlinearity[1], the MI gain has the form: $g = \sqrt{\gamma p \delta\beta - \frac{1}{4}\delta\beta^2}$, where γ is the nonlinear parameter, and p is the pump power, and $\delta\beta$ is linear phase mismatch. One can see that the gain exists within $0 < \delta\beta < 4\gamma p$. $\delta\beta$ can be rewritten as: $\delta\beta = -2\sum_{m=2,4...}^{\infty} \frac{\beta_m(\omega_p)}{m!}\Omega^m$. Note that only the even order dispersion terms have influence on the MI condition. In particular, if β_2 is dominant, then MI gain requires that GVD is anomalous. It should be noted that the higher even order dispersion terms can lead to MI gain, which occurs in the large frequency offset, when we operate the wavelength within the normal

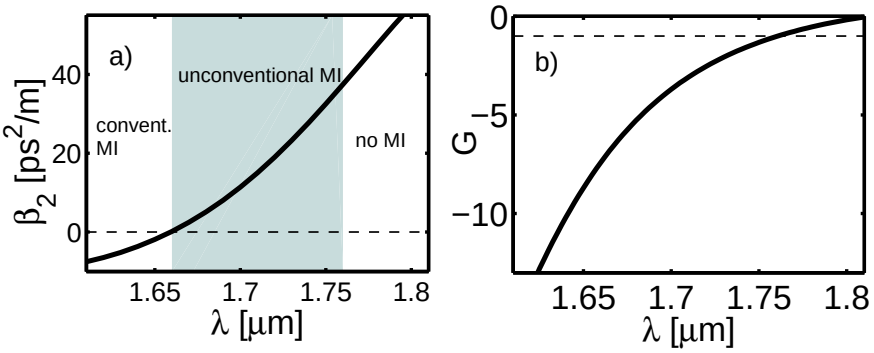

Figure 4.2.3: (a) group velocity dispersion, conventional MI is possible in the range of anomalous GVD, $\beta_2 < 0$. Shaded area indicates the region of unconventional MI due to the dispersion of nonlinearity. (b) Condition for $\gamma_- < 0$, see equation 4.3.12.

GVD regime[104]. In this case, although β_2 is positive, the higher even order dispersion terms makes $\delta\beta > 0$. On the other hand, MI research was extended to a NLS equation with self-steepening term and Raman nonlinearity. They both have impact on MI gain and condition[142]. Here, we only consider the parametric processes, in which the total energy of the interacting photons is conserved. Therefore, any non-parametric effects, such as TPA, Raman effect have been disregarded in what follows.

In this section, based on propagation equations 2.3.18 and 4.2.4, we exploit the MI in two different ways. The onset of MI can be analyzed and numerically modeled by reduced HP model 2.3.18, which includes only three interacting harmonics[126]. However, their mixing generally leads to generation of multiple higher-order harmonics, see Figure 4.4.1 (a). To model such process, it is more convenient to use equation 4.2.4. Moreover, it allows one to identify specific features of MI process when dealing with pulsed excitation. Below, we compare the two models by considering three interacting harmonics, and then proceed with numerical analysis of MI evolution with pulses by using the equation 4.2.4.

By assuming the very weak signal and idler waves and a strong pump pulse, reduced equation 2.3.18 can be written as :

$$i\partial_z A_p = -\beta_p A_p - \omega_p \Gamma_p |A_p|^2 A_p \tag{4.3.1}$$

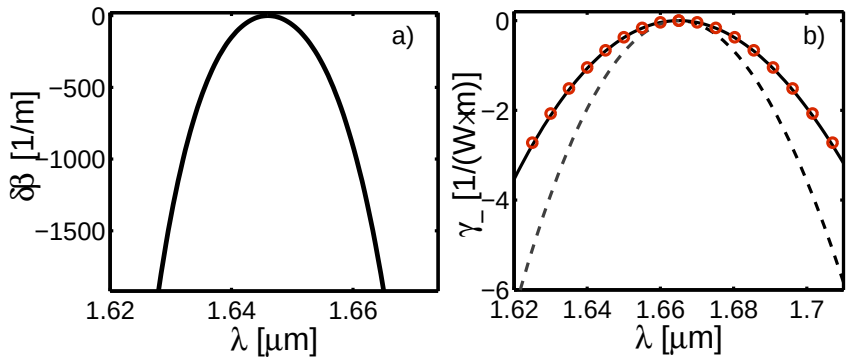

Figure 4.3.1: (a) $\delta\beta$ at pump wavelength $\lambda_p = 1.665\mu m$ as functions of signal and idler wavelengths. (b) calculated γ_- for $\lambda_p = 1.665\mu m$ from equation 4.3.11 by using Taylor expansion coefficients of $\tilde{\gamma}(\omega)$, solid curve, and $\gamma(\omega)$, dashed curve. Red circles correspond to γ_- calculated from 4.3.6.

$$i\partial_z A_s = -\beta_s A_s - 2\omega_s \Gamma_{sp}|A_p|^2 A_s - \omega_s \Gamma_4 A_p^2 A_i^* \tag{4.3.2}$$

$$i\partial_z A_i = -\beta_i A_i - 2\omega_i \Gamma_{ip}|A_p|^2 A_i - \omega_s \Gamma_4 A_p^2 A_s^* \tag{4.3.3}$$

where $\beta_{p,s,i} = \beta(\omega_{p,s,i})$. For convenience, we take $\Gamma_p = \Gamma_{pppp}, \Gamma_{sp} = \Gamma_{spps}\Gamma_{ip} = \Gamma_{ippi}\Gamma_4 = \Gamma_{spip} = \Gamma_{ipsp}$. Assuming $A_s, A_i \sim e^{qz}$, parametric amplification occurs when $g = Re(q) > 0$. From equations 4.3.1-4.3.3, it is straightforward to derive the corresponding condition of existence of MI and gain [126]:

$$4\gamma_-|A_p|^2 < \delta\beta < 4\gamma_+|A_p|^2 \tag{4.3.4}$$

$$g = \frac{1}{2} Re(\sqrt{(4\gamma_+|A_p|^2 - \delta\beta)(\delta\beta - 4\gamma_-|A_p|^2)}) \tag{4.3.5}$$

$$\gamma_\pm = (\omega_s\Gamma_{sp} + \omega_i\Gamma_{ip} - \omega_p\Gamma_p \pm \sqrt{\omega_s\omega_i\Gamma_4^2})/2 \tag{4.3.6}$$

In the absence of dispersion of nonlinearity, i.e., assuming all coefficients Γ in equation 4.3.6 to be equal, it is easy to see that $\gamma_- > 0$, and therefore MI is only possible when $\delta\beta > 0$, which is the well-known textbook condition [1]. In particular, if $\beta(\omega)$ can be approximated by a parabola in a vicinity of ω_p [i.e., $\beta_{i>2} = 0$ in equation 4.2.5, as we discussed above, the conventional

MI condition can be recovered: $\beta_2 = \partial_\omega^2 \beta(\omega_p) < 0$, which corresponds to anomalous GVD, see Figure 4.2.3(a).

It should be pointed out that no gain is possible if the pump power P is below the threshold pump power:

$$P > P_{th} = |\delta\beta|/(4|\gamma_-|). \tag{4.3.7}$$

Recently, we identified a novel mechanism supporting MI when $\delta\beta < 0$ provided $\gamma_- < 0$. Dispersion of nonlinearity is obviously responsible for this[126]. Note that $\Gamma(\omega)$ should be able to make γ_-negative, which generally implies $\tilde{\gamma}_2 = \partial_\omega^2 \tilde{\gamma} \neq 0$ [126], see equation 4.2.3.

Different coefficients Γ entering the condition in equation 4.3.4 are plotted for the AlGaAs and silicon waveguides in Figure 4.1.3(a) and (b), respectively. Apparently, in both examples, factorization approximation works well in a wide range of signal/idler wavelengths, and therefore one can benefit from using the more convenient for analysis pulse propagation equation 4.2.4.

In the presence of only first-order and second-order dispersions of nonlinearity in the equation 4.2.4, Expanding a as the sum for the pump, signal and idler waves: $a = a_p(z)e^{i\kappa_p z} + a_s(z)e^{i\kappa_s z - i\delta t} + a_i(z)e^{i\kappa_i z + i\delta t}$, where a_p, a_s, a_i stand for pump, signal and idler waves and δ is frequency shift, and substituting it into equation 4.2.4, After several calculations, for strong pump and small signal and idler waves, we obtain the following equations:

$$i\frac{\partial \mathrm{a}_s}{\partial z} = (-\tilde{\gamma}_0 - \tilde{\gamma}_1\delta - \frac{\tilde{\gamma}_2}{2}\delta^2)a_p^2 a_i^* e^{i\delta\kappa z} \tag{4.3.8}$$

$$i\frac{\partial a_i}{\partial z} = (-\tilde{\gamma}_0 + \tilde{\gamma}_1\delta - \frac{\tilde{\gamma}_2}{2}\delta^2)a_p^2 a_i^* e^{i\delta\kappa z} \tag{4.3.9}$$

The growth rate of MI is given by:

$$g = Re\sqrt{-\frac{1}{4}\delta k^2 + \delta k(\tilde{\gamma}_0 P + \tilde{\gamma}_2 P\delta^2) - \tilde{\gamma}_0\tilde{\gamma}_2\delta^2 P^2 - \frac{3}{4}\tilde{\gamma}_2^2\delta^4 P^2 - \tilde{\gamma}_1^2\delta^2 P^2} \tag{4.3.10}$$

where P is the pump power and $P = |A_p|^2$, and δk is linear mismatch. By ignoring all of the nonlinear dispersion terms, the conventional gain expression[1] can be restored.

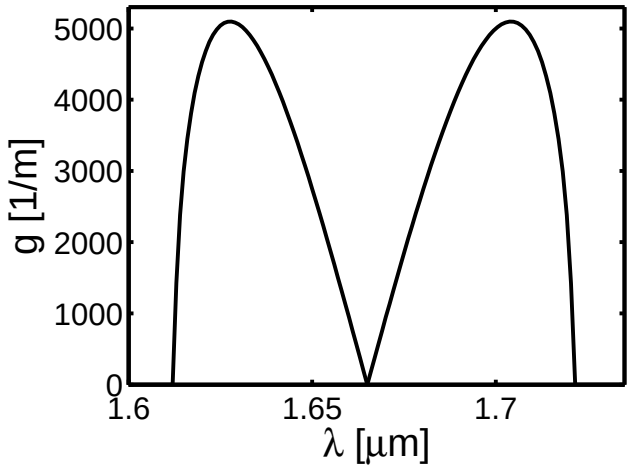

Figure 4.3.2: Gain based on equation 4.3.10 as functions of signal and idler wavelengths for the pump wavelengh $\lambda_p = 1.665\mu m$ and pump power $|A_p|^2 = 150W$.

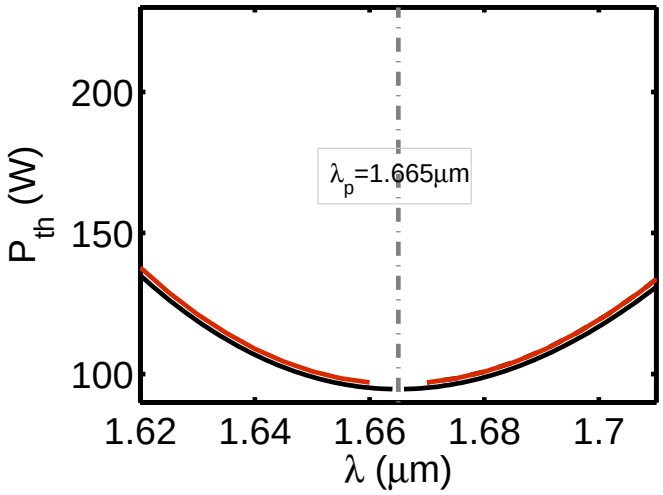

Figure 4.3.3: Threshold power P_{th} as function of signal and idler wavelength. The red curve shows computed P_{th} using equation 4.3.6and 4.3.7. The P_{th} computed from equation 4.3.11 and 4.3.7 for the same pump wavelength $1.665\mu m$.

To gain the direct insight, instead of calculating the five complex nonlinear coefficients, in chapter 2, by employing the minimal model 3.4.2, the MI condition has the simple form: $\Gamma_- = \frac{1}{2}\gamma_2\Omega^2 < 0$. Therefore, the condition transforms to: $\gamma_2 < 0$. In the present work, it is obvious that $\gamma_-(\delta = \omega_p - \omega_s)$ is given by:

$$\gamma_- = \frac{\tilde{\gamma}_0 + \tilde{\gamma}_2\delta^2 - \sqrt{(\tilde{\gamma}_0 + \frac{\tilde{\gamma}_2\delta^2}{2})^2 - \tilde{\gamma}_1^2\delta^2}}{2} \tag{4.3.11}$$

From this expression, one can see that the MI gain is crucially determined by the sign of $\tilde{\gamma}_2$, and $\tilde{\gamma}_1$ doesn't affect the gain condition. we derive that γ_- is always negative for small enough detunings δ, provided the following condition is satisfied:

$$G = \frac{\tilde{\gamma}_0\tilde{\gamma}_2}{\tilde{\gamma}_1} < -1 \tag{4.3.12}$$

For the typical case of focusing Kerr nonlinearity, the nonlinear coefficient is positive: $\tilde{\gamma}_0 > 0$, and therefore the above condition implies, in particular, that $\tilde{\gamma}_2 < 0$. While only one coefficient Γ_ω is needed to compute the modified nonlinear coefficient $\tilde{\gamma}$, see Equation 4.2.3, the condition in equation 4.3.12 is much more convenient for analysis of MI, as compared to the direct computation of γ_- from equation 4.3.6.

In the following section, As an example, we consider a suspended $300nm \times 500nms$ $Al_{0.25}Ga_{0.75}A$ waveguide [126] with the geometry and profile of one of the guided quasi-TE modes (dominant electric field component is oriented horizontally) shown in Figure 4.1.1. As we know, AlGaAs has a strong and instantaneous Kerr nonlinearity, and also the linear and two photon absorption[48, 129] are negligible when the operation wavelength is larger than $1.5\mu m$. Figure 4.2.3 shows that the GVD is normal ($\beta_2 < 0$) for $\lambda > 1.659\mu m$. The nonlinear coefficient $\tilde{\gamma}$ is shown in Figure 4.2.1. Analysis of the equation 4.3.12 indicates possibility to observe MI in a wide window of wavelengths within the range of normal GVD: $1.66\mu m < \lambda < 1.76\mu m$, see Figure 4.2.3(b) and shaded area in Figure 4.2.3(a). The plot of $\delta\beta$ as function of the signal and idler wavelengths is shown in Figure 4.3.1(a). One can see that $\delta\beta$ is negative over the whole range. It should be emphasized that, for $\delta\beta < 0$, MI condition can be satisfied only via the mechanism of dispersion of nonlinearity compensating for the linear mismatch, which is independent from higher order dispersions of linear

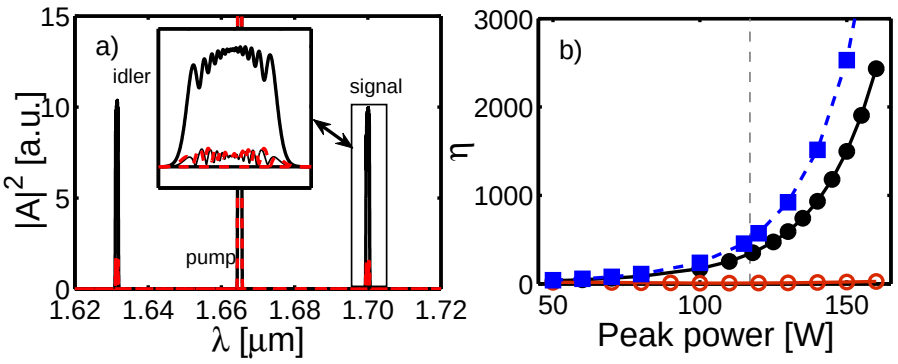

Figure 4.3.4: MI development with $100ps$ pulse excitation: (a) output spectra in frequency domain after $z = 0.4mm$ propagation distance. The pump, signal and idler wavelengths are: $\lambda_p = 1.665\mu m$, $\lambda_s = 1.7\mu m$, $\lambda_i = 1.6314\mu m$. Thin solid curve corresponds to wavelength-independent nonlinearity, dotted red/gray curve to self-steepening only, and thick solid curve to full dispersion of nonlinearity. Pump peak power is $150W$. The inset shows the MI at signal wavelength $1.7\mu m$. (b) Conversion efficiency as a function of the pump peak power. Full/open circles correspond to the full/self-steepening only dispersion of nonlinearity. Full squares correspond to the same as full circles, but for $10ps$ pulse excitation. Vertical dashed line indicates the threshold power for the case of three interacting waves [126]. The signal peak power is fixed to $0.1mW$ in all simulations.

wave.

Choosing $\lambda_p = 2\pi c/\omega_p = 1.665\mu m$, we compute γ_- by using the original definition in equation 4.3.6 and the reduced expression in equation 4.3.11; both appear to be in good agreement as shown in Figure 4.3.1(b). For comparison, we also compute γ_- by using the standard definition of the nonlinear coefficient, i.e., by replacing all $\tilde{\gamma}_i$ with γ_i in equation 4.3.11, see the dashed curve in Figure 4.3.1(b). Apparently, the modified nonlinear coefficient, which has been derived on the basis of the factorization approximation in equation 4.1.3, gives a much better agreement with the original model in equation 2.3.18.

The computed coefficient γ_- is negative in the broad range of the signal and idler wavelengths. This result is consistent with the condition in equation 4.3.12. While $\delta\beta$ is negative for the chosen pump wavelength, see Figure 4.3.1(a), MI can be provided only through the mechanism related to the dispersion of nonlinearity. Figure 4.3.2 shows the computed gain coefficient g for the pump power of $|A_p|^2 = 150W$. In this case, the maximum gain of $g = 5000m^{-1}$ is achieved for the signal located at around $\lambda_s = 1.7\mu m$ (idler is at $\lambda_i = 1.63\mu m$). It is instructive to note that the MI length is $L_{ML} = 1/g \sim 0.2mm$. In our simulation, for the duration of pulse $T_0 = 100ps, 10ps$, , the dispersion length $L_D = T_0^2/|\beta_2|$ and the walk-off length $L_W = T_0/|1/v_{g,s} - 1/v_{g,i}|$ between the signal and idler wave are both much larger than the MI length, which ensure that our analytical approach can provide a good prediction. For pump wavelength $\lambda_p = 1.665\mu m$, the threshold pump power P_{th} is computed and is shown in Figure 4.3.3 by using equations 4.3.6(red curve) and 4.3.11(black curve). They are considerably in agreement with each other, which provides a further evidence about the MI predicted by equation 4.2.4. It should be noted that the $P_{th} = 115W$ for $\lambda_s = 1.7\mu m$ ($\lambda_i \approx 1.63\mu m$).

While the condition in equation 4.3.6 was obtained under approximation of three interacting harmonics, to analyze the role of finite pump bandwidth and higher harmonics excitation in the development of MI, the picosecond sech pulse centered at wavelength $1.665\mu m$ with duration T_0= $100ps$ and peak power $150W$ is incident to waveguide together with a weak signal wave at $1.7\mu m$ with the same duration (peak power $0.1mW$). The signal pulse triggers MI and is located at the wavelength for which the maximum gain is predicted

when CW pump of the same power is used, see Figure 4.3.2. Such setup corresponds to the case of seeded MI [139]and requires relatively short propagation distances if compared to noise- or waveguide impurity-induced MI. The orders of polynomial expansions of linear and nonlinear dispersion operators, equations 4.2.5 and 4.2.6, were taken as $N_D = 11$ and $N_G = 7$, respectively, providing with a good fit of numerically computed functions $\beta(\omega)$ and $\tilde{\gamma}(\omega)$ across the range of wavelengths $1.4\mu m < \lambda < 2\mu m$.

The output spectrum in frequency domain after the propagation distance up to $z = 0.4mm$ are demonstrated in Figure 4.3.4(a). Both signal and idler are boosted in power due to the development of MI. To confirm the importance of the dispersion of nonlinearity in this process, we repeated simulations with the truncated versions of the nonlinear operator in 4.2.6 having $N_G = 0$ (wavelength-independent nonlinearity) and $N_G = 1$ (self-steepening only). In both cases, the output signal and idler spectral peaks are similar (they are nonzero because the signal is seeded) and significantly lower than those with the full dispersion of nonlinearity operator, see Figure 4.3.4(a).

To investigate the impact of peak power of the pulse on MI, we introduce the conversion efficiency η , which is defined as:

$$\eta = \frac{p_{i,out}}{p_{s,in}}$$

where $p_{i,out}$ is the output power of idler wave and $p_{s,in}$ is the input power of signal wave. In Figure 4.3.4(b) the conversion efficiency [139] is plotted as function of the pump pulse peak power. $p_{i,out}$ and $p_{s,in}$, were computed by the integration of the respective narrow frequency intervals. According to the analytical estimation based on the three waves approximation, no gain is possible below the threshold pump power P_{th}, while above this threshold the gain increases with pump power [126]. For the chosen signal wavelength, from Figure 4.3.3, we evaluate the threshold power to be $P_{th}(\lambda = 1.7\mu m) = 115W$, see the vertical dashed line in Figure 4.3.4(b). When using pulse excitation, we found that the conversion efficiency grows steadily with the pump power. Note that if we keep the self-steepening type of dispersion of nonlinearity only, the conversion efficiency remains low at all powers, see open circles in Figure 4.3.4(b). This confirms that the observed gain is due to the higher-order

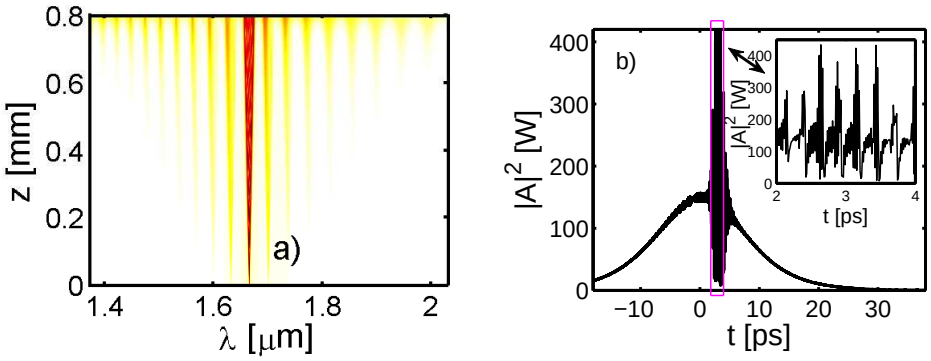

Figure 4.4.1: MI development with $10ps$ pulse excitation: (a) evolution of the spectrum with propagation distance and (b) output signal in time domain after the propagation distance of $z = 0.8mm$. The inset zooms in the central region of the pulse, where formation of a periodic sequence of ultra-short pulses is clearly visible. The pump/ seed peak power is $150W./0.1mW$; other parameters are the same as in Figure 4.3.4.

dispersion of nonlinearity.

For shorter pulse durations we obtained qualitatively similar results, but the conversion efficiency becomes higher, see full squares in Figure 4.3.4(b). This growth can be explained by the spectral broadening of the signal and idler due to the self-phase modulation[1], which becomes more pronounced for shorter pulses. The broadening effectively acts as a secondary seed, expanding the range of seed/idler frequencies to be parametrically amplified.

4.4 Frequency comb generation

As the signal $(\omega_p + \delta)$ and idler $(\omega_p - \delta)$ are amplified continuously, the sidebands at $\omega_p \pm \delta$ eventually become strong and the perturbation becomes very large. Therefore, as we know, the linear stability analysis is not valid. Evolution of the modulated state is then completely governed by the NLS equation 4.2.4. From Figure 4.4.1(a), one can see that their interaction with the pump produces higher-order sidebands, which are located at $\omega_p \pm m\delta$ $(m = 2, 3, ...)$. The process is repeated in the cascaded manner, eventually leading to the generation of a frequency comb. In time domain, this corresponds to the formation of a periodic sequence of ultrashort pulses, see Figure 4.4.1(b).

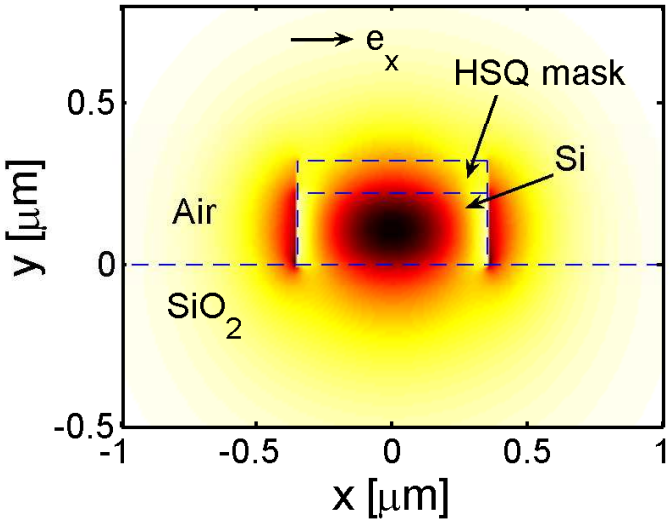

Figure 4.5.1: Geometry and profile of the dominant electric field component of the quasi-TE guided mode in subwavelength SOI waveguide for $\lambda_0 = 2.3\mu m$.

4.5 Spectral broadening in SOI waveguide

In this section, we discuss the impact of dispersion of nonlinearity on spectral broadening of ultrashort pulses. This renowned phenomenon occurs in a wide range of nonlinear media. Particularly in optical fibers, octave-wide spectral broadening from a sub-picosecond pulse, optical supercontinuum, has been studied for decades and applied to a range of fields as the convenient tool for generation of coherent radiation [140]. The theoretical foundation for spectral broadening in optical fibers is well established nowadays; in particular, it is recognized that the phenomenon occurs as the interplay between linear dispersion and nonlinearity. The broadest spectra are achieved by pumping near the zero GVD wavelength, where the dispersion changes its sign from anomalous to normal or vice versa [140].

Recently, spectral broadening and frequency conversion in SOI waveguides has become a focus of research [141, 112]. High nonlinear coefficient of silicon, combined with strong and tunable dispersion of SOI nano-waveguides, ensures nonlinear effects happening more effectively and over much shorter propagation distances than in conventional fibers. However, silicon has strong two-photon absorption (TPA) near the standard telecom wavelength of $\lambda = 1.55\mu m$[49],

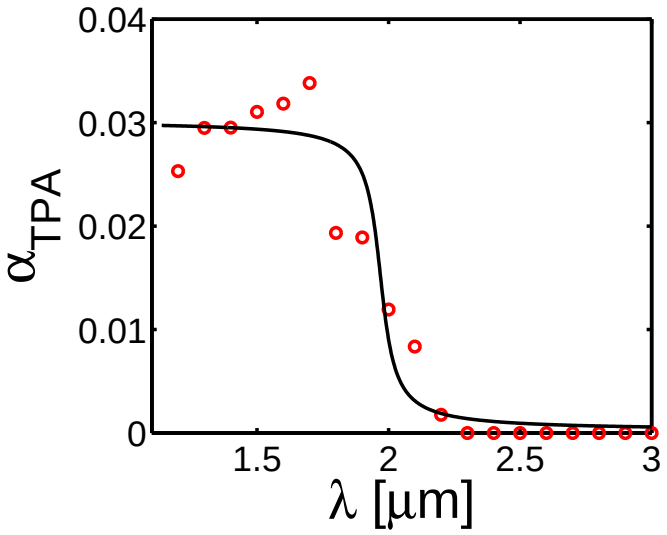

Figure 4.5.2: TPA rate in bulk silicon: experimental data adapted from [49] (circles) and analytical fit used in our calculations (solid curve).

which brings major limitations to the nonlinear performance of SOI waveguides. TPA can be characterized by the ratio α_{TPA} of the real and imaginary parts of the nonlinear susceptibility of silicon [88]:

$$\chi^{(3)} = \chi(1 + i\alpha_{TPA}).$$

Figure 4.5.2 shows the experimental data for α_{TPA} in bulk silicon (adapted from [49]) together with a simple fit $\alpha_{TPA} = 0.03/\pi.[arctan((\omega-\omega_c)/\omega)+\pi/2]$, $\lambda_c = 2\pi c/\omega_c = 2{\cdot}10^{13}s^{-1}$,used in our calculations. As one can see, TPA sharply drops and becomes practically negligible beyond $2\mu m$.

We choose the geometry of SOI waveguide shown in Figure 4.5.1. For the selected waveguide dimensions, the quasi-TE mode has zero GVD at $\lambda \approx 2.27\mu m$, see Figure 4.5.3(a). By pumping near this wavelength, one should expect to benefit from a reduced TPA rate. Figure 4.5.4 illustrates spectral broadening for the case of $100fs$ input sech pulse with the peak power of $100W$ and central wavelength of $\lambda_0 = 2.2\mu m$. This result was obtained by numerical integration of equation4.2.4 with the wavelength-independent nonlinear coefficient, i.e., $N_G = 0$ in the expansion of the nonlinear operator in equation 4.2.6, and with no account of TPA. The spectrum evolves following the typ-

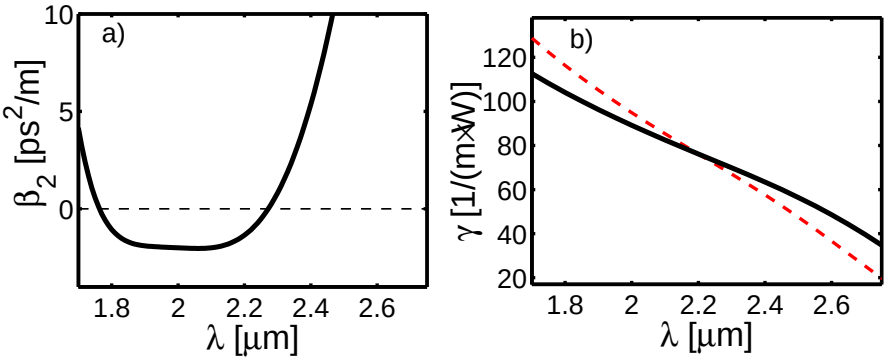

Figure 4.5.3: (a) Calculated GVD and (b) nonlinear coefficient (real part), for the quasi-TE mode of SOI waveguide shown in Figure 4.5.1. Solid/dashed curve in (b) corresponds to the modified/conventional ($\tilde{\gamma}/\gamma$) nonlinear coefficient. In numerical simulations, we used polynomial fits of orders $N_D = 6$ and $N_G = 4$ to reproduce $\beta_2(\omega)$ and $\tilde{\gamma}(\omega)$dependencies, respectively.

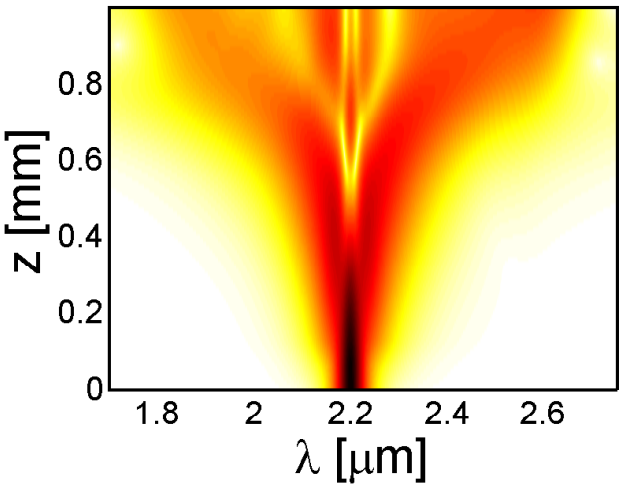

Figure 4.5.4: Spectral broadening in SOI waveguide pumped at $\lambda_0 = 2.2\mu m$ by a $100fs$ pulse with $100W$ peak power. The result is obtained for the case of wavelength-independent nonlinear coefficient, $\tilde{\gamma} = Const.$, TPA is neglected.

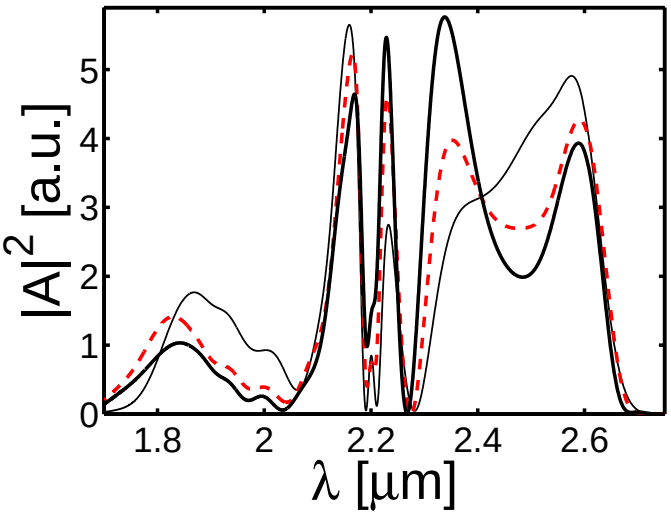

Figure 4.5.5: Spectral broadening in SOI waveguide: geometrical dispersion of nonlinearity. Output spectra at $z = 1mm$ calculated for the cases of wavelength-independent nonlinearity $\tilde{\gamma} = Const$. Const: (thin solid curve), self-steepening nonlinearity $\tilde{\gamma} = \omega\Gamma_0$ (dashed red/gray curve), and fully dispersive nonlinearity $\tilde{\gamma} = \omega\sqrt{\Gamma_0\Gamma}$ (thick solid curve). Input parameters are the same as in Figure 4.5.4.

ical two-stage scenario [140]. At the first stage ($0 < z < 0.7mm$) spectrum broadens symmetrically due to the self-phase modulation of the pulse. For larger distances, the interplay between dispersion and nonlinearity becomes important. This causes a considerable spectral asymmetry, with more power being concentrated in the long-wavelength part of the spectrum.

After $z = 1mm$ propagation distance, the output spectrum covers the wide range of wavelengths $1.8\mu m < \lambda < 2.6\mu m$. According to our calculations, the real part of the nonlinear coefficient changes significantly in this wavelength range, see Figure 4.5.3(b). Also, a large part of the output spectrum falls into the range of strong TPA. Therefore, both geometrical and material dispersions of nonlinearity are expected to influence the spectral broadening process.

In Figure 4.5.5, output spectra are compared for three different cases: with constant nonlinear coefficient, self-steepening only, and full geometrical dispersion of nonlinearity. TPA was disregarded in all these simulations. Self-steepening enhances spectral asymmetry by lowering and shifting peak in the short-wavelength part of the spectrum and separating the long-wavelength

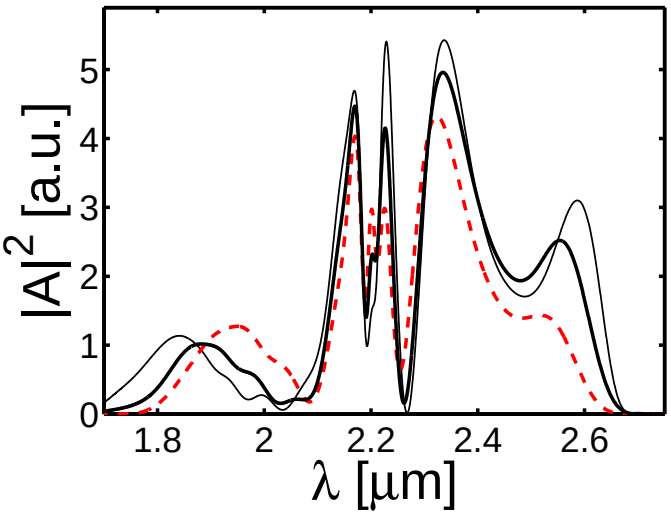

Figure 4.5.6: Spectral broadening in SOI waveguide: dispersion of TPA. Output spectra at $z = 1mm$ calculated for the cases of no TPA (thin solid curve), wavelength-independent TPA $\alpha_{TPA} \equiv 0.03$ (dashed red/gray curve), and dispersive TPA (thick solid curve) as in Figure 4.5.2. Full geometrical dispersion of nonlinearity is taken into account. Input parameters are the same as in Figure 4.5.4.

edge spectral peak from the central three-peak structure formed during the self-phase modulation stage. Geometrical dispersion further boosts the asymmetry, especially enhancing features in the long-wavelength wing.

The effect of dispersion of TPA is summarized in Figure 4.5.6, where we compare cases of no TPA, wavelength-independent TPA, and dispersive TPA. As expected, inclusion of flat TPA rate $\alpha_{TPA} \equiv 0.03$ (Oviously, the part of spectral in the short wavelength wing falls into the range of wavelengths $1.7\mu m < \lambda 1.9\mu m$, in which TPA is quite strong, see Figure 4.5.2.) results in overall shrinking of the spectrum. Perhaps more surprisingly, fully dispersive TPA does not bring any noticeable spectral asymmetries and effectively acts as a reduced flat TPA. The reason for that is in the link between short- and long-wavelength wings of the spectrum, which has been analyzed in details in the context of supercontinuum generation in fibers [140]. In particular, spectral features in the normal GVD wing of generated supercontinua are generally defined by the positions and intensities of spectral peaks in the anomalous GVD wing. Apparently, this relation holds in the equation2.3.18: while TPA affects

mostly the short-wavelength wing of the spectrum (where GVD is anomalous), the spectral peaks in the long-wavelength wing (normal GVD) change accordingly.

4.6 Summary

Due to tight optical field confinement in subwavelength waveguide, the dispersion of nonlinear response can be increased significantly. Specifically, because of the low nonlinear loss in AlGaAs waveguides, we demonstrated that the MI exists for picsecond pulse under an appropriate threshold power, which is arisend from dispersion of nonlinearity independently in the regime of normal group velocity dispersion, by using a generalized NLS equation 4.2.4 with all the dispersion coefficients including nonlinear contributions derived from Maxwell equations following the perturbation expansion procedure by introducing factorization of the four-frequency dependence of the nonlinear coefficients Γ_{nklm}. The factorization was tested on different semiconductor waveguide geometries and found to approximate well the actual coefficients in the wide wavelength ranges, although a careful analysis of the general conditions of applicability of this approximation is still needed for future research.

Based on this model, the new MI gain and condition expressions have been obtained. Also, our results indicate that spectral broadening of pulses due to self-phase modulation plays an important role in the development of MI. In particular, MI is observed for pump pulse peak powers well below the threshold predicted for CW pump [126]. In addition, the conversion efficiency becomes higher when shorter pulses are used. Similar to the conventional MI, long-term evolution of the dispersion of nonlinearity induced MI leads to the cascaded generation of higher-order sidebands and associated formation of a sequence of ultrashort pulses.

We also considered an impact of the dispersion of nonlinearity on spectral broadening of short pulses in a SOI waveguide. We chose the geometry where the zero of GVD is located at around $\lambda = 2.27\mu m$. Pumping by $100fs$ pulses with $100W$ peak power in a vicinity of this wavelength, a considerable spectral broadening can be observed with the output spectra spanning from 1.8 to $2.6\mu m$. The nonlinear coefficient changes significantly in this wavelength

range, causing clearly pronounced spectral asymmetries. Also, for silicon, the ratio of TPA to Kerr coefficients changes sharply around $\lambda = 2.2\mu m$, reaching its highest rate of $\alpha_{TPA} \approx 0.03$ below $1.9\mu m$ and being practically zero above $2.1\mu m$. However, the account for dispersive imaginary part of the nonlinear coefficient does not introduce any noticeable additional asymmetry in the output spectra, causing nearly even shrinkage and power loss on either side of the spectrum. This counterintuitive result is explained by the internal link between the edges of the spectrum, well analyzed in the context of optical fibers[140]. Although the long-wavelength wing remains in the range of negligibly small TPA, its structure still changes accordingly with the short-wavelength wing, the latter being affected by the strong TPA.

Chapter 5

Modulation instability and oscillating solitons in dielectric-metal-dielectric waveguides with PT-symmetry

MI is a well known phenomenon induced by nonlinearity in many branches of physics[143]. in nonlinear optics, the small noise or perturbation rapidly enhances because of the interaction of nonlinearity and diffraction or dispersion. Consequently, a constant amplitude pump wave or a broad optical beam decay into pulse trains or optical filaments, respectively. It was found that MI can lead to "oscillons" (or oscillating solitons) in granular[144] systems, and also it is a mechanism behind the generation of rogue waves[145, 146, 147].

Recently, studies in quantum mechanics by Bender and co-worker demonstrated that even non-Hermitian Hamiltonians can have entirely real spectra provided they obey parity-time (PT) symmetry[148]. Generally, the action of the parity P and time T operators is defined as $\hat{p} \rightarrow -\hat{p}, \hat{x} \rightarrow -\hat{x}$ and $\hat{p} \rightarrow -\hat{p}, \hat{x} \rightarrow \hat{x}, i \rightarrow -i$ (here, $\hat{p}$,$\hat{x}$ stand for momentum and position operators, respectively). It was found that Hamiltonian $\hat{H} = \hat{p}^2/2m + V(\hat{x})$ is PT symmetric if the condition $V(\hat{x}) = V^*(-\hat{x})$ is satisfied, where V is the potential and m is mass. In other words, PT symmetry requires that the real part of the potential V is an even function of position x , while the imaginary part is odd, which means that the Hamiltonian has the form $\hat{H} = \hat{p}^2/2m + V_R(\hat{x}) + i\epsilon V_I(\hat{x})$,

where V_R and V_I are the symmetric and antisymmetric functions, respectively. One can see that the Hamiltonian is Hermitian only when $\epsilon = 0$.

Optics provides an appropriate platform in which PT concept from quantum mechanics can be realized analytically and experimentally. In particular, the quantum mechanical Schrodinger equation is equivalent to the pulse propagation equation and the real and imaginary parts of the index of refraction can be manipulated. Based on these considerations, we can design a PT-symmetric system by satisfying $n_R = n_R(-x), n_I = -n_I(-x)$. Such PT-symmetric system firstly has been achieved in optical coupler with balanced gain and loss[149] and in the temporal lattices[150]. The intriguing properties of PT symmetry causes extensive interests in theory and experiment[151, 152, 153, 154, 155, 156, 157, 158, 159, 160, 161, 162, 163, 164, 165]. Light in a linear couplers with PT-symmetry propagates in a non-reciprocal manner[149]. Beam dynamics (especially, Bloch oscillation and discrete diffraction) in PT-symmetric lattices has been investigated[151, 152, 153, 154, 155]. By considering the nonlinearity of the waveguides, the optical soliton[166, 167, 168] in different PT potentials and breathers[165]in optical couplers have been observed theoretically. Therefore, these experimental and theoretical works discussed above suggest that such dielectric waveguides with PT-symmetry can be used for light controlling.

Lately, due to the ability to manipulate light in a nanometer size regime and a great deal of applications from nanoscale photonic devices to biological sensors[171, 172], in dielectric-metal (plasmonic) systems, surface plasmon polaritons (SPPs), which are exponentially localized, are explored extensively. The stable spatial plasmon soliton excited below the surface plasmon frequency has been demonstrated by using Ginzburg-Landau equation in dielectric-metal waveguides with gain and loss[177, 178, 179]. On the other hand, specifically, the localized surface plasmon resonances (localized SPPs) have been excited by direct illumination using arrays of plasmonic nanotubes[173, 174]. Furthermore, for a nanoparticle chain driven by an optical field with the frequency close to the frequency of the surface plasmon resonance of an individual particle, oscillating soliton (oscillon) has been found[175, 176].

Inspired by these works, it is natural to expect that the combination of strong surface plasmon resonances and PT-symmetry may open up a new way

for light manipulating. In this chapter, importantly, one assumption is made by assuming that the localized SPPs can be described by two coupled equations (see below). Based on these equations, we investigate the temporal evolutions of fundamental and one-ring solitary waves with phase dislocation in dielectric-metal-dielectric waveguides with PT-symmetry and numerically analyze the properties of these nonlinear localized modes and reveal different scenarios of their instability. In particular, we demonstrate that the stable oscillating soliton and long-lived breather do exist over a wide range of parameters (see below for details).

5.1 Model and stationary solutions

As mentioned above, SPPs are guided along metal-dielectric interfaces and can be created through the coupling of the light to oscillations of the conductor's electron plasma. There are two kinds of SPPs depending on how they are excited. One is the SPPs propagating at a interface excited at frequencies below the surface plasmon frequeny ω_{sp}[177, 180]. The model describing propagating SPPs has been derived in different geometries by taking into account the full vectorial nature of the guided waves[177, 179, 181]. The other one is the localized SPPs[133, 180] excited at frequencies close to ω_{sp}. In particular, in the absence of damping of the conduction electron oscillation[180], as the frequency approaches ω_{sp}, the wave vector β goes to infinity and the group velocity v_g tends to 0, which implies that the SPPs is confined to the interface without propagating. Here, in the case of localized SPPs, to demonstrate the dynamics of the self-trapped beams in sandwich waveguides composed of two dielectric layers with gain and loss and a thin metal stripe where SPPs at the two interfaces are coupled, which is schematically depicted in Figure 5.1.1(a), two coupled equations, which describe the temporal evolution of localized SPPs, are employed. By scaling our variables carefully, we obtain the following dimensionless form:

$$iU_t + U_{xx} + U_{yy} + \frac{|U|^2 U}{1 + \alpha|U|^2} = -V + i\gamma U$$

$$iV_t + V_{xx} + V_{yy} + \frac{|V|^2 V}{1+\alpha|V|^2} = -U - i\gamma V \tag{5.1.1}$$

Here t is the temporal coordinate and x and y are the transverse coordinates. The in-plane diffraction of SPPs happens along x and y directions, see Figure 5.1.1(a). α is a saturation parameter and by taking $\alpha = 0$, Kerr nonlinearity can be recovered. The U and V variables are the normalized complex amplitudes. In the right-hand side of equation 5.1.1, the first terms describe the coupling between two modes through the overlap of their tails. The second terms account for the balanced gain in the top layer and loss in the bottom layer, which explains how the PT-symmetry can be achieved by properly choosing the complex refractive index[149].

It should be noted that one can find stable solitons within certain area employing Kerr nonlinearity in two dielectric layers when the in-plane diffraction of SPPs happens along x or y direction[169]. However, for Kerr nonlinearity, by extending the system to include two diffraction directions, we found that stationary solutions are unstable in the whole parameter plane of a and γ (see Figure 5.3.1). Therefore, in this work, we only focus on self-focusing saturable nonlinearity. Before we start our analysis, we should note that, in this dissipative system, the individual powers and total power are both not conserved if $\gamma \neq 0$. However, they can provide very useful information for the understanding of the soliton and MI, therefore we write these two expressions here for convenience:

$$P_U = \iint |U|^2 dxdy, P_V = \iint |V|^2 dxdy \tag{5.1.2}$$

$$P_T = P_U + P_V \tag{5.1.3}$$

Below, in order to obtain the stationary solutions in sandwich waveguides with saturable nonlinearity, it is convenient to introduce the polar coordinate and finally we arrive at:

$$i\frac{\partial U}{\partial t} + \frac{\partial^2 U}{\partial r^2} + \frac{1}{r}\frac{\partial U}{\partial r} + \frac{1}{r^2}\frac{\partial^2 U}{\partial \varphi^2} + \frac{|U|^2 U}{1+\alpha|U|} = -V + i\gamma U$$

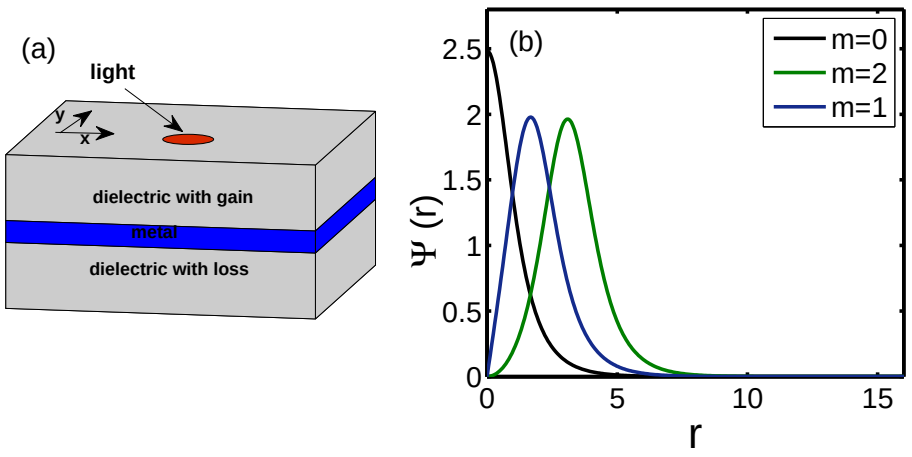

Figure 5.1.1: (a) A schematic of dielectric-metal-dielectric structure with gain (top layer) and loss (bottom layer). (b) Plot of the field amplitude $\Psi(r)$ for $m = 0, 1, 2$, and $\gamma = 0.4, a = 1.0409, \alpha = 0.1$.

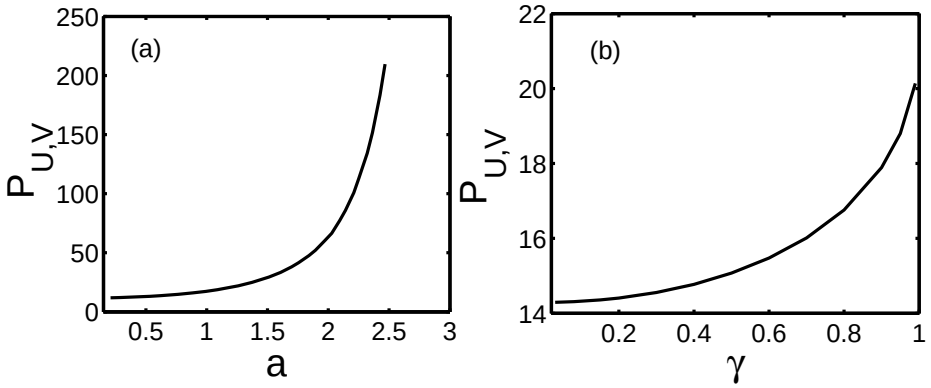

Figure 5.1.2: Plots of power $P_{U,V}$ for fundamental solitons as function of a and γ. The values of parameters are as follows: (a), $\gamma = 0.4$; (b),$\Omega = 1.5$. Note that $\cos\theta > 0$ for both plots.

$$i\frac{\partial V}{\partial t}+\frac{\partial^2 V}{\partial r^2}+\frac{1}{r}\frac{\partial V}{\partial r}+\frac{1}{r^2}\frac{\partial^2 V}{\partial \varphi^2}+\frac{|V|^2 V}{1+\alpha|V|^2}=-U-i\gamma V \tag{5.1.4}$$

We make a transformation by using the following form[169]:

$$U(r,\varphi,t)=e^{i(\Omega t-\theta)}u(r)e^{im\varphi}, V(r,\varphi,t)=e^{i\Omega t}v(r)e^{im\varphi} \tag{5.1.5}$$

where θ is a constant satisfying $\gamma=\sin\theta$ and Ω is a real parameter. m must be integer. For the ground state, there is no phase singularity, thus, $m=0$. Substituting 5.1.5 to 5.1.4, the resulting coupled equations in polar coordinate are:

$$-\Omega u+\frac{\partial^2 u}{\partial r^2}+\frac{1}{r}\frac{\partial u}{\partial r}-\frac{m^2}{r^2}u+\frac{|u|^2 u}{1+\alpha|u|}=-v\cos\theta+i\gamma(u-v)$$

$$-\Omega v+\frac{\partial^2 v}{\partial r^2}+\frac{1}{r}\frac{\partial v}{\partial r}-\frac{m^2}{r^2}v+\frac{|v|^2 v}{1+\alpha|v|^2}=-u\cos\theta+i\gamma(u-v) \tag{5.1.6}$$

Furthermore, to find a special stationary solution, we assume $u=v=\Psi$. Therefore, the equations 5.1.6 are reduced to the scalar nonlinear Schrodinger equation:

$$\frac{\partial^2\Psi}{\partial r^2}+\frac{1}{r}\frac{\partial\Psi}{\partial r}-\frac{m^2}{r^2}\Psi-a^2\Psi+\frac{|\Psi|^2\Psi}{1+\alpha|\Psi|}=0, \tag{5.1.7}$$

where $a^2=\Omega-\cos\theta$. Note that, according to the sign of $cos\theta$, the stationary solution of equation 5.1.7 can be classified into two families. One has $cos\theta=\sqrt{1-\gamma^2}>0$; the other one has $cos\theta=-\sqrt{1-\gamma^2}<0$. It should be stressed that only when $\gamma<1$, these two families solutions could exist. Assuming that this restriction always holds, equation 5.1.7 was solved numerically using Newton method. Typical profiles of Ψ for different values of m are presented in Figure 5.1.1(b). In addition, for fundamental solutions, Figure 5.1.2 shows that the power $P_{U,V}$ increases with a and γ when $\cos\theta>0$. We also found two-, three-, and many-ring solutions with or without a central phase singularity. However, in this work, currently, we only concentrate on the ground state and one-ring solution with a phase singularity

at the center. As we know, based on equation 5.1.7 (in conserved systems), numerical simulations and analytical method through applying the Vakhitov-Kolokolov stability criterion[5, 170] indicate that all of the ground states in the saturable media are stable. Also, all higher-order solitons (soliton with one or two or many rings) are not stable although the saturable nonlinearity can suppress the instability[182]. In the Hamiltonian systems, because of an azimuthal symmetry-breaking instability, it was shown that, theoretically, the ring-shaped solitons break up into mutiple fundamental solitons depending on topological charge m[170, 183, 184, 185]. This kind of instability has been observed experimentally in Kerr-type and quadratic nonlinear media[186, 187, 188]. Our aim in next section is to numerically investigate the stability of these special solutions 5.1.5 (solutions with or without phase dislocation) in dielectric-metal-dielectric waveguides with saturable nonlinearity for dissipative system.

5.2 Linear stability analysis

The stationary solutions are not necessarily stable. Therefore, one should study how they react to small perturbation. The linear stability analysis is well established for the models similar to ours[5]. Below, we follow the normal procedure as described in Refs.[5]to analyze the stability of the stationary solutions obtained by numerically solving the equation 5.1.7.

To identify the stability of the two families of solitons, we consider the small perturbations of the stationary solution:

$$U(r,\varphi,t) = \Psi(r) + \delta U(r,\varphi,t), V(r,\varphi,t) = \Psi(r) + \delta V(r,\varphi,t) \qquad (5.2.1)$$

and linearize the equations 5.1.4 in δU and δV . The following coupled equations are obtained:

$$i\frac{\partial \delta U}{\partial t}+\frac{\partial^2 \delta U}{\partial r^2}+\frac{1}{r}\frac{\partial \delta U}{\partial r}-\frac{m^2}{r^2}\delta U+\frac{1}{r^2}\frac{\partial^2 \delta U}{\partial \varphi^2}+\frac{2im}{r^2}\frac{\partial \delta U}{\partial \varphi}-\Omega\delta U+\frac{\Psi^2\delta U}{1+\alpha\Psi^2}$$
$$+\frac{\Psi^2\delta U}{(1+\alpha\Psi^2)^2}+\frac{\Psi^2\delta U^*}{(1+\alpha\Psi^2)^2}=-\cos\theta\delta V+i\gamma(\delta U-\delta V) \tag{5.2.2}$$

$$i\frac{\partial \delta V}{\partial t}+\frac{\partial^2 \delta V}{\partial r^2}+\frac{1}{r}\frac{\partial \delta V}{\partial r}-\frac{m^2}{r^2}\delta V+\frac{1}{r^2}\frac{\partial^2 \delta V}{\partial \varphi^2}+\frac{2im}{r^2}\frac{\partial \delta V}{\partial \varphi}-\Omega\delta V+\frac{\Psi^2\delta V}{1+\alpha\Psi^2}$$
$$+\frac{\Psi^2\delta V}{(1+\alpha\Psi^2)^2}+\frac{\Psi^2\delta V^*}{(1+\alpha\Psi^2)^2}=-\cos\theta\delta U+i\gamma(\delta U-\delta V) \tag{5.2.3}$$

It is convenient to make a transformation by using the symmetric and anti-symmetric combinations:

$$p=\delta U+\delta V, q=\delta U-\delta V.$$

Hence, the new form of linearized equations 5.2.2 and 5.2.3 are given by:

$$i\frac{\partial p}{\partial t}+\frac{\partial^2 p}{\partial r^2}+\frac{1}{r}\frac{\partial p}{\partial r}-\frac{m^2}{r^2}p+\frac{1}{r^2}\frac{\partial^2 \delta U}{\partial \varphi^2}+\frac{2im}{r^2}\frac{\partial p}{\partial \varphi}-\Omega p+\frac{\Psi^2 p}{1+\alpha\Psi^2}$$
$$+\frac{\Psi^2 p}{(1+\alpha\Psi^2)^2}+\frac{\Psi^2 p*}{(1+\alpha\Psi^2)^2}=-\cos\theta p+2i\gamma q \tag{5.2.4}$$

$$i\frac{\partial q}{\partial t}+\frac{\partial^2 q}{\partial r^2}+\frac{1}{r}\frac{\partial q}{\partial r}-\frac{m^2}{r^2}q+\frac{1}{r^2}\frac{\partial^2 q}{\partial \varphi^2}+\frac{2im}{r^2}\frac{\partial q}{\partial \varphi}-\Omega q+\frac{\Psi^2 q}{1+\alpha\Psi^2}$$
$$+\frac{\Psi^2 q}{(1+\alpha\Psi^2)^2}+\frac{\Psi^2 q*}{(1+\alpha\Psi^2)^2}=\cos\theta q \tag{5.2.5}$$

The general solution of the linearized problem for p and q can be expressed as a superposition of azimuthal Fourier modes $e^{\pm iJ\theta}$ $(J=0,1,2\cdots)$ with complex coefficients depending on r and t. Therefore, we set:

$$p=p_+(r)\exp(\nu t+iJ\varphi)+p_-^*(r)\exp(\nu^* t-iJ\varphi) \tag{5.2.6}$$

$$q = q_+(r)\exp(\nu t + iJ\varphi) + q_-^*(r)\exp(\nu^* t - iJ\varphi). \tag{5.2.7}$$

Substituting equations 5.2.6 and 5.2.7 into 5.2.4 and 5.2.5, the eigenvalue problem can be given by:

$$i\nu\overrightarrow{P} = \begin{bmatrix} L_+^p & \frac{\Psi^2}{(1+\alpha\Psi^2)^2} & 2i\gamma & 0 \\ \frac{-\Psi^2}{(1+\alpha\Psi^2)^2} & L_-^p & 0 & -2i\gamma \\ 0 & 0 & L_+^q & \frac{\Psi^2}{(1+\alpha\Psi^2)^2} \\ 0 & 0 & \frac{-\Psi^2}{(1+\alpha\Psi^2)^2} & L_-^q \end{bmatrix} \overrightarrow{P} \tag{5.2.8}$$

where the operators can be written as:

$$L_+^p = -(\frac{\partial^2}{\partial r^2} + \frac{1}{r}\frac{\partial}{\partial r} - \frac{(J+m)^2}{r^2} - \Omega + \frac{\Psi^2}{1+\alpha\Psi^2} + \frac{\Psi^2}{(1+\alpha\Psi^2)^2}) - \cos\theta$$

$$L_-^p = \frac{\partial^2}{\partial r^2} + \frac{1}{r}\frac{\partial}{\partial r} - \frac{(J-m)^2}{r^2} - \Omega + \frac{\Psi^2}{1+\alpha\Psi^2} + \frac{\Psi^2}{(1+\alpha\Psi^2)^2} + \cos\theta$$

$$L_+^q = -(\frac{\partial^2}{\partial r^2} + \frac{1}{r}\frac{\partial}{\partial r} - \frac{(J+m)^2}{r^2} - \Omega + \frac{\Psi^2}{1+\alpha\Psi^2} + \frac{\Psi^2}{(1+\alpha\Psi^2)^2}) + \cos\theta$$

$$L_-^q = \frac{\partial^2}{\partial r^2} + \frac{1}{r}\frac{\partial}{\partial r} - \frac{(J-m)^2}{r^2} - \Omega + \frac{\Psi^2}{1+\alpha\Psi^2} + \frac{\Psi^2}{(1+\alpha\Psi^2)^2} - \cos\theta$$

and

$$\overrightarrow{P} = \begin{bmatrix} p_+ \\ -p_- \\ q_+ \\ -q_- \end{bmatrix}.$$

In order to eliminate the singularity where the operators $L_+^p, L_-^p, L_+^q, L_-^q$ tend to infinity when $r = 0$, we introduce:

$$p_+ = x_1(r)r^{|m+J|}, p_- = x_2(r)r^{|m-J|} \tag{5.2.9}$$

$$q_+ = x_3(r)r^{|m+J|}, q_- = x_4(r)r^{|m-J|} \tag{5.2.10}$$

$$i\nu\overrightarrow{X} = \begin{bmatrix} L_+^1 & \frac{\Psi^2 r^{|m-J|-|m+J|}}{(1+\alpha\Psi^2)^2} & 2i\gamma & 0 \\ \frac{-\Psi^2 r^{|m+J|-|m-J|}}{(1+\alpha\Psi^2)^2} & -L_-^2 & 0 & -2i\gamma \\ 0 & 0 & L_+^3 & \frac{\Psi^2 r^{|m-J|-|m+J|}}{(1+\alpha\Psi^2)^2} \\ 0 & 0 & \frac{-\Psi^2 r^{|m+J|-|m-J|}}{(1+\alpha\Psi^2)^2} & -L_-^4 \end{bmatrix} \overrightarrow{X} \tag{5.2.11}$$

where

$$L_+^1 = -\frac{\partial^2}{\partial r^2} - \frac{2|J+m|+1}{r}\frac{\partial}{\partial r} + \Omega - \frac{\Psi^2}{1+\alpha\Psi^2} - \frac{\Psi^2}{(1+\alpha\Psi^2)^2}) - \cos\theta$$

$$L_-^2 = -\frac{\partial^2}{\partial r^2} - \frac{2|J-m|+1}{r}\frac{\partial}{\partial r} + \Omega + -\frac{\Psi^2}{1+\alpha\Psi^2} - \frac{\Psi^2}{(1+\alpha\Psi^2)^2} - \cos\theta$$

$$L_+^3 = -\frac{\partial^2}{\partial r^2} + \frac{2|J+m|+1}{r}\frac{\partial}{\partial r} + \Omega - \frac{\Psi^2}{1+\alpha\Psi^2} - \frac{\Psi^2}{(1+\alpha\Psi^2)^2}) + \cos\theta$$

$$L_-^4 = -\frac{\partial^2}{\partial r^2} - \frac{2|J-m|+1}{r}\frac{\partial}{\partial r} + \Omega - \frac{\Psi^2}{1+\alpha\Psi^2} - \frac{\Psi^2}{(1+\alpha\Psi^2)^2} + \cos\theta$$

and

$$\overrightarrow{X} = \begin{bmatrix} x_1 \\ -x_2 \\ x_3 \\ -x_4 \end{bmatrix}.$$

The equation 5.2.11 can be solved numerically. We reduce equation 5.2.11 to an algebraic eigenvalue problem by replacing the differential operators with the second-order finite differences. For large value of r, $\overrightarrow{X}$ tends to 0, and appropriate boundary conditions at $r = 0$ are given by equations 5.2.9 and 5.2.10. Although the equation 5.2.11can be applied for investigating the fila-

ment dynamics after ring breakup[170], in this work, we mainly focus on the MI of fundamental solitons ($m = 0$,or without phase singularity).

The numerical study of eigenvalue problem 5.2.11 offers a direct information about where the stable fundamental soliton can be expected. Figure 5.3.1 presents this results. For $cos\theta > 0$, we found that the eigenvalues ν are zeros below the solid blue line, which means that the stationary solutions do not grow exponentially with time. Above the solid blue line, the eigenvalues ν are real numbers, and consequently, the solutions are unstable. Note that, for $cos\theta < 0$, the solitons are all not stable based on linear stability analysis and direct numerical simulation. In contrast, the unstable eigenmodes have complex eigenvalues and the magnitude of real parts are much smaller than it of imaginary parts. We also found that the lifetimes of the solitons with small values of a (in Figure 5.3.8, below the dashed line with circles numerically found by using equations 5.1.1) are very long. Therefore, in practice, they can be observed.

5.3 Time evolution of solitons

To further identify the stable soliton and unstable soliton and test the results of our stability analysis obtained above, we performed considerable numerical simulations of equations 5.1.1 with initial conditions in the form:

$$U(r,\varphi) = e^{-i\theta}u(r)e^{im\varphi}(1 + s \cdot random),$$

$$V(r,\varphi) = v(r)e^{im\varphi}(1 + s \cdot random), \tag{5.3.1}$$

where $random$ is the complex function consisting of real and imaginary parts which are evaluated by the standard uniform distribution on the open interval $(0, 1)$ and s is a constant. Simulation was carried out by using equations 5.1.1 on the rectangular grid with 512×512 grid points along the x and y coordinates, respectively. As we know, generally the instability gets stronger for $\alpha \to 0$ and it could be suppressed when α gets larger[189, 190]. It should be noted that, in our simulations, we take $\alpha = 0.1$.

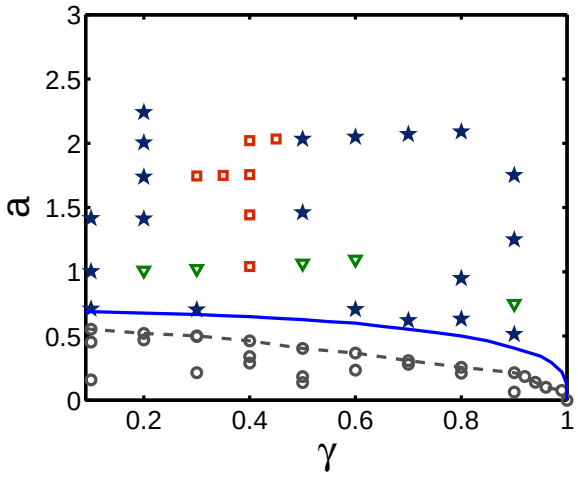

Figure 5.3.1: Plot of a as function of γ. The dashed curve with circles directly obtained by simulating the equations 5.1.1 with initial conditions 5.3.1 and the solid blue line based on linear stability analysis indicate the boundary between stable soliton and unstable soliton (breakup of solitons). The star markers represent breakup of solitons (see Figure 5.3.5). The triangular markers mean diffraction of solitons (see Figure 5.3.4). The rectangular markers indicate breather (see Figure 5.3.6). The circles indicates the stable oscillating soliton. The parameter $\alpha = 0.1$.

5.3.1 Solitons for $cos\theta > 0$

A solution of equations 5.1.4 is stable if none of the eigenmodes of the linear eigenvalue problem 5.2.11 grows exponentially. Soliton evolution with time is modelled numerically. Figure 5.3.1 presents the presence of stable fundamental soliton below the dashed line with circles and instabilities above the dashed line with circles. Three kinds of scenarios of instabilities have been identified.

Figure 5.3.2 shows the soliton evolution with time without initial noise. We performed a number of numerical simulations using equations 5.1.1 without initial noise. The solitons U and V almost stay unchanged apart from the small variation of the peak of soliton, see Figure 5.3.2(b). It should be emphasized that the demarcation line between the stable and unstable area based on numerical simulation is in agreement with the one from linear analysis (the solid blue line in Figure 5.3.1). From Figure 5.3.3(d), one can see that the individual power for U or V is a constant (the dashed grey line), which means that the gain can completely compensate for the loss during the evolution.

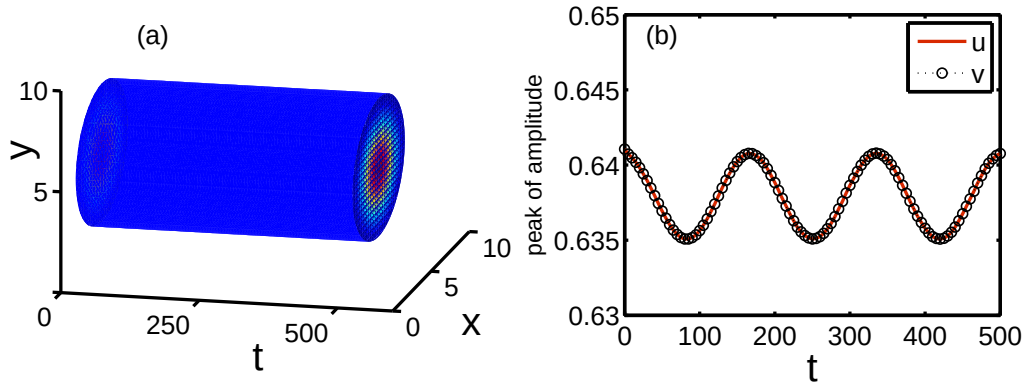

Figure 5.3.2: (a) The evolution of cross-sections of pulse along the time direction without adding noise. (b) Peaks of amplitude for U and V as function of time t. The parameters are as follows: $\gamma = 0.4, a = 0.2889, \alpha = 0.1$

To further examine the robustness of self-trapped fundamental PT modes U and V, considerable simulations have been done by adding low ($s = 0.01$) and high ($s = 0.025$) initial noises on amplitude and phase. Surprisingly, although the cross-section and peaks of solitons all vary with time notably, solitons can evolve stably for sufficient long time without any exponential decay or growth, see Figure 5.3.3(a)(b). Figure 5.3.3(c) shows that the period of peaks gets shorter whilst increasing the noise level. We should note that the individual power P_U and P_V and total power P_T have a very small fluctuation along the time axis, see Figure 5.3.3(d). We assume that the power is conserved and this kind of soliton is called oscillating soliton. It is found that there is the small discrepancy between the dashed curve with circle obtained by direct simulations with initial noise and solid blue line based on linear stability analysis (Figure 5.3.1). Notably, the stable area shrinks when one adds noise on the system with PT symmetry. From our simulations, adding smaller perturbations, we found that the border (dashed curve with circle) numerically obtained approaches the one (solid blue line) from stability analysis.

Figure 5.3.4, 5.3.5 and 5.3.6 present the three scenarios of instabilities. The triangular markers in Figure 5.3.1 represent the diffraction of the solitons, which means that the soliton spread everywhere with time evolution. One of examples is shown in Figure 5.3.4. the cross-sections of the U and V both

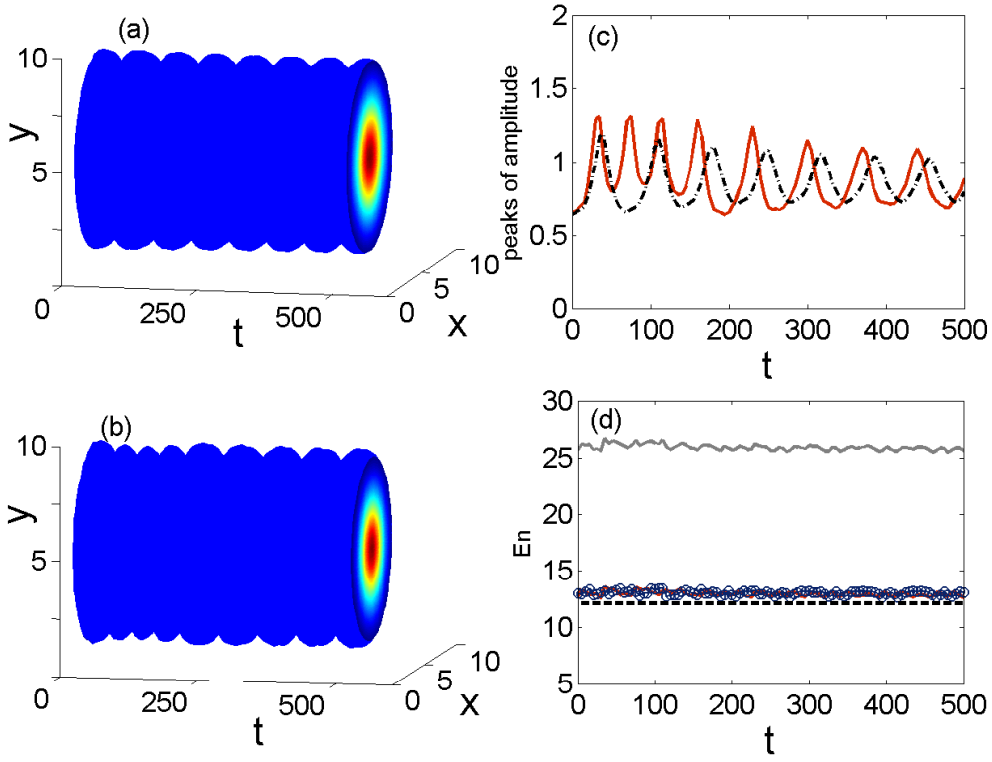

Figure 5.3.3: (a) and (b) show the evolution of cross-sections of envelope U along the time direction with $\gamma = 0.4, a = 0.2889, \alpha = 0.1$ and initial noise (a) $s = 0.01$, (b) $s = 0.025$. by adding noise to the initial amplitude and phase, we found that the oscillating soliton can propagate stably for long time. (c) Peaks of amplitude U with initial noise $s = 0.01$(dot-dash curve) and $s = 0.025$ (full red curve) as function of time t. (d) Horizontal dashed line mark the evolution of power for U without noise with time. Dashed line with circles and red full line indicate the individual power P_V and P_U , respectively, and the grey full line represents the total power P_T with noise $s = 0.025$.

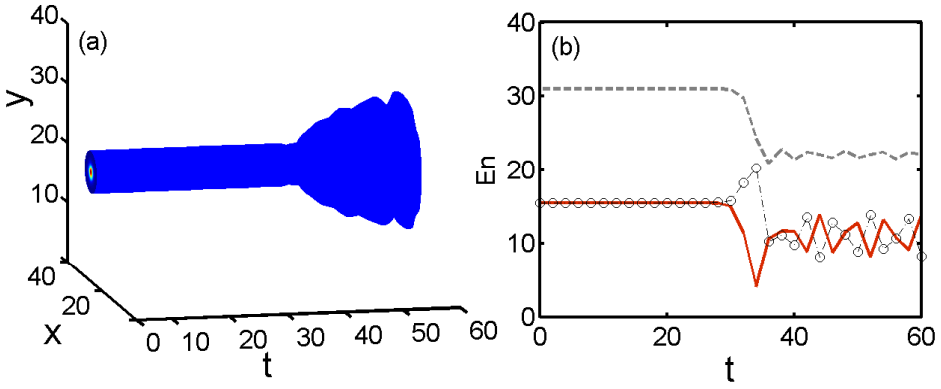

Figure 5.3.4: (a) The evolution of the cross-sections of soliton for U with $\gamma = 0.1, a = 0.8397, \alpha = 0.1$. (b) Dot-dash line with circles and red full line indicate the individual power for P_V and P_U , respectively, and the grey dashed line represents the total power P_T.

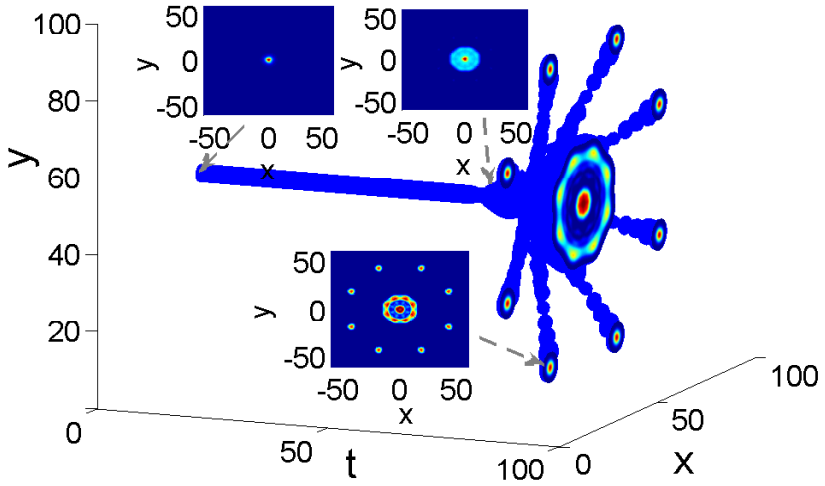

Figure 5.3.5: Breakup of the soliton for U with $\gamma = 0.9, a = 0.5739, \alpha = 0.1$. The insets indicate the cross-sections corresponding to $t = 0, 79, 84$, respectively.

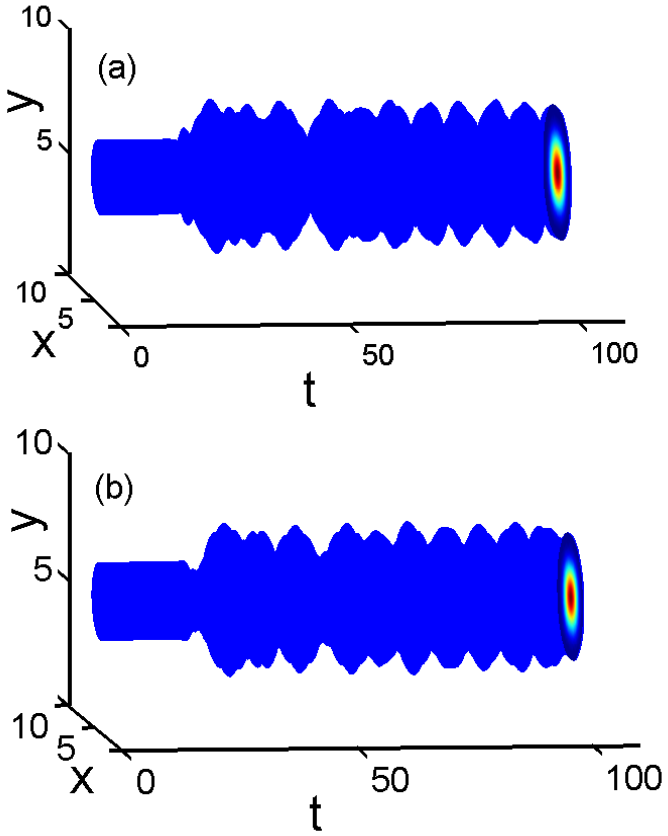

Figure 5.3.6: The plot of evolution of breathers ((a) U (b) V) with time with $\gamma = 0.4, a = 2.0208, \alpha = 0.1$.

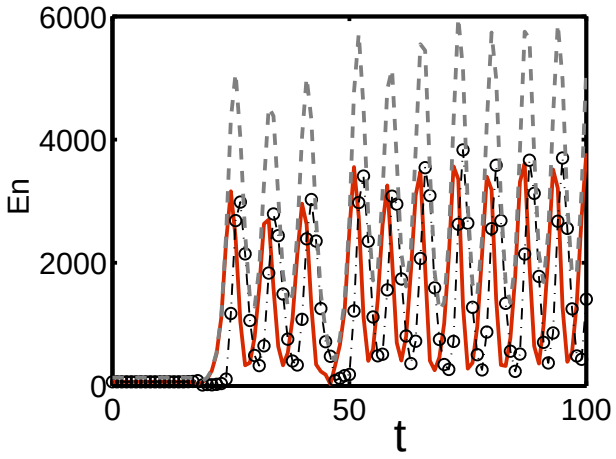

Figure 5.3.7: Dot-dash line with circles and red full line indicate the individual power P_V and P_U , respectively, and the grey dashed line represents the total power P_T. The parameters are same as in Figure 5.3.6.

diffract, and at the same time, the peaks of U and V both decay with time. The total power decreases at a specific point [Figure 5.3.4(b)].

In another scenario, the soliton blows up during the evolution. The star markers in Figure 5.3.1 represent breakup of solitons. The power and peaks of solitons all exponentially grow with time. However, the solitons U and V break up in a symmetric way and the eight small filaments are distributed symmetrically in the last stage (Figure 5.3.5).

In addition, the breakup of the unstable soliton results in the formation of a long-lived breather (Figure 5.3.6). Like the results presented in reference[169] and Figure 5.3.4(b), the component V (mode amplitude in the bottom waveguides with loss) grows and U decreases in the very initial stage ($t = 15 - 19$). Their cross-sections vary with time periodically, but they never go back to initial state. Accordingly, the individual powers and total power show a periodic behavior (Figure 5.3.7).

It is worth mentioning that the cross-section evolves stably in a periodic way (Figure 5.3.2, 5.3.3, 5.3.6), and even after the breakup of solitons, the eight filaments still could propagate periodically in time domain (Figure 5.3.5), which implies that the stable oscillating soliton or breather is a common phenomenon in the system with balanced gain and loss.

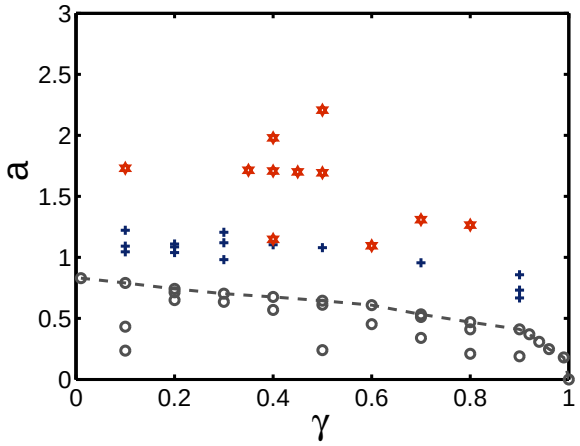

Figure 5.3.8: the dashed curve with circle shows the boundary between the long-lived soliton (eventually diffract, see Figure 5.3.9) and splitting and moving of the soliton. The red stars mark the splitting of the soliton (see Figure 5.3.12) and the plus markers indicate the moving of the soliton (see Figure 5.3.10) in the same direction.

5.3.2 Solitons for $cos\theta < 0$

To verify the predictions based on linear stability analysis, as we addressed above, we carried out numerical simulations of solitons with a range of amplitudes for different gain-loss rate γ. The simulations of the whole γ regime are summarized in Figure 5.3.8. The red stars indicate that the solitons split into two breathers (Figure 5.3.12) and the plus markers represent that the instability of solitons leads to spontaneous motion of the two components U and V in the same direction (Figure 5.3.10).

For one-dimensional case[169, 165] (only with x or y direction), the solitons for $cos\theta > 0$ and $cos\theta < 0$ are both stable for sufficiently small a (below a finite threshold). Although the soliton with $cos\theta < 0$ has unstable eigenvalue (also its real part is exponentially small), the small-amplitude soliton doesn't show any instability within the very long distance[165]. In contrast, in our case (for $cos\theta < 0$), numerically, we found that the U and V components with initial noise both decay eventually. Therefore, the peaks of amplitudes U and V decrease with time and the individual power P_U and P_V and total power P_T oscillates around the position of equilibrium, see Figure 5.3.9(b)(c)(d). On the contrary, Figure 5.3.9(a)(c)(d) shows that, without noise, the soliton is stable

within a very long time, and the peaks and powers keep almost unchanged.

For soliton with $cos\theta < 0$, one of the scenarios of instability is shown in Figure 5.3.10. The solitons start moving at $t \approx 60$ in the same direction, and transforming to breathers, followed by the decay of U and V. Figure 5.3.11 demonstrates that the individual powers and total power oscillate with time, which is similar to variation of power in Figure 5.3.9(d) (the soliton both decay eventually in these two cases).

The other observed instability of solitons is demonstrated in Figure 5.3.12. In this case, with the increase of power (Figure 5.3.13), the solion breaks up into a pair of breathers in order to shake off the extra energy. In particular, in our simulation, these two breathers evolve stably for sufficient long time if one take parameter $0.3 < \gamma < 0.5$.

In addition, it should be emphasized that the long-lived breathers can stay for long time if the gain-loss rate parameter $0.3 < \gamma < 0.5$ for $cos\theta > 0$ and $cos\theta < 0$, which indicates that, to practically observe these instabilities, one should choose γ within this area.

5.3.3 Breakup of one-ring solutions with phase dislocation

Ring bright and dark soliton has drawn a great deal of interest in many branches of physics. For instance, In the context of Bose-Einstein condensates (BEC), The ring dark soliton is first introduced in the repulsive BECs[191]. Ring bright solitons are also observed In a binary BEC experiment[192, 193] and studied further theoretically for different winding number m in the frame of the Gross-Pitaevskii equation[194, 195]. In optics, Ring-like vortex solitons were discovered for several types of nonlinear media[183, 184, 185]. As discussed above, the stability of these solutions has been investigated extensively in conserved systems[170, 185]. Both linear and nonlinear propagation of the beams with phase dislocations and the related angular momentum effects have been a very active research area[170, 185, 196, 197, 198, 199, 200]. For a system with balanced gain and loss, we expect the novel instability of solitons appearing.

As we mentioned before, when $m \neq 0$, the stationary solution with the

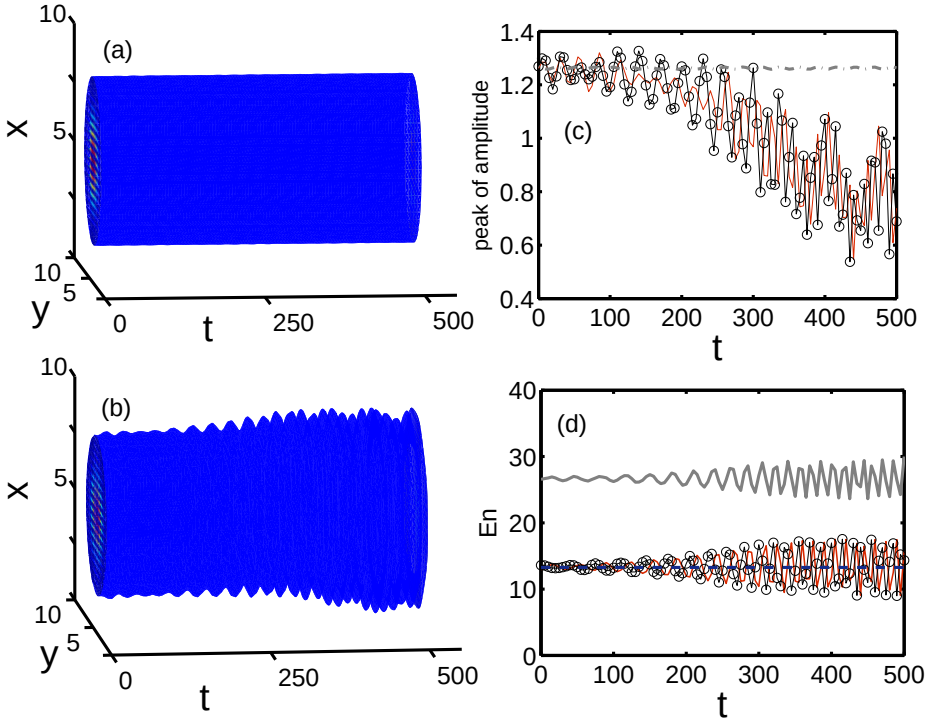

Figure 5.3.9: (a) and (b) show the evolution of cross-sections of one of the components U along the time direction with $\gamma = 0.4, a = 0.5626, \alpha = 0.1, cos\theta < 0$, and initial noise (a) $s = 0$, (b) $s = 0.025$. by adding noise to the initial amplitude and phase, we found that the oscillating soliton can propagate stably for long time and eventually decay or spread everywhere, see (b). (c) Peaks of amplitude U without initial noise (dot-dash curve) and Peaks of amplitudes U and V with $s = 0.025$ (full red curve and full black curve with circles) as function of time t. (d) Horizontal dashed line mark the evolution of power for U without noise with time. Full line with circles and red full line indicate the individual power P_V and P_U , respectively, and the grey full line represents the total power P_T with noise $s = 0.025$.

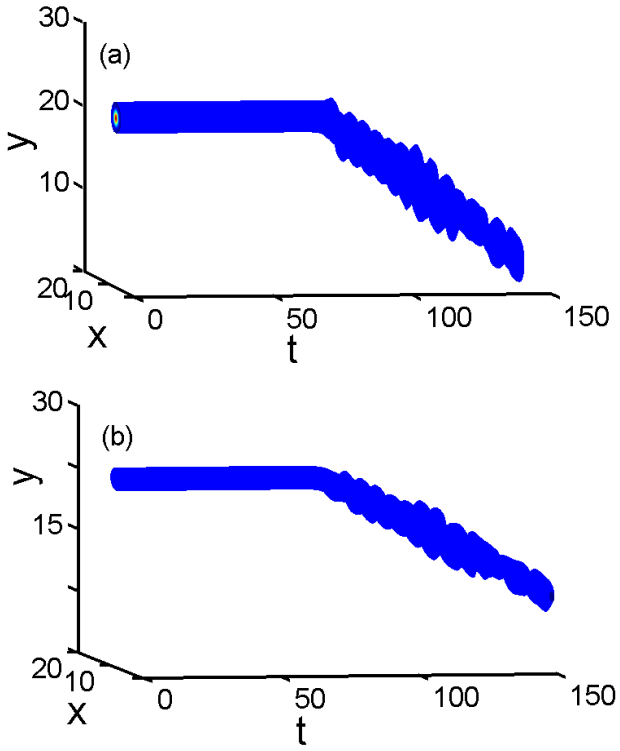

Figure 5.3.10: (a) and (b) show the evolution of cross-sections of the components U and V with time. The two components both move in the same direction and finally decay. The parameters are as follows: $\gamma = 0.1, a = 1.2227, \alpha = 0.1, cos\theta < 0$,

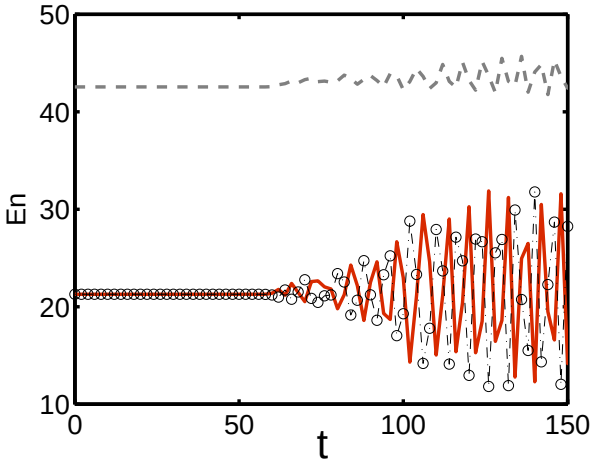

Figure 5.3.11: Dot-dash line with circles and red full line indicate the individual power P_V and P_U , respectively, and the grey dashed line represents the total power P_T. The parameters are same as in Figure 5.3.10.

phase dislocation has been found in the system 5.1.1. It is natural to ask if these solutions are stable. In the case of one-ring solutions, the linear stability analysis shows that the real part of the eigenvalues ν are the real numbers. Therefore, all of the one-ring solutions are not stable. Below, through numerically integrating the equation 5.1.1 by using Fast Fourier Transform for linear part of equation and the fourth-order Runge-Kutta method for nonlinear step, the dynamics of ring-like soliton is studied.

We first simulate the dynamic evolution of the ring soliton with $m = 1$ for $cos\theta > 0$. Figure 5.3.14(a) shows that one-ring soliton breaks up into two breathers. Note that, for large value of a ($a = 1.756$), the transverse velocity of soliton is bigger, see Figure 5.3.14(b). According to the power evolution shown in Figure 5.3.15, when $t \approx 65$, the power increases to a specific value and oscillates again, which indicates that the breather is going to continuously break up. Figure 5.3.16 presents that, after $t = 65$, in order to propagate stably further, one of the breathers split into three breathers, which is able to eliminate the extra energy obtained from the gain medium.

In the case of $cos\theta < 0$, for the ring soliton with $m = 1$, two breathers form in the first stage. After $t \approx 30$, surprisingly, these two breathers break up into four breathers with the decrease of oscillation of power, see Figure 5.3.17. To identify how the value of m influences on the dynamics of soliton,

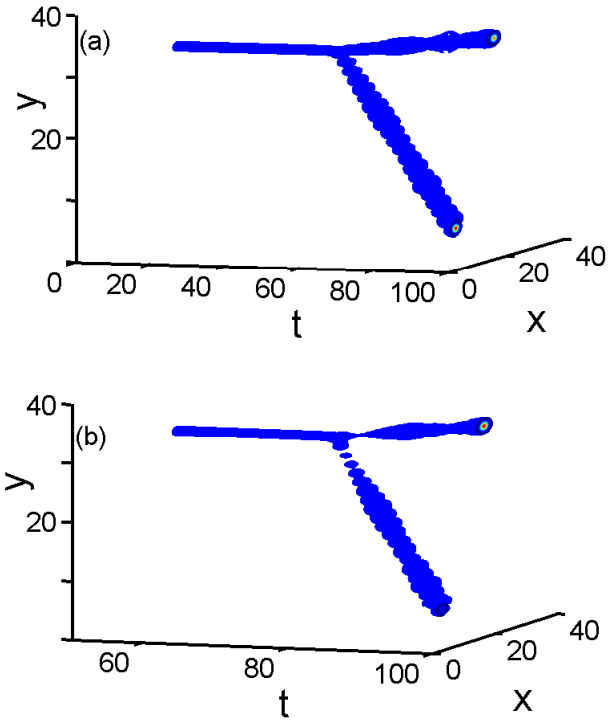

Figure 5.3.12: (a) and (b) show the evolution of cross-sections of the components U and V with time. The two components both split into a pair of breathers. The parameters are as follows: $\gamma = 0.4, a = 1.7078, \alpha = 0.1, cos\theta < 0$,

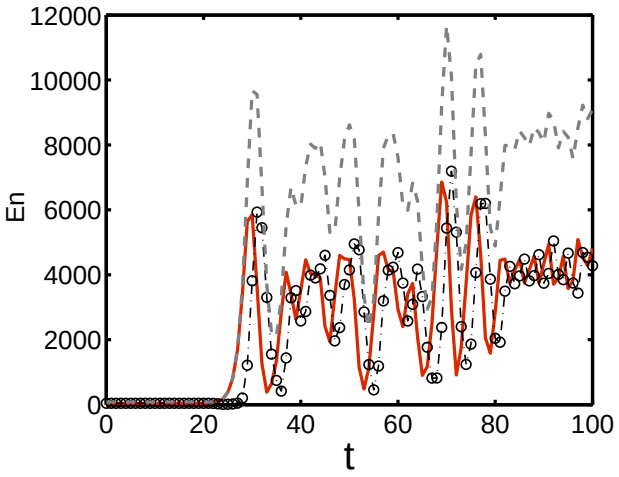

Figure 5.3.13: Dot-dash line with circles and red full line indicate the individual power P_V and P_U , respectively, and the grey dashed line represents the total power P_T. The parameters are same as in Figure 5.3.12.

below, we simulate the evolution of ring soliton with $m = 2$. Similarly, for $cos\theta > 0$, the soliton split into four breathers and one of them disappears at $t \approx 40$. Numerically, we found that these three breathers still stay there after $t = 100$. For $cos\theta < 0$, four breathers form when t reaches to 30 and four breathers further dissociate and become eight breathers, followed by breakup when $t = 55$.

Figure 5.3.18(b) and Figure 5.3.19(b) show the motion trajectories of filaments after the breakup of a ring soliton. Clearly, one can see that the self-trapped filaments travel along the paths tangent to the initial ring.

5.4 Summary

In this chapter, we examined the stability of two families of solitons which are special stationary solution found through equations 5.1.5-5.1.7 in dielectric-metal-dielectric waveguides with balanced gain and loss. The main results can be summarized as follows.

(1) For solitons with $cos\theta > 0$, below the critical values of a, which have been found numerically, the solitons with low and high level noises are stable by numerically testing several cases. Furthermore, for twelve values of

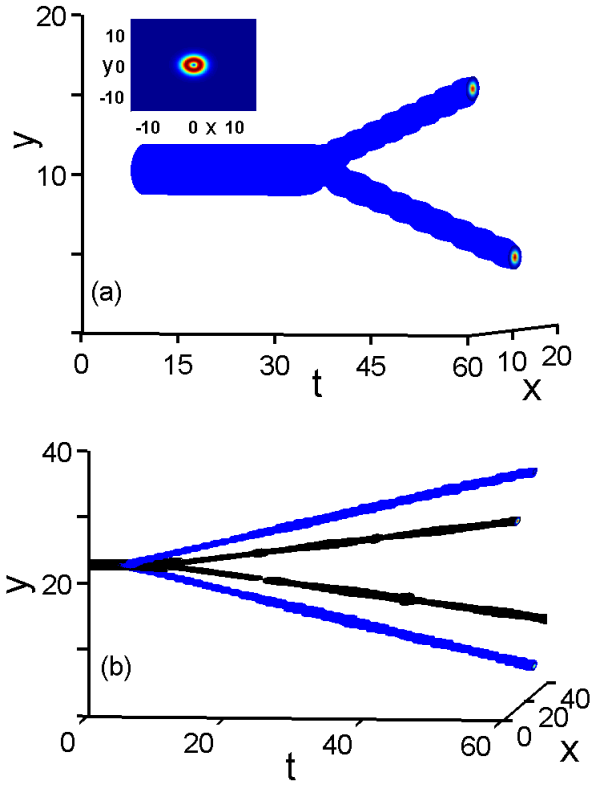

Figure 5.3.14: (a) Breakup of the one-ring solution U with $a = 1.0409$. (b) The evolution of the unstable solution U with $a = 1.0409$ (the black area) and $a = 1.756$ (the blue area). Here $\gamma = 0.4, \alpha = 0.1, m = 1, cos\theta > 0$,

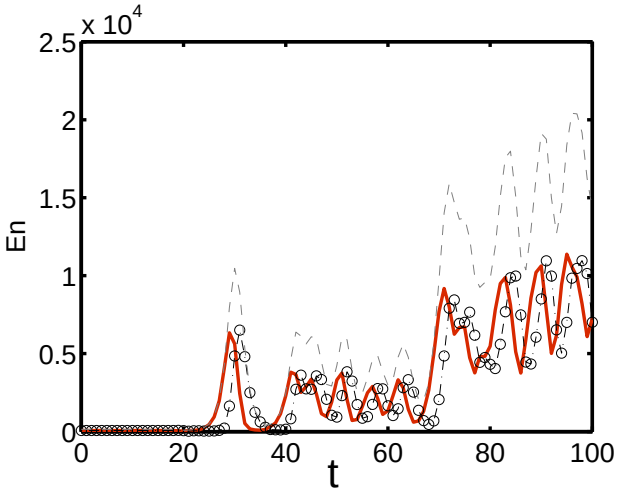

Figure 5.3.15: Dot-dash line with circles and red full line indicate the individual power P_V and P_U , respectively, and the grey dashed line represents the total power P_T. The parameters are same as in Figure 5.3.6.

$\gamma = 0.1, 0.2, 0.3, 0.35, 0.4, 0.45, 0.5, 0.6, 0.7, 0.8, 0.9, 0.99$, we simulated the evolutions of solitons with a above the critical values, and three different scenarios of instability of solitons have been identified. When $0.3 < \gamma < 0.5$, long-lived breathers are formed. On the other hand, the two fields U and V grow with time monotonously and finally break up into several filaments, see Figure 5.3.5. In addition, U and V components both decay with time and spread everywhere, see Figure 5.3.4.

(2) In the case of solitons with $cos\theta < 0$, all solitons are unstable. However, the lifetime of the solitons with small value of a can survive for very long time. Therefore, they can be observed in practice. Also, the splitting and spontaneous moving of solitons have been found.

(3) For the ring solitons with a phase dislocation and $cos\theta > 0$, we identified that , when $m = 1, 2$, the ring solitons break into 2 and 4 filaments in the early stage, respectively, and these filaments move outwards along the tangents to the initial ring. In contrast, in the case of ring solitons with $cos\theta < 0$, for $m = 1$, in the first stage, two filaments are formed and next, these two filaments continue to split into four filaments and finally blow up. For $m = 2$, similar scenario appeared, see Figure 5.3.19.

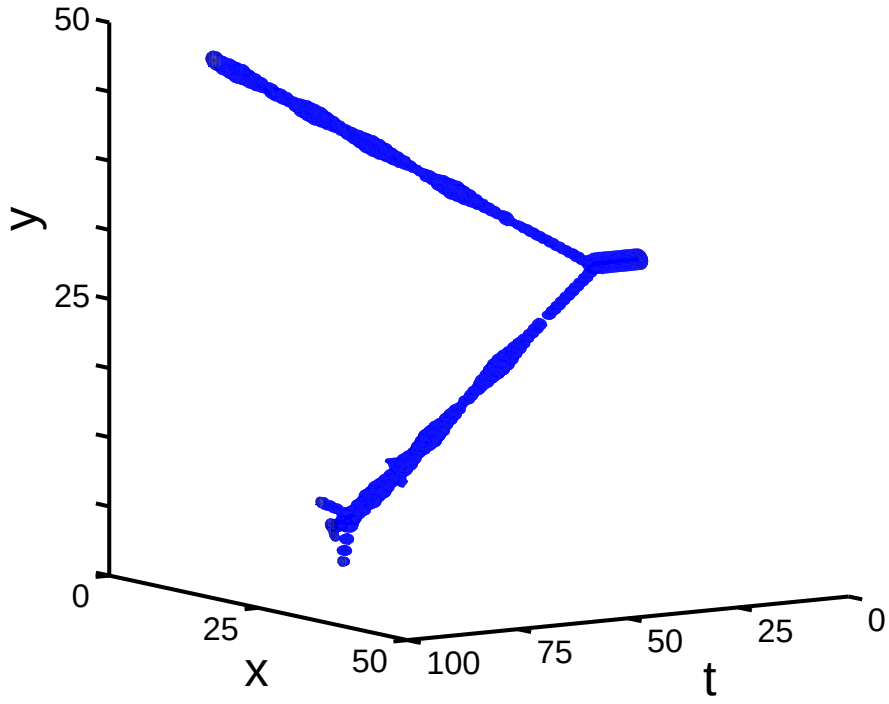

Figure 5.3.16: Breakup of the one-ring solution U with $a = 1.0409$. Here $\gamma = 0.4, \alpha = 0.1, m = 1, cos\theta > 0$,

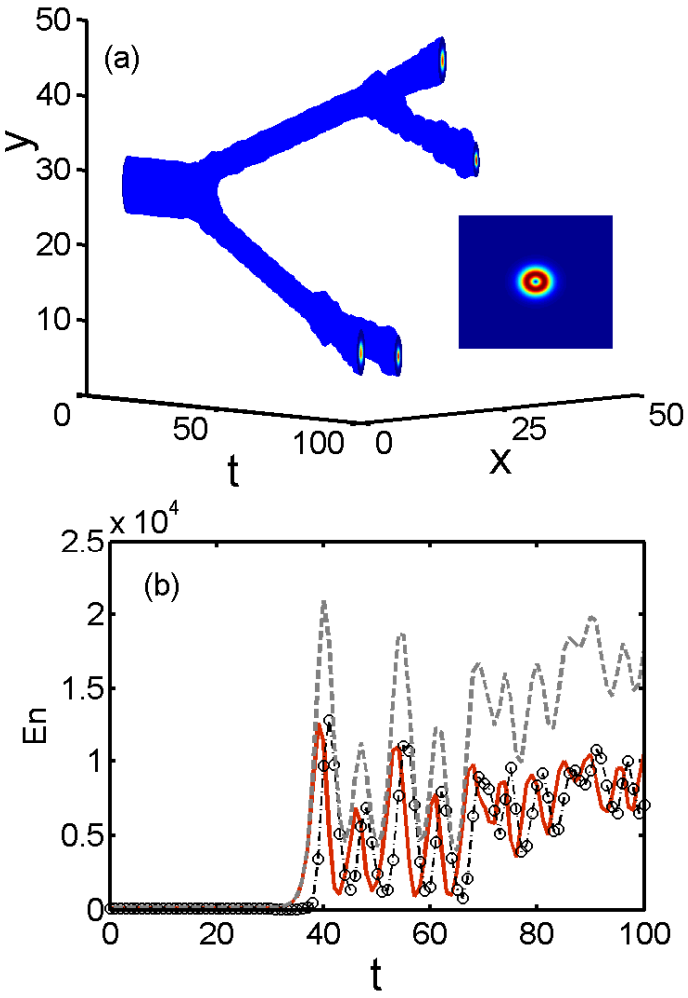

Figure 5.3.17: (a) Breakup of the one-ring solution U with $a = 1.0082$. The inset shows the initial ring soliton. (b) Dot-dash line with circles and red full line indicate the individual power P_V and P_U , respectively, and the grey dashed line represents the total power P_T. Here $\gamma = 0.4, \alpha = 0.1, m = 1, cos\theta < 0$,

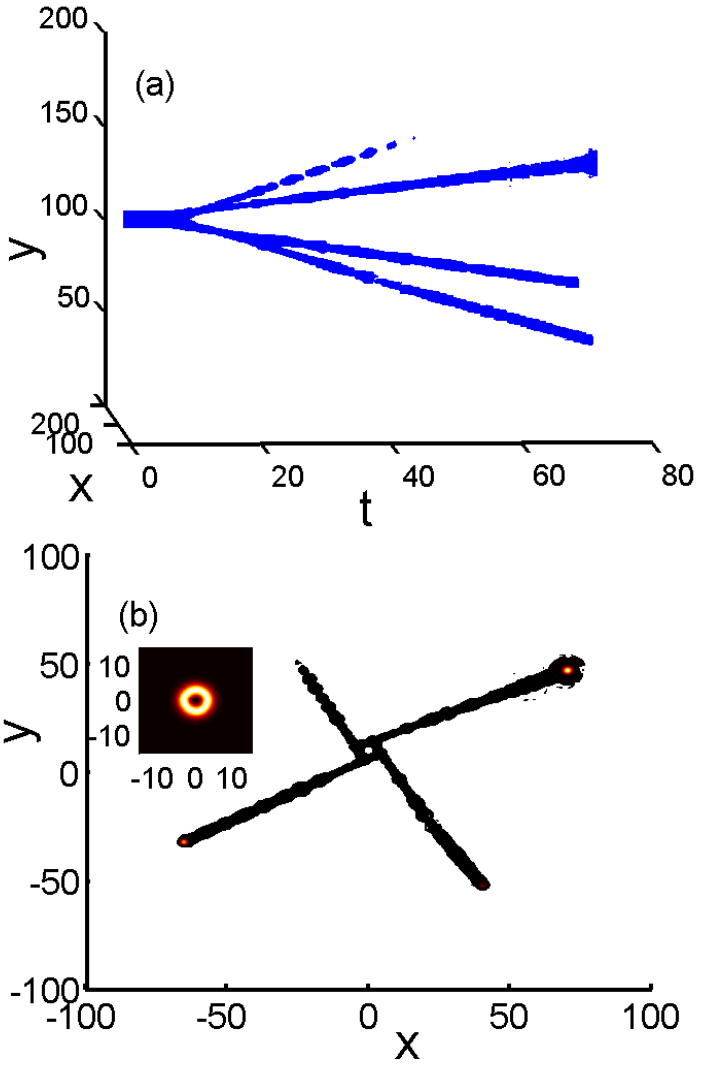

Figure 5.3.18: (a) Breakup of the one-ring solution U with $a = 1.0409$. The inset shows the initial ring soliton. (b) The trajectory of the unstable solution U with $a = 1.0409$. Here $\gamma = 0.4, \alpha = 0.1, m = 2, cos\theta > 0$,

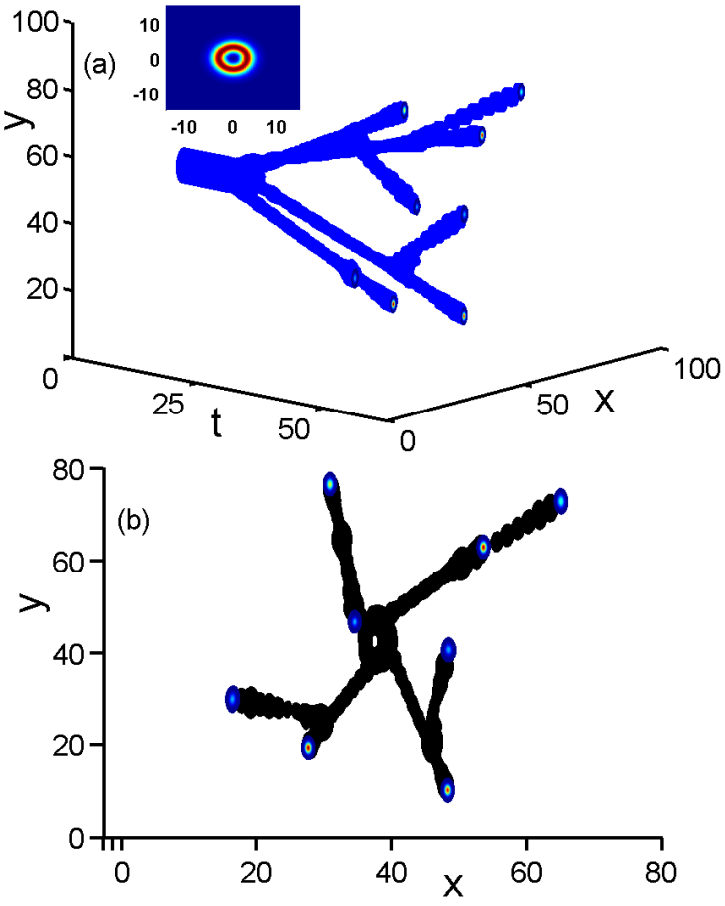

Figure 5.3.19: (a) Breakup of the one-ring solution U with $a = 1.0082$. The inset shows the initial ring soliton. (b) The trajectory of the unstable solution U with $a = 1.0082$. Here $\gamma = 0.4, \alpha = 0.1, m = 2, cos\theta < 0$,

Chapter 6

Conclusions and future work

This chapter provides a summary of findings discussed above and our future work.

We reported new mechanism arising from dispersion of nonlinearity, which is capable of inducing MI in the regime of normal group velocity dispersion, in nano-structured semi-conductor waveguides, and the dynamics of soliton in dielectric-metal-dielectric waveguides with PT symmetry.

We derived a new model with nonlinear dispersion terms governing evolution of the amplitude of the all optical components interacting in a waveguide. In particular, for degenerate FWM, The new MI condition has been found, as we took into account the dispersion of nonlinearity. We demonstrated that this dispersion of nonlinearity can lead to the MI in the range of normal group velocity dispersion for CW. A simple generalization of the NLS equation accounting for the MI resulting from the dispersion of nonlinearity was presented[126]. (*Optics Express*, ***19***, 9345, 2011.)

In chapter 4, by making the assumption of factorization of the four-frequency dependence of nonlinear coefficient, the reduced generalized nonlinear Schrödinger-type equation has been derived. Based on this model, we addressed that the dispersion of nonlinearity in sub-wavelength semiconductor waveguide induces the MI in picsecond regime together with the cascaded generation of higher-order sidebands. The impact of the dispersion of nonlinearity on spectral broadening of short pulses in a silicon waveguide also has been demonstrated[138]. (*J. Opt. Soc. Am. B*, ***30***, 812, 2013.)

We demonstrated the temporal evolutions of fundamental and one-ring

solitary waves with phase dislocation in dielectric-metal-dielectric waveguides with PT-symmetry and numerically analyzed the properties of these nonlinear localized modes and, revealed different scenarios of their instability. (In preparation)

One of our main goals of this thesis is to study the impact of dispersion of nonlinearity on MI in sub-wavelength waveguides. On the other hand, by considering the dispersion of nonlinearity, the nonlinear phenomena in nonastructured waveguides, such as soliton[131], are also under investigation. In particular, while the pump wavelength is close to Zero-GVD point, it is still remaining a challenge whether the dispersion of nonlinearity on its own could compensate for the nonlinearity, thus leading to a soliton.

PT-symmetry, which is a basic and crucial concept for understanding the physics behind many phenomena[148], has been introduced into optics lately as optics offers an ideal platform to implement this functionality[149]. Further investigating the waveguides with PT-symmetry could bring profound understanding about this concept and rich and new phenomena in optics.

List of Figures

Appendix: Numerical Methods

A: Split-step beam propagation method with adaptive step

In our work, we have frequently used Split-step Fourier method to simulate the beam propagation. In this section, the implementation of this method is discussed.

The generalised NLS equation always can be given by:

$$\frac{\partial E}{\partial z} = [\hat{D}(\omega) + \hat{N}(z, \omega)]E, \tag{6.0.1}$$

where $\hat{D}$ is the dispersion operator and $\hat{N}$ is the nonlinear operator.

Without the nonlinear terms (including such as self-steepening term, Raman delayed response, etc..), the equation can be solved in the frequency domain, since the derivative term $\hat{D}$ in the time domain is replaced with a simple multiplication factor. On the contrary, The nonlinear terms are more easily evaluated in the time domain. Split-step Fourier technique can satisfy both requirements. The principle of the Split-step Fourier method is to solve the equation 6.0.1for each small step h. The dispersion operator and the nonlinear operator act independantly for each step h. The dispersive step can be written as:

$$\frac{\partial E_D}{\partial z} = \hat{D}(\omega)E.$$

Its solution in frequency domain is given by:

$$E_D(z+h,\omega) = exp[\hat{D}(\omega)]E_D(z,\omega).$$

On the other hand, the nonlinear step:

$$\frac{\partial E_N}{\partial z} = \hat{N}(\omega)E$$

has been solved by using fourth or fifth-order Runge-Kutta method.

In the process of solving the equation 6.0.1, the pulse propagates from one step h to another repeatedly until the end of the waveguide or fibre is achieved and a Fourier transform and an inverse Fourier transform are performed at each step h. Note that a fast Fourier transform (FFT) algorithm is used.

It should be mentioned that, in the nonlinear step, Runge-Kutta method with adaptive step[201] has been employed in order to reduce the numerical error. Adaptive stepsize algorithm invented by Fehlberg is base on the embedded Runge-Kutta formulars. For simplicity, the general form of a fifth-order Runge-Kutta formula is directly given by:

$$k_1 = hf(x_n, y_n),$$

$$k_2 = hf(x_n + a_2 h, y_n + b_{21}k_1),$$

$$\cdots$$

$$k_6 = hf(x_n + a_{26}h, y_n + b_{61}k_1 + \cdots + b_{65}k_5),$$

$$y_{n+1} = y_n + c_1k_1 + c_2k_2 + c_3k_3 + c_4k_4 + c_5k_5 + c_6k_6 + o(h^6). \qquad (6.0.2)$$

The embedded fourth-order foumula is given by:

$$y^*_{n+1} = y_n + c^*_1 k_1 + c^*_2 k_2 + c^*_3 k_3 + c^*_4 k_4 + c^*_5 k_5 + c^*_6 k_6 + o(h^5). \qquad (6.0.3)$$

The values of the constants appearing in equations 6.0.2 and 6.0.3 are given in reference [201]. The error estimate is:

$$\Delta = y_{n+1} - y^*_{n+1}.$$

We define Δ_0 as the desired accuracy and take a step $h_1$and produce an error Δ_1. If Δ_1 is larger than Δ_0 in magnitude, then the stepsize must be reduced. If Δ_1 is smaller than Δ_0, then we can increase the stepsize for the next step.

B: Newton method

Newton's method, which also is called Newton-Raphson method, is widely employed to solve the nonlinear equations. The idea of the method is that the function is approximated by its tangent line at a current point x_i, and until it crosses zero, one computes the abscissa of this tangent line. This x-intercept will be a better approximation to the function's root than the original guess. This method employs the familiar Taylor series expansion of a function. Typically, the function involves N variables $x_i, i = 1, 2 \cdots N$, and is given by:

$$f_i(x_1, x_2, \cdots x_N) = 0, i = 1, 2, \cdots N.$$

Each of the functions f_i can be expanded in Taylor series:

$$f_i(X + \delta X) = f_i(X) + \sum_{j=1}^{N} \frac{\partial f_i}{\partial x_j} \delta x_j + O(\delta X^2), \qquad (6.0.4)$$

where X denotes the entire vector of values $x_i$and F denote the entire vector of functions f_i.

We define the matrix of partial derivatives as the Jacobian matrix J:

$$J_{ij} = \frac{\partial f_i}{\partial x_j}.$$

The equation 6.0.4 can be written as:

$$F(X + \delta X) = F(X) + J{\cdot}\delta X + O(\delta X^2).$$

By neglecting second-order term together with higher order terms in the right hand side and by setting $F(X + \delta X) = 0$, we obtain a set of linear equations for the corrections δX :

$$J{\cdot}\delta X = -F(X).$$

The corrections are added to the solution vector:

$$X^{new} = X^{old} + \delta X$$

It should be noted that the convergence strongly depends on the initial guess. Therefore, the method will converge quickly provided this initial guess is close enough to root.

Bibliography

[1] G. P. Agrawal, Nonlinear Fiber Optics, 4th ed. (Academic Press, Boston, 2007)

[2] A. W. Snyder and J. Love, Optical Waveguide Theory (Kluwer, Boston, 1983)

[3] R. W. Boyd. (2002). Nonlinear optics (2nd ed.).

[4] Pochi Yeh, Optical Waves in Layered Media, (Wiley, 1988).

[5] Y, S. Kivshar, G. P. Agrawal, Optical Solitons, (Academic Press, 2003).

[6] D J Frantzeskakis, "Dark solitons in atomic Bose–Einstein condensates: from theory to experiments", *J. Phys. A: Math. Theor.* 43, 213001(2010).

[7] T. Taniuti and H. Washimi, "Self-Trapping and Instability of Hydromagnetic Waves Along the Magnetic Field in a Cold Plasma", *Phys. Rev. Lett.* 21, 209 (1968)

[8] E.A. Kuznetsov and A.M. Rubenchik, "Soliton stability in plasmas and hydrodynamics", *PHYSICS REPORTS* (Review Section of Physics Letters) 142, 103-165(1986).

[9] Zabusky, N. J. and Kruskal, M. D. "Interaction of 'solitons' in a collisionless plasma and the recurrence of initial states", *Phys. Rev. Lett.* 15 (6): 240–243 (1965).

[10] J.Scott Russell, Report of 14th Meeting of the British Association for Advancement of Science, York, September 1844, pp. 311-390.

[11] C. S. Gardner, J.M.Green, M.D. Kruskal, and R. M. Miura, *Phys. Rev. Lett.* 19, 1095 (1967);

[12] Akira Hasegawa and Frederick Tappert, "Transmission of stationary nonlinear optical pulses in dispersive dielectric fibers. i. anomalous dispersion", *Applied Physics Letters*, 23,142 (1973).

[13] L. F. Mollenauer and R. H. Stolen, "Experimental observation of picosecond pulse narrowing and solitons in optical fibers", *Phys. Rev. Lett.*, 45,1095–1098, 1980.

[14] H.Hasegawa and Y. Kodama, Solitons in Optical Communications (Oxford University Press, New York, 1995);

[15] H.A. Haus and W. S. Wong, *Rev. Mod. Phys.* 68, 423 (1996);

[16] G. P. Agrawal, Applications of Nonlinear Fiber Optics (Acdemic Press, San Diego, CA, 2001);

[17] Hermann A. Haus and William S. Wong, "Solitons in optical communications", *Review of Modern Physics*, 68, 423–444, 1996.

[18] J.C.Knight, T.A.Birks, J.C.Knights, and P.St.J.Russell, *Opt. Lett.* 21,1547(1996).

[19] P.St.J.Russell,*Science* 299, 358 (2003).

[20] W.J. Wadsworth, J.C. Knight, A. Ortigosa-Blanch, J. Arriaga, E. Silvestre, and P.St.J. Russell, "Soliton effects in photonic crystal fibres at 850 nm", *Electronics Letters*, 36, 53–55, 2000.

[21] Q. Lin, J. Zhang, G. Piredda, R. W. Boyd, P. M. Fauchet, and G. P. Agrawal, "Dispersion of silicon nonlinearities in the near infrared region", *Applied Physics Letters*, 91, 021111, 2007.

[22] J. Zhang, Q. Lin, G. Piredda, R. W. Boyd, G. P. Agrawal, and P. M. Fauchet, "Optical solitons in a silicon waveguide," *Optics Express* 15, 7682–7688 (2007).

[23] Alan D. Bristow, Nir Rotenberg, and Henry M. van Driel, "Two-photon absorption and kerr coefficients of silicon for 850 2200 nm", *Applied Physics Letters*, 90, 191104, 2007.

[24] C. Koos, L. Jacome, C. Poulton, J. Leuthold, and W. Freude, "Nonlinear silicon-on-insulator waveguides for all-optical signal processing", *Optics Express*, 15:5976–5990, 1997.

[25] I-Wei Hsieh, Xiaogang Chen, Jerry I. Dadap, Nicolae C. Panoiu, and Richard M. Osgood, "Ultrafast-pulse self-phase modulation and third-order dispersion in Si photonic wire-waveguides" *Optics Express*, 14, 12380–12387, 2006.

[26] Amy C. Turner, Christina Manolatou, Bradley S. Schmidt, Michal Lipson, Mark A. Foster, Jay E. Sharping, and Alexander L. Gaeta, "Tailored anomalous group-velocity dispersion in silicon channel waveguides", *Optics Express*, 14:4357–4362, 2006.

[27] Eric Dulkeith, Fengnian Xia, Laurent Schares, William M. J. Green, and Yurii A. Vlasov, "Group index and group velocity dispersion in silicon-on-insulator photonic wires", *Optics Express*, 14:3853–3863, 2006.

[28] Mark A. Foster, Amy C. Turner, Michal Lipson, and Alexander L.Gaeta, "Nonlinear optics in photonic nanowires", *Opt. Lett.* 16, 1300–1320 (2008).

[29] George I. Stegeman and Mordechai Segev, "Optical Spatial Solitons and Their Interactions: Universality and Diversity", *Science*, 286 , 1518-1523, 1999.

[30] R. Y. Chiao, E. Garmire, and C. H. Townes, "Self-trapping of optical beams", *Phys. Rev. Lett.*, 13, 479-482, (1964).

[31] A. Barthelemy, S. Maneuf and C. Froehly, "soliton propagation and self-confinement of laser-beams by Kerr optical nonlinearity", *Optics Communications*, 55, 201-206(1985).

[32] Y. Siberberg and G. I. Stegman, In Spatial Solitons, S. Trillo and W. Torruellas, Eds. (Springer, New York,2001).

[33] D. N. Christodoulides, R. I. Joseph, "Discrete self-focusing in nonlinear arrays of coupled waveguides", *Opt. Lett.*, 13, 794-796 (1988).

[34] H. S. Eisenberg and Y. Silberberg, R. Morandotti, A. R. Boyd, and J. S. Aitchison, "Discrete Spatial Optical Solitons in Waveguide Arrays", *Phys. Rev. Lett.*, 81, 3383-3386 (1998).

[35] R. Morandotti, U. Peschel, and J. S. Aitchison, H. S. Eisenberg and Y. Silberberg, "Dynamics of Discrete Solitons in Optical Waveguide Arrays", *Phys. Rev. Lett.*, 83, 2726-2729 (1999).

[36] G. A. Swartzlander, Jr., D. R. Andersen, J. J. Regan, H. Yin and A. E. Kaplan, *Phys. Rev. Lett.* 66,1583 (1991).

[37] G. R. Allan, S. R. Skinner, D. R. Andersen, and A. L. Smirl, *Opt. Lett.* 16, 156 (1991).

[38] Shvedov, V. G., Rode, A. V., Izdebskaya, Y. V., Desyatnikov, A. S., Krolikowski, W., & Kivshar, Y. S., "Giant Optical Manipulation", *Phys. Rev. Lett.*105, 118103 (2010).

[39] Dholakia, K., and Čižmár, T., "Shaping the future of manipulation", *Nature Photonics*, 5(6), 335–342 (2011).

[40] Padgett, M., and Bowman, R., "Tweezers with a twist", *Nature Photonics*, 5(6), 343–348, (2011).

[41] Allen, L., Beijersbergen, M. W., Spreeuw, R. J. C. & Woerdman, J. P., "Orbital angular-momentum of light and the transformation of Laguerre–Gaussian laser modes", *Phys. Rev. A* 45, 8185–8189 (1992).

[42] He, H., Friese, M., Heckenberg, N. R. & Rubinsztein-Dunlop, H., "Direct observation of transfer of angular momentum to absorptive particles from a laser beam with a phase singularity", *Phys. Rev. Lett.* 75, 826–829 (1995).

[43] V. I. Kruglov and R. A. Vlasov, *Phys. Rev. A* 111,401 (1985).

[44] G. T. Reed and A. P. Knights, Silicon Photonics: An Introduction (Wiley, Hoboken, NJ, 2004)

[45] R. A. Soref, "The Past, Present, and Future of Silicon Photonics," *IEEE J. Sel. Top.Quantum Electron.* 12, 1678–1687 (2006).

[46] R. A. Soref, S. J. Emelett, and W. R. Buchwald, "Silicon waveguided components for the long-wave infrared region," *J. Opt. A: Pure Appl. Opt.* 8, 840–848 (2006).

[47] J. S. Aitchison, D. C. Hutchings, , J. U. Kang. G .I. Stegeman, A. Villeneuve, "The nonlinear optical properties of AlGaAs at the half band gap," *IEEE Journal of Quantum Electronics*, 33(3), 341-348 (1997).

[48] G. I. Stegeman, A. Villeneuve, J. Kang, J. S. Aitchison, C. N. Ironside, K. Alhemyari, C. C. Yang, C. H. Lin, H. H. Lin, G. T. Kennedy, R. S. Grant, and W. Sibbett, "AlGaAs Below Half Bandgap - the Silicon of Nonlinear-Optical Materials," *Int. J. Nonlinear Opt. Phys.* 3, 347-371 (1994).

[49] Q. Lin, J. Zhang, G. Piredda, R. W. Boyd, P. M. Fauchet, and G. P. Agrawal, "Dispersion of silicon nonlinearities in the near infrared region," *Appl. Phys. Lett.* 91, 21111 (2007).

[50] Meier, J., Mohammed, W. S., Jugessur, A, Qian, L., Mojahedi, M., & Aitchison, J. S., "Group velocity inversion in AlGaAs nanowires", *Optics Express*, 15(20), 12755–12762. (2007).

[51] J.Leuthold, C. Koos and W. Freude. "Nonlinear silicon photonics", *Nature Photonics*, 4, 535-544 (2010).

[52] H. K. Tsang, C. S. Wong, T. K. Liang, I. E. Day, S. W. Roberts, A. Harpin, J. Drake, and M. Asghari, "Optical dispersion, two-photon absorption, and self-phase modulation in silicon waveguides at 1.5μm wavelength," *Appl. Phys. Lett.* 80, 416–418 (2002).

[53] E. Dulkeith, Y. A. Vlasov, X. Chen, N. C. Panoiu, and R. M. Osgood, Jr., "Self-phase-modulation in submicron silicon-on-insulator photonic wires," *Opt. Express* 14, 5524–5534 (2006).

[54] L. Yin and G. P. Agrawal, "Impact of two-photon absorption on self-phase modulation in silicon waveguides," *Opt. Lett.* 32, 2031–2033 (2007).

[55] I-W. Hsieh, X. Chen, J. I. Dadap, N. C. Panoiu, R. M. Osgood, Jr., S. J. McNab, and Y. A. Vlasov, "Cross phase modulation-induced spectral and temporal effects on co-propagating femtosecond pulses in silicon photonic wires," *Opt. Express* 15, 1135–1146 (2007).

[56] A. Hache and M. Bourgeois, "Ultrafast all-optical switching in a silicon-based photonic crystal," *Appl. Phys. Lett.* 77, 4089–4091 (2000).

[57] J. I. Dadap, R. L. Espinola, R. M. Osgood, Jr., S. J. McNab, and Y. A. Vlasov, "Spontaneous Raman scattering in ultrasmall silicon waveguides," *Opt. Lett.* 29, 2755–2757 (2004).

[58] V. Raghunathan, D. Borlaug, R. R. Rice, and B. Jalali, "Demonstration of a mid-infrared silicon Raman amplifier," *Opt. Express* 15, 14355–14362 (2007).

[59] R. Claps, D. Dimitropoulos, Y. Han, and B. Jalali, "Observation of Raman emission in silicon waveguide at 1.54μm," *Opt. Express* 10, 1305–1313 (2002).

[60] M. A. Foster, A. C. Turner, J. E. Sharping, B. S. Schmidt, M. Lipson, and A. L. Gaeta, "Broad-band optical parametric gain on a silicon photonic chip," *Nature* 441, 960–963 (2006).

[61] D. Dimitropoulos, V. Raghunathan, R. Claps, and B. Jalali, "Phase-matching and nonlinear optical processes in silicon waveguides," Opt. Express 12, 149–160 (2003).

[62] V. Raghunathan, R. Claps, D. Dimitropoulos, and B. Jalali, "Wavelength conversion in silicon using Raman induced four-wave mixing," *Appl. Phys. Lett.* 85, 34–26 (2004).

[63] R. L. Espinola, J. I, Dadap, R. M. Osgood, Jr., S. J. McNab, and Y. A. Vlasov, "C-band wavelength conversion in silicon photonic wire waveguides," *Opt. Express* 13, 4341–4349 (2005).

[64] H. Fukuda, K. Yamada, T. Shoji, M. Takahashi, T. Tsuchizawa, T. Watanabe, J. Takahashi, and S. Itabashi,"Four-wave mixing in silicon wire waveguides," *Opt. Express* 13, 4629–4637 (2005).

[65] V. Raghunathan, R. Claps, D. Dimitropoulos, and B. Jalali, "Parametric Raman wavelength conversion in scaled silicon waveguides," *IEEE J. Light wave Technol.* 23, 2094–2102 (2005).

[66] H. Rong, Y. Kuo, A. Liu, M. Paniccia, and O. Cohen, "High efficiency wavelength conversion of 10 Gb/s data in silicon waveguides," *Opt. Express* 14, 1182–1188 (2006).

[67] Q. Lin, J. Zhang, P. M. Fauchet, and G. P. Agrawal, "Ultrabroadband parametric generation and wavelength conversion in silicon waveguides," *Opt. Express* 14, 4786–4799 (2006).

[68] K. Yamada, H. Fukuda, T. Tsuchizawa, T. Watanabe, T. Shoji, and S. Itabashi, "All-optical efficient wavelength conversion using silicon photonic wire waveguide," *IEEE Photon. Technol. Lett.* 18, 1046–1048 (2006).

[69] Y. Kuo, H. Rong, V. Sih, S. Xu, M. Paniccia, and O. Cohen, "Demonstration of wavelength conversion at 40 Gb/s data rate in silicon waveguides," *Opt. Express* 14, 11721–11726 (2006).

[70] N. C. Panoiu, X. Chen, and R. M. Osgood, Jr., "Modulation instability in silicon photonic nanowires," *Opt. Lett.* 31, 3609–3611 (2006).

[71] M. A. Foster, A. C. Turner, R. Salem, M. Lipson, and A. L. Gaeta, "Broad-band continuous-wave parametric wavelength conversion in silicon nanowaveguides," *Opt. Express* 15, 12949–12958 (2007).

[72] Qianfan Xu, Vilson R. Almeida, Roberto R. Panepucci, and Michal Lipson, "Experimental demonstration of guiding and confining light in nanometer-size low-refractive-index material", *Opt. Lett.* 29,1209-1211 (2004)

[73] Vilson R. Almeida, Qianfan Xu, Carlos A. Barrios, and Michal Lipson, "Guiding and confining light in void nanostructure", *Opt. Lett.* 29,1626-1628 (2004).

[74] M. Santagiustina, C. G. Someda, G. Vadal'a, S. Combri´e, A. De Rossi, "Theory of slow light enhanced four-wave mixing in photonic crystal waveguides", *Opt. Express* 18, 21024–21029 (2010).

[75] M. Ebnali-Heidari, C. Monat, C. Grillet, M. K Moravvej-Farshi, "A proposal for enhancing four-wave mixing in slow light engineered photonic crystal waveguides and its application to optical regeneration", *Opt. Express* 17, 18340–18353 (2009).

[76] Corcoran, B. et al. "Green light emission in silicon through slow-light enhanced third-harmonic generation in photonic crystal waveguides", *Nature Photon* 3, 206–210 (2009).

[77] B. Corcoran, C. Monat, M. Pelusi, C. Grillet, T. P. White, L. O'Faolain,T. F. Krauss, B. J. Eggleton1 and D. J. Moss, "Optical signal processing on a silicon chip at 640Gb/s using slow-light", *Opt. Express* ,18,7770-7781(2010).

[78] William L. Barnes, Alain Dereux and Thomas W. Ebbesen, "Surface plasmon subwavelength optics", *Nature* 424, 824-830 (2003).

[79] Noh, H., Chong, Y., Stone, a. D., & Cao, H., "Perfect coupling of light to surface plasmons by coherent absorption", *Phys. Rev. Lett.*, 108, 186805 (2012).

[80] Kauranen, M., & Zayats, A. V., Nonlinear plasmonics, 6, 737–748 (2012).

[81] Juan, M. L., Righini, M., and Quidant, R, "Plasmon nano-optical tweezers", *Nature Photonics*, 5, 349–356 (2011).

[82] Berini, P., and Leon, D, "Surface plasmon–polariton amplifiers and lasers", *Nature Photonics*, 1–9 (2011).

[83] Grigorenko, A. N., Polini, M., and Novoselov, K. S., "Graphene plasmonics", *Nature Photonics*, 6, 749-758 (2012).

[84] Cho, C., Aspetti, C. O., Park, J., and Agarwal, R., "Silicon coupled with plasmon nanocavities generates bright visible hot luminescence", *Nature Photonics*, 1–5 (2013).

[85] A. Taflove and S. C. Hagness, Computational Electrodynamics, 3rd ed. (Artech House, London, 2005).

[86] S. Afshar V and T. M. Monro, "A full vectorial model for pulse propagation in emerging waveguides with subwavelength structures part I: Kerr nonlinearity," *Opt. Express* 17, 2298–2318 (2009).

[87] T. X. Tran and F. Biancalana, "An accurate envelope equation for light propagation in photonic nanowires: new nonlinear effects," *Opt. Express* 17, 17934–17949 (2009).

[88] Q. Lin, O. J. Painter, and G. P. Agrawal, "Nonlinear optical phenomena in silicon waveguides: modeling and applications," *Opt. Express* 15, 16604 (2007).

[89] David F. Edwards. Handbook of Optical Constants of Solids, chapter Silicon (Si), page 547. Academic Press, 1985.

[90] R. M. Osgood, Jr., N. C. Panoiu,2 J. I. Dadap, Xiaoping Liu, Xiaogang Chen,1 I-Wei Hsieh, E. Dulkeith, W. M. J. Green, and Y. A. Vlasov, "Engineering nonlinearities in nanoscale optical systems: physics andapplications in dispersion-engineered silicon nanophotonic wires", *Advances in Optics and Photonics* 1, 162–235 (2009).

[91] S. Gehrsitz,et al, *Journal of Applied Physics* 87, 7825-7837 (2000). Sadao Adachi, *J. Appl. Phys.* 58(3), (1985).

[92] W. S. Rodney, I. H. Malitson, and T. A. King, "Refractive index of arsenic trisulfide," *J. Opt. Soc. Am.* 48(9), 633–636 (1958).

[93] F.Biancalana, D.V.Skryabin, P.St.J. Russell, "Four-wave mixing instabilities in photonic-crystal and tapered fibers," *Phys. Rev. E* 68, 046603(2003).

[94] F. Biancalana and D. V. Skryabin, "Vector modulational instabilities in ultra-small core optical fibres", *J. Opt. A* 6,301 (2004)

[95] T. A. Birks, W. J.Wadsworth, and P. St. J. Russell, "Supercontinuum generation in tapered fibers," *Opt. Lett.* 25,1415–1416 (2000).

[96] Michael R.E. Lamont, Boris T. Kuhlmey, and C. Martijn de Sterke, "Multi-order dispersion engineering for optimal four-wave mixing", *Opt. Express* 16, 7551–7563 (2008).

[97] Sara Mas, José Caraquitena, José V. Galán, Pablo Sanchis, and Javier Mart,"Tailoring the dispersion behavior of silicon nanophotonic slot waveguides", *Opt. Express* 18, 20839-20844 (2010).

[98] Lin Zhang,Yang Yue, Raymond G. Beausoleil, and Alan E. Willner, "Flattened dispersion in silicon slot waveguides", *Opt. Express* 18, 20529-20534 (2010).

[99] Lin Zhang, Yang Yue, Yinying Xiao-Li Jian Wang, Raymond G. Beausoleil, and Alan E. Willne, "Flat and low dispersion in highly nonlinear slot waveguide". *Opt. Express* 18, 13187-13193 (2010).

[100] G. B. Whitham, *Proc. Roy. Soc.* 283, 238 (1965); T. B. Benjamin and J. E. Feir, *J.Fluid Mech.* 27, 417 (1967).

[101] V. I. Bespalov and V. I. Talanov, *JETP Lett.* 3, 307 (1966).

[102] C. K. W. Tam, *Phys. Fluids* 12, 1028 (1969).

[103] A. Hasegawa, *Phys. Rev. Lett.* 24, 1165 (1970); *Phys. Fluids* 15, 870 (1971).

[104] M.Yu, C.J.Mckinstrie, Govind P.Agrawal, *Phys. Rev. E* 52, 1072(1995).

[105] M. Kolesik and J. V. Moloney, "Nonlinear optical pulse propagation simulation: From Maxwell's to unidirectional equations," *Phys. Rev. E* 70, 036604 (2004);

[106] 125. D. J. Moss, E. Ghahramani, J. E. Sipe, and H. M. van Driel, "Band-structure calculation of dispersion and anisotropy in χ (3) for third-harmonic generation in Si, Ge, and GaAs," *Phys. Rev. B* 41, 1542–1560 (1990).

[107] 124. C. C. Wang, J. Bomback, W. T. Donlon, C. R. Huo, and J. V. James, "Optical third-harmonic generation in reflection from crystalline and amorphous samples of silicon," *Phys. Rev. Lett.* 57, 1647–1650 (1986)

[108] W. K. Burns and N. Bloembergen, "Third-harmonic generation in absorbing media of cubic or isotropic symmetry," *Phys. Rev. B* 4, 3437–3450 (1971).

[109] M. Kolesik, E. M. Wright, and J. V. Moloney, "Simulation of femtosecond pulse propagation in sub-micron diameter tapered fibers," *Appl. Phys. B* 79, 293–300 (2004).

[110] A. V. Gorbach and D. V. Skryabin, "Spatial solitons in periodic nanostructures," *Phys. Rev. A* 79, 053812 (2009).

[111] N. C. Panoiu, X. P. Liu, and R. M. Osgood, Jr., "Self-steepening of ultrashort pulses in silicon photonic nanowires," *Opt. Lett.* 34, 947–949 (2009).

[112] A. V. Gorbach, W. Ding, O. K. Staines, C. E. de Nobriga, G. D. Hobbs, W. J. Wadsworth, J. C. Knight, D. V. Skryabin, A. Samarelli, M. Sorel, and R. M. De La Rue, "Spatiotemporal nonlinear optics in arrays of subwavelength waveguides," *Phys. Rev. A* 82, 041802 (2010).

[113] R.H.Stolen, J.E.Bjorkholm, and A.Ashkin, *Appl. Phys. Lett.* 24, 308(1974).

[114] R.H.Stolen, J.E.Bjorkholm, *IEEE J. Quantum Electron.* 18, 1062(1982).

[115] G. P. Agrawal, Lightwave Technology: Components and Divices, (Wiley, Hoboken, NJ, 2004).

[116] J.H.Lee,Z.Yusoff, W.Belardi, M.Ibsen, T.M. Monro, and D.J.Richardson, *Opt. Lett.* 27,927 (2002).

[117] T.A.Birks, W.J.Wadsworth, and P.St.J.Russell, *Opt. Lett.* 25,1415 (2000).

[118] Alessia Pasquazi, Yongwoo Park, Jose Azana, Francois Legare, Roberto Morandotti, Brent E. Little, Sai T. chu, and David J. Moss, "Efficient wavelength conversion and net parametric gain via four wave mixing in a high index doped silica waveguide.", *Opt. Express* 18, 7634-7641(2010).

[119] W. Wadsworth, N. Joly, J. Kinght, T. Birks, F. Biancalana, and P. St. J. Russell, *Opt. Express* 12,299 (2004).

[120] W. H. Reeves, D. V. Skryabin, F. Biancalana, J. C. Knight, P. St. J. Russell, F. G. Omenetto, A. Efimov, A. J. Taylor. "Transformation and control of ultra-short pulses in dispersion-engineered photonic crystal fibres". *Nature*, 424:511-515,2003.

[121] M. A. Foster, A. C. Turner, J. E. Sharping, B. S. Schmidt, M. Lipson, and A. L.Gaeta, "Broad-band optical parametric gain on a silicon photonic chip," *Nature* 441, 960–963 (2006).

[122] Espinola, R. L., Dadap, J. I., Osgood, R. M. Jr, McNab, S. J. & Vlasov, Y. A.," Raman amplification in ultrasmall silicon-on-insulator wire waveguides", *Opt. Express* 12, 3713–-3718 (2004).

[123] Michael Galili, Jing Xu, Hans C.H. Mulvad, Leif K. Oxenløwe,Anders T. Clausen, Palle Jeppesen, Barry Luther-Davies, Steve Madden, Andrei Rode, Duk-Yong Choi, Mark Pelusi, Feng Luan, and Benjamin J. Eggleton, "Breakthrough switching speed with an all-optical chalcogenide glass chip: 640 Gbit/s demultiplexing". *Optics Express* 17,2182 (2009).

[124] Xiaoping Liu, Richard M. Osgood Jr, Yurii A. Vlasov and William M. J. Green, "Mid-infrared optical parametric amplifier using silicon nanophotonic waveguides", *nature photonics*, 4, 557-560(2010).

[125] Amy C.Turner-Foster, Mark A.Foster, Reza Salem, Alexander L.Gaeta, and Michal Lipson, *Opt. Express* 18, 1904-1908 (2010).

[126] A.V. Gorbach, X. Zhao, and D.V. Skryabin, "Dispersion of nonlinearity and modulation instability in subwavelength semiconductor waveguides ," *Optics Express*, 19, 9345-9351(2011).

[127] G. Van Simaeys, Ph. Emplit, and M. Haelterman, "Experimental demonstration of the fermi-pasta-ulam recurrence in a modulationally unstable optical wave," *Phys. Rev. Lett.* 87, 033902 (2001)

[128] C. Koos, P. Vorreau, T. Vallaitis, P. Dumon, W. Bogaerts, R. Baets, B. Esembeson, I. Biaggio, T. Michinobu, F. Diederich, W. Freude, and J.

Leuthold, “All-optical high-speed signal processing with silicon-organic hybrid slot waveguides,” *Nat. Photonics* 3, 216–219 (2009).

[129] J. S. Aitchison, A. H. Kean, C. N. Ironside, A. Villeneuve, and G. I. Stegeman, "Ultrafast All-Optical Switching in $Al_{0.18}Ga_{0.82}As$ Directional Coupler in $1.55\mu m$ Spectral Region," *Electron Lett.* 27, 1709-1710 (1991).

[130] Z. Xu, B. Maes, X. Jiang, J. D. Joannopoulos, L. Torner, and M. Soljacić, “Nonlinear photonic crystals near the supercollimation point,” *Opt. Lett.* 33, 1762–1764 (2008).

[131] Sh. Amiranashvili and U. Bandelow and N. Akhmediev, “Dispersion of nonlinear group velocity determines shortest envelope solitons”, *Phys. Rev. A* 84, 043834 (2011).

[132] A. R. Davoyan, I. V. Shadrivov, and Y. S. Kivshar, “Self-focusing and spatial plasmon-polariton solitons,” *Opt. Express* 17, 21732–21737 (2009).

[133] D. V. Skryabin, A. V. Gorbach, and A. Marini, “Surface-induced nonlinearity enhancement of TM modes in planar subwavelength waveguides,” *J. Opt. Soc. Am. B* 28, 109–114 (2011).

[134] A. Marini, R. Hartley, A. V. Gorbach, and D. V. Skryabin, “Surface-induced nonlinearity enhancement in subwavelength rod waveguides,” *Phys. Rev. A* 84, 063839 (2011).

[135] P. Kinsler and G. H. C. New, “Few-cycle soliton propagation,” *Phys. Rev. A* 69, 013805 (2004).

[136] Y. Xiang, S. Wen, X. Dai, Z. Tang, W. Su, and D. Fan, “Modulation instability induced by nonlinear dispersion in nonlinear metamaterials,” *J. Opt. Soc. Am. B*, 24, 3058-3063(2007).

[137] J. Gomez-Gardeñes, B. A. Malomed, L. M. Flora, and A. R. Bishop, “Solitons in the Salerno model with competing nonlinearities,” *Phys. Rev. E* 73, 036608 (2006).

[138] Xuesong Zhao, Andrey V. Gorbach, and Dmitry V. Skryabin, "Dispersion of nonlinearity in subwavelength waveguides: derivation of pulse propagation equation and frequency conversion effects", *J. Opt. Soc. Am. B*, 30, 812, 2013.

[139] W. Ding, O. K. Staines, G. D. Hobbs, A. V. Gorbach, C. de Nobriga, W. J. Wadsworth, J. C. Knight, D. V. Skryabin, M. J. Strain, and M. Sorel, "Modulational instability in a silicon- on-insulator directional coupler: role of the couplinginduced group velocity dispersion," *Opt. Lett.* 37, 668–670 (2012).

[140] D. V. Skryabin and A. V. Gorbach, "Looking at a soliton through the prism of optical supercontinuum," *Rev. Mod. Phys.* 82, 1287–1299 (2010).

[141] I.-W. Hsieh, X. Chen, X. Liu, J. I. Dadap, N. C. Panoiu, C.-Y. Chou, F. Xia, W. M. Green, Y. A. Vlasov, and R. M. Osgood, "Supercontinuum generation in silicon photonic wires," *Opt. Express* 15, 15242–15249 (2007).

[142] M.J. Potasek, Modulation instability in an extended nonlinear Schrodinger equation, *Optics Letters*, 12, 921-923(1987).

[143] Zakharov, V. Ostrovsky, L. Modulation instability: The beginning, *Physica, D.* 238, 540 (2009).

[144] Umbanhowar, P. B.,Melo, F. Swinney, H. L., "Localized excitations in a vertically vibrated granular layer", *Nature* 382, 793 (1996).

[145] Solli, D. R., Ropers, C., Koonath, P., Jalali, B., "Optical rogue waves", *Nature*, 450, 06402 (2007).

[146] Xia, H., Maimbourg, T., Punzmann, H., Shats, M., "Oscillon Dynamics and Rogue Wave Generation in Faraday Surface Ripples", *Phys. Rev. Lett.* 109,114502 (2012).

[147] Ankiewicz, A., Soto-crespo, J. M., Chowdhury, M. A., Akhmediev, N., "Rogue waves in optical fibers in presence of third-order dispersion , self-steepening , and self-frequency shift", *America*, 30(1) (2013).

[148] Bender, C. M., Boettcher, S., "Real Spectra in Non-Hermitian Hamiltonians Having PT Symmetry", *Phys. Rev. Lett.*, 80(24), 5243–5246, (1998).

[149] Rüter, C. E., Makris, K. G., El-ganainy, R., Christodoulides, D. N., Segev, M., Kip, D., "Observation of parity time symmetry in optics", *Nature Physics*, 6(3), 192–195 (2010).

[150] Alois Regensburger, Christoph Bersch, Mohammad-Ali Miri, Georgy Onishchukov, Demetrios N. Christodoulides and Ulf Peschel, "Parity–time synthetic photonic lattices", *Nature* 488, 168-171 (2012).

[151] Longhi, S., "Bloch Oscillations in Complex Crystals with PT Symmetry", *Phys. Rev. Lett.*, 103(12), 123601,(2009).

[152] Makris, K. G., El-Ganainy, R., Christodoulides, D. N., "Beam Dynamics in PT Symmetric Optical Lattices", *Phys. Rev. Lett.*, 100(10), 103904, (2008).

[153] Bendix, O., Fleischmann, R., Kottos, T., Shapiro, B., "Exponentially Fragile PT Symmetry in Lattices with Localized Eigenmodes", *Phys. Rev. Lett.*, 103(3), 030402, (2009).

[154] Dmitriev, S. V., Suchkov, S. V., Sukhorukov, A., Kivshar, Y. S., "Scattering of linear and nonlinear waves in a waveguide array with a PT-symmetric defect", *Phys. Rev. A*, 84(1), 013833, (2011).

[155] Zheng, M. C., Christodoulides, D. N., Fleischmann, R., Kottos, T., "PT optical lattices and universality in beam dynamics", *Phys. Rev. A*, 82(1), (2010).

[156] West, C. T., Kottos, T., Prosen, T., "PT-Symmetric Wave Chaos", *Phys. Rev. Lett.*, 104(5), 054102, (2010).

[157] Klaiman, S., Günther, U., Moiseyev, N., "Visualization of Branch Points in PT-Symmetric Waveguides", *Phys. Rev. Lett.*, 101(8), 080402, (2008).

[158] Lin, Z., Ramezani, H., Eichelkraut, T., Kottos, T., Cao, H., & Christodoulides, D. N., "Unidirectional Invisibility Induced by PT-Symmetric Periodic Structures", *Phys. Rev. Lett.*, 106(21), 213901, (2011).

[159] Sukhorukov, A. a, Dmitriev, S. V, Suchkov, S. V, Kivshar, Y. S., "Nonlocality in PT-symmetric waveguide arrays with gain and loss", *Optics letters*, 37(11), 2148–2150, (2012).

[160] Guo, a., Salamo, G. J., Volatier-Ravat, M., Aimez, V., Siviloglou, G. a., & Christodoulides, D. N., "Observation of PT-Symmetry Breaking in Complex Optical Potentials", *Phys. Rev. Lett.*, 103(9), 093902, (2009).

[161] Longhi, S., "Spectral singularities and Bragg scattering in complex crystals", *Phys. Rev. A*, 81(2), 022102, (2010).

[162] Ramezani, H., Kottos, T., El-Ganainy, R., Christodoulides, D. N., "Unidirectional nonlinear PT-symmetric optical structures", *Phys. Rev. A*, 82(4), 043803, (2010).

[163] El-Ganainy, R., Makris, K. G., Christodoulides, D. N., Musslimani, Z. H., "Theory of coupled optical PT-symmetric structures", *Optics letters*, 32(17), 2632–2634, (2007).

[164] Sukhorukov, A., Xu, Z., Kivshar, Y. S., "Nonlinear suppression of time reversals in PT-symmetric optical couplers", *Phys. Rev. A*, 82(4), 043818, (2010).

[165] Barashenkov, I. V, Suchkov, S. V, Sukhorukov, A. A., Dmitriev, S. V, Kivshar, Y. S., "Breathers in PT -symmetric optical couplers", *Phys. Rev. A*, 86,053809 (2012).

[166] Musslimani, Z. H., Makris, K. G., El-Ganainy, R., Christodoulides, D. N., "Analytical solutions to a class of nonlinear Schrödinger equations with PT-like potentials", *Journal of Physics A: Mathematical and Theoretical*, 41(24), 244019, (2008).

[167] Musslimani, Z. H., "Optical Solitons in PT Periodic Potentials", *Phys. Rev. Lett.*, 100(3), 030402, (2008).

[168] Suchkov, S. V., Malomed, B. A., Dmitriev, S. V., Kivshar, Y. S., "Solitons in a chain of parity-time-invariant dimers", *Phys. Rev. E*, 84(4), 046609, (2011).

[169] Alexeeva, N. V., Barashenkov, I. V., Sukhorukov, A., and Kivshar, Y. S., "Optical solitons in PT-symmetric nonlinear couplers with gain and loss", *Phys. Rev. A*, 85(6), 063837 (2012).

[170] Skryabin, D. V, Firth, W. J., "Dynamics of self-trapped beams with phase dislocation in saturable Kerr and quadratic nonlinear media", *Phys. Rev. E.*, 58(3), 3916–3930 (1998).

[171] Pelton, M., Aizpurua, J. Bryant, G., "Metal-nanoparticle plasmonics", *Laser & Photon. Rev.* 2, 136 (2008).

[172] Gramotnev, D. K., Bozhevolnyi, S. I., "Plasmonics beyond the diffraction limit", *Nature Photon.* 4, 83 (2010).

[173] J. McPhillips, A. Murphy, M. P. Jonsson, W. R. Hendren, R. Atkinson, F. Hook, A. V. Zayats, and R. J. Pollard, "High-perfomance biosensing using arrays of plasmonic nanotubes", *ACS Nano* 4, 2210 (2010).

[174] A. Murphy, Y. Sonnefraud, A. V. Krasavin, P. Ginzburg, F. Morgan, J. McPhillips, G. Wurtz, S. A. Maier, A. V. Zayats, and R. Pollard, "Fabrication and optical properties of large-scale arrays of gold nanocavities based on rod-in-a-tube coaxials", *Appl. Phys. Lett.* 102, 103103 (2013).

[175] Noskov R. E., Belov P. A. & Kivshar Y. S. Subwavelength plasmonic kinks in arrays of metallic nanoparticles. *Opt. Express* 20, 2733 (2012).

[176] Noskov R. E., Belov P. A. & Kivshar Y. S. Subwavelength modulational instability and plasmon oscillons in nanoparticle arrays. *Phys. Rev. Lett.* 108, 093901 (2012).

[177] Andrea Marini, Dmitry V. Skryabin,1, Boris Malomed, "Stable spatial plasmon solitons in a dielectric-metal-dielectric geometry with gain and loss", *Opt. Express* 19, 6616-6622, (2011).

[178] N. N. Ahmediev and A. Ankiewicz, Solitons: Nonlinear Pulses and Beams (Chapman and Hall, 2007).

[179] A. Marini and D. V. Skryabin, "Ginzburg-landau equation bound to the metal-dielectric interface and transverse nonlinear optics with amplified plasmon polaritons," *Phys. Rev. A* 81, 033850 (2010).

[180] Stefan Alexander Maier, Plasmonics: fundamentals and Applications (Springer, 2007).

[181] E. Feigenbaum and M. Orenstein, "Plasmon-solitons," *Opt. Lett.* 32, 674–676 (2007).

[182] J. Yang, Phys. Rev. E 66, 026601 (2002).

[183] V. I. Kruglov, Yu. A. logvin, and V. M. Volkov, *J. Mod. opt.* 39, 2277 (1992).

[184] J. Atai, Y. Chen, and J. M. Soto-Crespo, *Phys. Rev. A* 49, R3170 (1994).

[185] W. J. Firth and D. V. Skryabin, Optical Solitons Carrying Orbital Angular Momentum, *Phys. Rev. Lett.* 79, 2450 (1997)

[186] V. Tikhonenko, J. Christou, and B. Luther-Davies, *J. Opt. Soc. Am. B* 12, 2046 (1995).

[187] V. Tikhonenko, J. Christou, and B. Luther-Davies, *Phys. Rev. Lett.* 76, 2698 (1996).

[188] D. V. Petrov, L. Torner, J. Martorell, R. Vilaseca, J. P. Torres, and C. Cojocaru, *Opt. Lett.* 23, 1444 (1998).

[189] Y. S. Kivshar and B. Luther-Davies, *Phys. Rep.* 298, 81 (1998).

[190] N. N. Akhmediev, V. I. Korneev, and R. F. Nabiev, *Opt. Lett.* 17, 393 (1992).

[191] G. Theocharis, D. J. Frantzeskakis, P. G. Kevrekidis, B. A. Malomed, and Y. S. Kivshar, "Ring Dark Solitons and Vortex Necklaces in Bose-Einstein Condensates", *Phys. Rev. Lett.* 90, 120403 (2003).

[192] K. M. Mertes, J. W. Merrill, R. Carretero-Gonzalez, D. J. ´ Frantzeskakis, P. G. Kevrekidis, and D. S. Hall, "Nonequilibrium Dynamics and Superfluid Ring Excitations in Binary Bose-Einstein Condensates", *Phys. Rev. Lett.* 99, 190402 (2007).

[193] M. Scherer, B. Lucke, G. Gebreyesus, O. Topic, F. ¨ Deuretzbacher, W. Ertmer, L. Santos, J. J. Arlt, and C. Klempt, "Spontaneous Breaking of Spatial and Spin Symmetry in Spinor Condensates", *Phys. Rev. Lett.* 105, 135302 (2010).

[194] K. J. H. Law, P. G. Kevrekidis, and L. S. Tuckerman, "Stable Vortex–Bright-Soliton Structures in Two-Component Bose-Einstein Condensates", *Phys. Rev. Lett.* 105, 160405 (2010).

[195] Ji Li, Deng-Shan Wang, Zhi-Yong Wu, Yan-Mei Yu, and Wu-Ming Liu, "Three-dimensional ring vortex solitons and their stabilities in Bose-Einstein condensates under magnetic confinement", *Phys. Rev. A* 86, 023628 (2012).

[196] L. Allen, M. W. Beijersbergen, R. J. C. Spreeuw, and J. P. Woerdman, *Phys. Rev. A* 45, 8185 (1992).

[197] N. R. Heckenberg, R. McDuff, C. P. Smith, and A. G. White, *Opt. Lett.* 17, 221 (1992).

[198] N. B. Simpson, K. Dholakia, L. Allen, and M. J. Padgett, *ibid.* 22, 52 (1997).

[199] D. Rozas, C. T. Law, and G. A. Swartzlander, *J. Opt. Soc. Am. B* 14, 3054 (1997).

[200] M. S. Soskin, V. N. Gorshkov, M. V. Vasnetsov, J. T. Mallos, and N. R. Heckenberg, *Phys. Rev. A* 56, 4064 (1997).

[201] William H. Press, Saul A. Teukolsky, William T. Vetterling and Brian P. Flannery, Numerical Recipes in Fortran 77 (the Press Syndicate of the University of Cambridge, New York, 2001).